CHARACTERIZING A REGULATORY AXIS OF MICRORNA-200B, THE RNA-BINDING PROTEIN QUAKING, AND CYCLIN D1 IN MODULATING TUMOR ANGIOGENESIS AND METASTASIS

Salma Haleema Azam

A dissertation submitted to the faculty at the University of North Carolina at Chapel Hill in partial fulfillment of the requirements for the degree of Doctor of Philosophy in the Curriculum in Genetics and Molecular Biology in the School of Medicine.

Chapel Hill
2019

Approved by:

Chad V. Pecot

Victoria Bautch

Andrew Dudley

Albert Baldwin

Jeff Sekelsky

ABSTRACT

Salma Haleema Azam: Characterizing a regulatory axis of microRNA-200b, the RNA-binding protein quaking, and cyclin D1 in modulating tumor angiogenesis and metastasis
(Under the direction of Chad V. Pecot)

Angiogenesis is critical to cancer development and metastasis. However, anti-angiogenic agents have only had modest therapeutic success, partly due to an incomplete understanding of tumor endothelial cell (EC) biology. The Pecot lab previously reported that the microRNA (miR)-200 family inhibits metastasis through regulation of tumor angiogenesis, but the underlying molecular mechanisms are poorly characterized. Here, using integrated bioinformatics approaches, I identified the RNA-binding protein (RBP) quaking (QKI) as a leading miR-200b endothelial target with previously unappreciated roles in the tumor microenvironment (TME) in lung cancer. In lung cancer samples, both miR-200b suppression and QKI overexpression corresponded with tumor ECs relative to normal ECs, and QKI silencing phenocopied miR-200b-mediated inhibition of sprouting. Additionally, both cancer cell and endothelial QKI expression in patient samples significantly corresponded with poor survival and correlated with angiogenic indices. QKI supported EC function by stabilizing cyclin D1 (CCND1) mRNA to promote EC G1/S cell cycle transition and proliferation. Both nanoparticle-mediated RNA interference (RNAi) of endothelial QKI expression and palbociclib blockade of CCND1-CDK4/6 function potently inhibited metastasis in concert with significant effects on tumor vasculature. Altogether, this work demonstrates the clinical relevance and therapeutic potential of a novel, actionable miR/RBP axis in tumor angiogenesis and metastasis.

To my baby brothers and sisters: Taseer, Tauqeer, Sofia, Saaliha, and Samrah, you are my world.

ACKNOWLEDGEMENTS

There are no words to do justice to the amount of gratitude and love I hold in my heart for the friends and family who have brought me to where I am today. I give thanks first and foremost to my loving parents, Naweed and Marriam Azam, who have showered me with relentless and unconditional love, support, and prayers my entire life and have always encouraged me to shoot for the stars; to my grandmother (my beloved “Nanee”), who is nothing short of the complete and absolute embodiment of love, compassion, and strength; to my great uncle, Dr. Amjad Umar (my dear “Nanaboo”), who was both the first and the most inspiring and loving PhD scientist I ever met; and to Numan Ahmad, for coming into my life with unconditional happiness and love when I needed him the most. And above all else, I say *Alhamdolillah*, “all praise belongs to God,” for blessing me with so many wonderful and caring people in my life, for answering all my prayers, and for granting me the opportunity to pursue my passion.

I close with a final thank you once again to my mother, without whom I would be completely and absolutely nothing: you are my other half, and everything I aspire to be.

TABLE OF CONTENTS

LIST OF FIGURES

LIST OF TABLES

LIST OF ABBREVIATIONS

αSMA	Alpha smooth muscle actin
µCT	micro computed tomography
AES	Amino-Terminal Enhancer of Split
AGO	Argonaute
ANG2	Angiopoietin-2
ANGPTL4	Angiopoietin-like 4
ARP2/3	Actin-related protein 2/3
ATCC	American Type Culture Collection
BLI	Bioluminescence
BSA	Bovine serum albumin
CA9	Carbonic anhydrous IX
CCND1	Cyclin D1
CCR4	C-C motif chemokine receptor 4
CD31	Cluster of differentiation 31
CDC42	Cell division cycle 42
CDK	Cyclin dependent kinase
circRNA	Circular RNA
CK	Cytokeratin
CLDN5	Claudin-5
CNP	Chitosan nanoparticle
COX-2	Cyclooxygenase-2
CXCL	C-X-C motif chemokine ligand
CXCR4	C-X-C motif chemokine receptor 4

DCC	Deleted in colorectal carcinoma
DCP	Decapping mRNA
DDX6	DEAD-box helicase 6
DGCR8	DiGeorge Syndrome Critical Region Gene 8
DLL4	Delta-like 4
DMEM	Dulbecco Modified Eagle Medium
DMSO	Dimethylsulfoxide
DOPC	1,2-dioleoyl-sn-glycero-3-phosphatidylcholine
EC	Endothelial cell
EGF	Epidermal growth factor
EGFR	Epidermal growth factor receptor
EHS	Environmental Health and Safety
EGM2	Endothelial cell growth medium 2
EMT	Epithelial to mesenchymal transition
EndoMT	Endothelial to mesenchymal transition
EPCAM	Epithelial cellular adhesion molecule
EPO	Erythropoietin
EREG	Epiregulin
ETS-1	E26 oncogene homolog 1
EU	Ethylene uridine
EV	Empty vector
EXP5	Exportin 5
EZH2	Enhancer of zeste 2 polycomb repressive complex 2 subunit
FACS	Fluorescent activated cell sorting
FBS	Fetal bovine serum

FDA	U.S. Food and Drug Administration
FDR	False discovery rate
FGF	Fibroblast growth factor
FITC	Fluorescein isothiocyanate
GAPDH	Glyceraldehyde-3-phosphate dehydrogenase
GATA	Globin transcription factor binding protein 2
GEM	Genetically engineered mouse
GFP	Green fluorescent protein
GLUT-1	Glucose transporter 1
GTP	Guanosine triphosphate
GW	Glycin tryptophan
HBSS	Hanks balanced salt solution
HER2	Human epidermal growth factor receptor 2
HIF	Hypoxia inducible factor
HRE	Hypoxia response element
HUVEC	Human umbilical vein endothelial cells
ID1	Inhibitor of cell differentiation 1
IF	Immunofluorescence
IGFBP4	Insulin like growth factor binding protein 4
IHC	Immunohistochemistry
IL-8	Interleukin-11
IP	Intraperitoneal
IPA	Ingenuity pathway analysis
IRB	Institutional Review Board
JAG1	Jagged1

KH	K homology
KLF2	Kruppel like factor 2
L1CAM	L1 cell adhesion molecule
LKB1	Liver kinase B1
LNEC	Lung normal endothelial cell
LUAD	Lung adenocarcinoma
LUSC	Lung squamous cell carcinoma
LYVE1	Lymphatic vessel endothelial hyaluronan receptor 1
MBP	Myelin basic protein
MEF2C	Myocyte enhancer factor 2C
MET	Mesenchymal to epithelial transition
miR	microRNA
MMP	Matrix metalloproteinase
mTOR	Mammalian target of rapamycin
MVD	Microvessel density
MYOCD	Myocardin
NC	Negative control
NEO	Neogenin
NHLF	Normal human lung fibroblast
NICD	Notch 1 intracellular domain
NKXX2-1	NK2 homeobox 1
NOT	Negative regulator of transcription
NP	Nanoparticle
NRP1	Neuropillin-1
NTN	Netrin

OA	Omphalomesenteric artery
OCLN	Occludin
OCT	Optimal cutting temperature compound
ORF	Open reading frame
PAI-1	Plasminogen activator-1
PARN	Poly(A)-specific ribonuclease
PBS	Phosphate buffered saline
PCR	Polymerase chain reaction
PDGF	Platelet-derived growth factor
PDGFRβ	Platelet-derived growth factor receptor β
PHD2	Prolyl hydroxylase domain protein 2
PIGF	Placenta growth factor
PLXDC1	Plexin domain containing 1
pri-miRNA	Primary microRNA
PTK	Protein tyrosine kinase
QKI	Quaking
qk^v	Quaking viable
QRE	Quaking response element
RA	Retinoic acid
RBP	RNA binding protein
RGD	Arginine-glycine-aspartate
RIN	RNA integrity number
RISC	RNA-induced silencing complex
RNAi	RNA interference
ROBO	Roundabout

ROI	Region of interest
S1P	Sphingosine-1-phosphate
S1PR	Sphingosine-1-phosphate receptors
siR	Small interfering RNA
SM22	Smooth muscle protein 22
SRF	Serum response factor
STAR	Signal transduction and activation of RNA
STAT3	Signal transducer and activator of transcription 3
TBS-T	Tris-buffered saline-Tween 20
TCGA	The Cancer Genome Atlas
TEC	Tumor endothelial cell
TGF-β	Transforming growth factor beta
TIE2	TEK receptor tyrosine kinase
TINAGL1	Tubulointerstitial nephritis antigen like 1
TMA	Tissue microarray
TME	Tumor microenvironment
TMP	Tissue inhibitor of metalloproteinase
TNRC6	Trinucleotide repeat containing 6
TPL	Tissue Pathology Laboratory
TRBP	Trans-activation responsive RNA-binding protein
TSP1	Thrombospondin-1
UTR	Untranslated region
UV	Ultraviolet
VA	Vitelline artery
VASH2	Vasohibin-2

VE-cadherin	Vascular endothelial cadherin
VEGF	Vascular Endothelial Growth Factor
VEGFR	Vascular Endothelial Growth Factor Receptor
VHL	von Hippel Lindau
ZEB2	Zinc finger E-box-binding homeobox 2

CHAPTER 1: INTRODUCTION[1]

Metastasis and the Metastatic Cascade

Cancer is the second leading cause of death in the U.S. and among the top 10 killers in the world. Approximately 90% of cancer patients die primarily due to the spread, or metastasis, of disease to distant sites (Gupta and Massague, 2006). Therefore, developing novel approaches for therapeutic targeting of metastasis is critical for improving patient outcomes.

The metastatic cascade refers to the process by which cancer cells shed from a growing primary tumor, invade the endothelial barrier and enter the circulation via intravasation, arrest in capillary beds within distant organs, extravasate, and ultimately re-activate pro-angiogenic and proliferation pathways to support outgrowth from micrometastases into vascularized macrometastases. The first step of this process consists of cancer cells invading into the tumor-associated stroma and eventually into the healthy tissue parenchyma. One of the greatest barriers to this invasion is the highly-structured basement membrane (Valastyan and Weinberg, 2011). Cancer cells overcome this by activating matrix metalloproteinases (MMPs) which degrade the basement membrane and other components of the extracellular matrix to allow cancer cell invasion and the release of growth factors sequestered within the matrix. The release of these growth factors helps to further stimulate cancer cell growth (Kessenbrock et al., 2010). Many cancer cells are also believed to activate a biological program known as the

[1] The section "Therapeutic RNAi for Tumor Angiogenesis Targeting" was modified and previously appeared as my authored contribution to the article presented in the journal *Frontiers in Pharmacology*. The actual citation is as follows: Harrison, E.B., Azam, S.H., and Pecot, C.V. (2018). Targeting Accessories to the Crime: Nanoparticle Nucleic Acid Delivery to the Tumor Microenvironment. Front Pharmacol 9, 307.

epithelial to mesenchymal transition (EMT) which decreases adherens and tight junctions between epithelial cells, causes a disruption in cellular polarity, and enhances mesenchymal characteristics such as invasiveness to enable metastasis (Thiery et al., 2009). As the cancer cells invade, the surrounding stroma is stimulated to become more reactive as the cancer cells encounter fibroblasts, endothelial cells (ECs), adipocytes, bone marrow-derived cells, and immune infiltrates (Grivennikov et al., 2010; Joyce and Pollard, 2009). These interactions between stromal components and cancer cells help promote tumor progression. For example, tumor associated macrophages have been shown to activate epidermal growth factor receptor (EGFR) signaling in breast carcinoma cells (DeNardo et al., 2009).

Intravasation refers to the process by which cancer cells invade into the lumen of blood or lymphatic vessels and is dependent on molecular alterations that enable cancer cell penetration of the pericyte-endothelial barrier wall of blood vasculature. For example, the transcriptional modulator amino-terminal enhancer of split (AES) was demonstrated to inhibit colon cancer cell intravasation through regulation of Notch signaling (Sonoshita et al., 2011). Intravasation is believed to be necessary to allow cancer cells to travel throughout the circulation and colonize distant sites. Cancer cells have to survive a number of stresses while in circulation, including the absence of integrin-mediated adhesion to the extracellular matrix which normally promotes cell survival (Valastyan and Weinberg, 2011). Un-anchored epithelial cells will usually undergo a form of cell death known as anoikis (Guo and Giancotti, 2004) which needs to be evaded to allow metastasis. For example, tyrosine kinase receptor B (TRKB) was demonstrated to suppress anoikis and to be required for metastasis of transformed intestinal epithelial cells (Douma et al., 2004). After cancer cells have traveled in the circulation, they are believed to arrest at specific sites either due to lumen size limitations of specific capillary beds they encounter, and/or specific molecular features of distinct host tissues (Valastyan and Weinberg, 2011). Regarding the latter point, one such example is breast cancer cell expression

of metadherin, which has been demonstrated to promote cancer cell arrest in the lungs by enabling binding to pulmonary vasculature (Brown and Ruoslahti, 2004).

Cancer cells shedding from a primary tumor are thought to also be recruited into lymphatic vessels and localized to lymph nodes. It has been clinically observed that the presence of lymphatic metastases predicts a more aggressive stage of cancer and a worse overall patient prognosis in multiple cancer types, but the mechanisms by which the lymphatic system contribute to cancer progression remain poorly characterized. Ultimately, however, lymphatic vessels do not provide a conduit directly to organs, so cancer cells must eventually be returned to the circulation to be able to hone to distant sites (Chambers et al., 2002).

Once cancer cells have arrested at a specific site, they extravasate, or cross the endothelial barrier from the lumen into the extravascular space to begin establishing a micrometastasis. Cancer cells face additional challenges at this step as opposed to the intravasation step, as here the vasculature and tissue microenvironment are much more normalized and impermeable (Valastyan and Weinberg, 2011). One possible mechanism that may help facilitate extravasation is primary tumor secretion of factors that increase vascular permeability at distant sites. For example, secretions of angiopoietin-like 4 (ANGPTL4), epiregulin (EREG), cyclooxygenase-2 (COX-2), MMP-1, and MMP-2 were shown to disrupt pulmonary EC-EC junctions and promote breast cancer cell extravasation (Gupta et al., 2007a; Padua et al., 2008).

The extravasated cancer cells must then establish micrometastases in a new, likely hostile environment that is molecularly and structurally different from the microenvironment of the host primary tumor (Valastyan and Weinberg, 2011). Some evidence suggests that primary tumors may release molecular signals which alter these recipient microenvironments to establish a “premetastatic niche” including upregulation of fibronectin to recruit hematopoietic progenitor cells to secret MMPs which make the extracellular matrix more amenable to cancer cell colonization (Psaila and Lyden, 2009). The colonizing cancer cells themselves must also

undergo molecular changes. For example, it has been shown that breast carcinoma cells activate Src tyrosine kinase signaling to be able to successfully colonize in the bone; however, this cell signaling was not required for initial honing to this site (Zhang et al., 2009).

Once the cancer cells have successfully established at a new site, they may not immediately outgrow into metastases. They may remain as occult micrometastases for a period of time either due to impaired cancer cell proliferation in the hostile new microenvironment; or due to a balance in cell proliferation and apoptosis and the absence of tumor angiogenesis to tip the scale and promote tumor outgrowth (Chambers et al., 2002). In one study, ANG2 was shown to enable pancreatic carcinoma metastatic colonization by promoting recruited myeloid cell-mediated activation of vascularization of metastases (Mazzieri et al., 2011).

Each cancer type is associated with unique metastasis tropisms, i.e. breast cancer cells preferentially metastasize to brain, bone, and lungs; lung cancer cells preferentially metastasize to liver and thoracic lymph nodes, etc. The unique patterns of tissue infiltration observed in different cancer types suggests that the deposition of cancer cells at distant sites is not due to chance or random distribution alone. It is believed that both the directionality of blood flow as it passes from one organ to another, as well as the unique molecular characteristics of each organ type, allow for the distinct patterns of metastasis observed. The “seed and soil hypothesis” predicts that the molecular nature of different organ/tissue types influences their contribution to metastasis (Paget, 1889). In brief, this suggests that the different chemokines, ligands, etc. expressed by certain tissue types make it more likely for specific cancer cell types to localize to particular organs. For example, breast cancer cells express high levels of C-X-C motif chemokine receptor 4 (CXCR4), which is the receptor for C-X-C motif chemokine ligand 12 (CXCL12) highly expressed in the lungs. Thus, breast cancer cells can find an agonist for their particular expressed receptor more readily at the lungs, making it a more likely site at which the cancer cells will metastasize (Chambers et al., 2002). In another example, it has been demonstrated that breast cancer cells promote osteoclast function via interleukin-11 (IL-11) and IL-6 to release growth factors normally

sequestered within the bone matrix and ultimately facilitate bone metastasis (Kang et al., 2003; Sethi et al., 2011).

To be able to successfully establish a new metastasis, cancer cells are also believed to require a high self-renewal capacity. Cells harboring such a capacity have been deemed “tumor-initiating cells.” For example, the transcription factors inhibitor of cell differentiation 1 (ID1) and ID3 and the transcription factor NK2 homeobox 1 (NKXX2-1) have all been shown to regulate metastasis in the breast and lung through alterations of the “tumor-initiating” state (Gupta et al., 2007b; Winslow et al., 2011).

In general, the early steps of the metastatic cascade are considered highly effective, whereas the latter steps following cancer cell entry into the circulation are much more prone to failure. It has been estimated that < 0.01% of tumor cells that enter the bloodstream eventually establish metastases, suggesting metastatic colonization of distant organs is a highly inefficient process. Thus, metastasis is believed to be an inefficient process largely due to the inability of micrometastases to activate tumor angiogenesis or continually support their growth in novel sites (Chambers et al., 2002), suggesting angiogenesis has an integral role in regulating both tumorigenesis and cancer spread.

Tumor Angiogenesis

Tumor angiogenesis, which refers to the sprouting of new tumor blood vessels from pre-existing host vasculature into the tumor microenvironment (TME), is a critical cancer hallmark. It is an appealing process to target therapeutically due to its importance in driving multiple components of tumor progression, including primary tumor growth, drug resistance, and distant metastasis (Baluk et al., 2005; Chambers et al., 2002; Folkman, 1971; Hanahan and Folkman, 1996). Judah Folkman was among the first to suggest that tumors cannot grow past 2-3 mm in diameter without promoting angiogenesis to support their metabolic demands and sustain their

continued growth (Folkman, 1971). However, this newly-established vasculature can also serve as a conduit for cancer cells to metastasize.

The Angiogenic Switch

ECs are some of the longest-living cells in the body apart from those found in the nervous system. Healthy adult vasculature is quiescent due to a controlled balance between pro- and anti-angiogenic factors that regulate EC proliferation and migration. A temporary usurpation of the balance activates angiogenesis to promote fundamental processes such as embryogenesis and wound healing. During embryonic development, blood vessels are first formed via vasculogenesis, or *de novo* vessel formation, from EC precursors assembling to create a primary capillary plexus. The EC precursors then undergo differentiation, and the plexus is remodeled via sprouting angiogenesis. During physiologic angiogenesis, vessels become mature and stabilized very quickly, but in the pathologic context, tumors hijack the balance between pro- and anti-angiogenic factors and permanently shift the balance to a pathologic, pro-angiogenic state (the “angiogenic switch”) to stimulate constant growth of new vessels (Bergers and Benjamin, 2003; Carmeliet, 2000; Hanahan and Folkman, 1996).

Tumors are believed to start out as avascular lesions that remain less than 1-2 mm in diameter, are dormant, and are at a steady state of proliferation and apoptosis. Once the tumors undergo the “angiogenic switch”, they experience exponential growth. This is believed to be what also happens at a new metastatic site. Many studies in autochthonous, mouse models of cancer have demonstrated that as tumors progress, they undergo distinct stages of growth, and it is after inducing angiogenesis that the tumors reach a more aggressive state (Bergers and Benjamin, 2003).

Activators of EC proliferation and migration are mainly receptor tyrosine kinase ligands, such as vascular endothelial growth factor (VEGF) A, C, and D (all bind VEGF Receptor 2 (VEGFR2)), fibroblast growth factor (FGF)s, platelet-derived growth factor (PDGF), epidermal

growth factor (EGF), placenta growth factor (PIGF) (binds VEGFR1), and ANG2 (binds to TEK receptor tyrosine kinase (TIE2)). These angiogenic molecules are all believed to be expressed by tumors. VEGFA expression alone can stimulate angiogenesis from quiescent vasculature and serves as a survival factor for ECs (Ferrara, 2002; Yancopoulos et al., 2000). MMP-9 has been shown to promote angiogenesis by degrading components of the extracellular matrix to release sequestered VEGF (Bergers et al., 2000) which then signals through VEGFR. Endogenous angiogenesis inhibitors include thrombospondin-1 (TSP1), which modulates EC proliferation and motility by inhibiting the release of VEGF from the extracellular matrix through suppression of MMP activity, directly binding VEGF, and modulating VEGFR signal transduction (Lawler and Lawler, 2012; Rodriguez-Manzaneque et al., 2001). Other endogenous angiogenesis inhibitors include statins, including angiostatin (a fragment of plasminogen), endostatin, tumstatin, and canstatin (fragments of collagens that bind to integrins). The relative levels of angiogenesis inhibitors and promoters determine whether the vasculature will be actively angiogenic or not (Bergers and Benjamin, 2003).

The steps and changes that parent vessels undergo to allow angiogenesis to occur have been well-studied (Pettersson et al., 2000). First the vessels undergo vasodilation and have increased permeability in response to VEGF to allow extravasation of plasma proteins which will lay down a matrix on which ECs can then migrate. There is also some dissociation of pericyte coverage via ANG2 signaling through TIE2 to help improve permeability. Basement membrane and extracellular matrix are degraded to create paths for ECs to migrate towards angiogenic signals. These are known as the tip cells. Additional ECs follow behind the leading ECs, and under normal circumstances the ECs further differentiate, change shape, adhere and form a lumen. They also continue to undergo proliferation to help increase vessel size. Mural cells are recruited and vascular basal lamina is produced (Bergers and Benjamin, 2003). Pericytes help inhibit EC proliferation and decrease their dependence on VEGFA production. Therefore, tumor

vessels with less pericyte coverage can have abnormal vessel diameter and more sensitivity to VEGF therapies (Benjamin et al., 1998; Benjamin and Keshet, 1997).

Molecular Basics of Sprouting Angiogenesis

Angiogenesis involves the sprouting, migration, and proliferation of ECs which are regulated by many factors. Tip cells are the migratory and invasive ECs at the leading end of a growing sprouting vessel which extend filopodia that respond to growth factors, the extracellular matrix, and other cues. They are stimulated to become migratory by VEGF. Following the tip cells, ECs known as stalk cells will undergo proliferation to help grow the developing vessel (Viallard and Larrivee, 2017). The Notch pathway has been implicated in modulating the tip/stalk EC phenotype. VEGF activation of VEGFR2 or neuropillin-1 (NRP1) has been shown to increase expression of the Notch ligand delta-like 4 (DLL4) (Phng and Gerhardt, 2009). DLL4 then binds to NOTCH1 in neighboring ECs, which causes the cleavage and release of the Notch 1 intracellular domain (NICD), which goes on to transcriptionally regulate gene expression to reduce the cell's response to VEGF (Blanco and Gerhardt, 2013; Bray, 2016). NICD activation has been associated with inhibition of VEGFR2, VEGFR3, NRP1 and upregulation of VEGFR1 (Jakobsson et al., 2010). VEGFR1 strongly associates with VEGF but has weak kinase activity and therefore acts as a competitive "decoy receptor" that reduces VEGF binding to VEGFR2. In this way, the cell with high VEGFR2 signaling and expression of DLL4 is more likely to have a tip cell-like phenotype, while the adjacent cells with higher Notch signaling maintain more of a proliferative/stalk cell phenotype (Ferrara et al., 2003; Jakobsson et al., 2010). In addition, jagged1 (JAG1) is a Notch receptor ligand strongly expressed in stalk cells that antagonizes DLL4-NOTCH1 signaling in the neighboring tip cell to help further maintain the differential phenotype between tip and stalk cells (Benedito et al., 2009).

Numerous filopodia protrude from the tip cells to respond to extracellular cues and signals, promote motility, and help establish focal adhesions. The Rho guanosine triphosphate

(GTP)ase cell division cycle 42 (CDC42) promotes filopodia production (Mattila and Lappalainen, 2008). RAC-actin-related protein 2/3 (ARP2/3) complexes regulate actin polymerization as well to help produce the cellular extensions (Ridley, 2015). Axon guidance molecules have also been implicated in endothelial tip cell guidance and vessel patterning: SLIT/roundabout (ROBO), netrin(NTN)/deleted in colorectal carcinoma (DCC)/UNC5 and NRP/plexin/sema families (Larrivee et al., 2009; Viallard and Larrivee, 2017). NRP1 has been shown to inhibit tip cell migration. The receptor UNC5B is activated by NTN1 or via NTN4 binding to neogenin (NEO) to regulate tip cell filopodia repulsion (Larrivee et al., 2007; Viallard and Larrivee, 2017). SLIT activates ROBO4 to induce vessel repulsion and also inhibit VEGFR2 activation (Koch et al., 2011; Viallard and Larrivee, 2017).

Lumen formation of the vessels is needed to initiate blood flow. One mechanism is believed to be that ECs undergo pinocytosis to internalize multiple vesicles of the plasma membrane that will then fuse together to create an intracellular lumen. This process is considered to be dependent on the signaling of integrins α2β1, αvβ3, and α5β1 (Sacharidou et al., 2012). Another model is that ECs negatively charge the glycoproteins expressed on their apical surface, which causes a repulsion between ECs and opening up of the lumen, followed by redistribution of cell-cell adhesions to the edge of the lumen (Strilic et al., 2009).

Vessel maturation to becoming functional and stable blood vessels is regulated by numerous factors. Tissue inhibitors of metalloproteinases (TMPs) antagonize MMPs to allow basement membrane deposition (Viallard and Larrivee, 2017). PDGFβ is secreted to stimulate recruitment of platelet-derived growth factor receptor β (PDGFRβ)-expressing pericytes, and it remains localized to the developing vessel via heparan sulfate proteoglycans (Andrae et al., 2008). Angiopoietins have also been implicated in mural cell-mediated stabilization of vessels. ANG1 is secreted by mural cells and activates TIE2 receptor on ECs, which leads to AKT activation, promotes survival, and inhibits apoptosis (Augustin et al., 2009). Sphingosine-1-phosphate (S1P) also stabilizes pericyte-EC interactions by binding to G protein-coupled

receptor sphingosine-1-phosphate receptors (S1PRs) to mediate N-cadherin trafficking and strengthen adhesion between ECs and pericytes (Lucke and Levkau, 2010).

Vascular endothelial cadherin (VE-cadherin) is a transmembrane protein which stabilizes EC-EC interactions and decreases vessel permeability and leakage. The intracellular domain is anchored to the cytoskeleton via β-catenin, whereas the extracellular domain is bound to VE-cadherin on a neighboring EC. VE-cadherin also promotes VEGFR2 dephosphorylation through the recruitment of phosphatases to ultimately enable blood vessel quiescence. Tight junction proteins claudin-5 (CLDN5), occludin (OCLN) and cluster of differentiation 31 (CD31) all also contribute to EC cell-cell adhesion by regulating the passage of solutes and ions and transducing intracellular signals (Dejana et al., 2009; Viallard and Larrivee, 2017; Wallez and Huber, 2008).

Role of Basement Membrane in Angiogenesis

The vascular basement membrane is structured like a tunnel, with ECs lining the inside and pericytes or mural cells lining the outside. The vascular basement membrane is involved in both the initiation and the ending steps of angiogenesis. ECs are normally quiescent when bound to the basement membrane, whose main components consist of type IV collagen (major component), laminin, heparan sulphate, proteoglycans, and other molecules. Therefore, the basement membrane is normally inhibiting proliferation and migration to maintain strong cell-to-cell adhesion (Form et al., 1986). Activated angiogenesis is associated with MMP-mediated (including MMP-2 and MMP-9) degradation of the basement membrane, which allows sprouting ECs to be freed from integrin cell surface anchors and migrate, proliferate, and invade the surrounding extracellular matrix. The basement membrane is very disorganized and highly crosslinked and therefore only certain domains of components are exposed. However, as those components are being degraded or disassembled, new cryptic domains are exposed. The new structural configurations of the same proteins then have different effects on the vasculature to

promote angiogenesis. In addition, disruption of the basement membrane frees sequestered growth factors such as VEGF and FGF, and also allows for pericyte detachment (Bergers et al., 2000; Egeblad and Werb, 2002; Folkman and D'Amore, 1996). When ECs detach, they eventually come into contact with what is known as the interstitial provisional matrix which includes vitronectin, fibronectin, type I collagen, and thrombin, which are all considered to provide proliferative cues (as opposed to the inhibitory signals given by the structured basement membrane) (Kalluri, 2003). As tumors begin to grow, they start recruiting immune cells, fibroblasts, and other stromal cells which produce additional VEGF and growth factors; therefore MMP activity is likely more important at the earlier stages of tumor angiogenesis (Kalluri, 2003).

As the MMPs degrade the basement membrane even further, what are known as cryptic domains begin to become exposed from partially degraded components of the basement membrane, which produces fragments with anti-angiogenic effects including, arrestin, canstatin, tumstatin (all derived from collagen type IV) and other collagen fragments (Colorado et al., 2000; Kamphaus et al., 2000; Kim et al., 2000; Maeshima et al., 2001). Basement membrane components bind to integrins to modulate integrin receptor downstream signaling to inhibit or promote EC function. Basement membrane components will bind to different cell surface integrins to have different effects on angiogenesis (Kalluri, 2003). At the later stages of vessel development, the anti-angiogenic cues may begin to become more predominant. Endostatin is one example of a specific inhibitor of EC proliferation and migration and promoter of EC apoptosis that is exposed after basement membrane degradation. The mechanism of EC inhibition appears to be via endostatin binding to cell surface proteoglycans, VEGFR2, and α5β1. Tumstatin is another example and has been shown to promote the apoptosis of dividing ECs by binding to αvβ3 to inhibit mammalian target of rapamycin (mTOR) signaling specifically in ECs (Kalluri, 2003).

Tumor Vessel Morphology

Angiogenesis produces chaotic and dysfunctional vasculature. While normal blood vessels consist of a continuous monolayer of tightly adhered ECs, close association of mural cells such as pericytes (which wrap around vessels and provide structural and chemical support), and a continuous basement membrane; tumor vessels have loosely associated ECs with large gaps between them, poor mural cell recruitment, and an irregular and discontinuous basement membrane. This reduced vessel wall integrity promotes leakiness and cancer cell intravasation, thus reducing drug delivery to the primary tumor and promoting distant metastasis (Baluk et al., 2005).

Tumor blood vessels are dilated, tortuous, disorganized, immature, sparsely covered by mural cells, leaky, poorly perfused, and lead to tumor hypoxia. Pericytes and smooth muscle cells help regulate blood flow and make vessels less permeable. In tumor vessels, pericytes have poorer association with the basement membrane and ECs. There is less pericyte coverage and they are abnormal in morphology (Bergers and Song, 2005; Morikawa et al., 2002). Higher EC proliferation and less pericyte coverage of tumor blood vessels contributes to their instability. High VEGF signaling from cancer cells inhibits PDGFRβ signaling in mural cells (Greenberg et al., 2008). Cancer cells release MMPs, elastase or trypsin to cleave VE-cadherin (Dejana et al., 2009). Inflammatory factors such as histamine stimulation can also disrupt vessel wall integrity by cleaving VE-cadherin (Guo et al., 2008). Electron microscopy images of tumor vessel basement membrane imaging type IV collagen, CD31 (marker of ECs) and alpha smooth muscle actin (αSMA, marker of pericytes) are disjointed, suggesting loose association of cells with the basement membrane. Electron microscopy images reveal that the tumor vascular basement membrane is uneven, with irregular thickness and even some perforations (Baluk et al., 2003).

The out of control growth of solid tumors and resulting restriction of the surrounding host tissue causes a great deal of intratumoral pressure. This pressure can cause vessels to

compress or collapse and stem blood flow. This compression also inhibits lymphatics and decreases the ability of the lymphatic system to drain interstitial fluid, further contributing to pressure build up (Jain et al., 2014). There is also increased fluid leakage from the vessels into the interstitial space. All these factors together result in a high interstitial fluid pressure, which disrupts blood pressure and flow within tumors and also makes for more difficult drug delivery. This ultimately causes poor oxygen delivery to the tumor, making it hypoxic. This results in selection of more aggressive cancer cell clones, as well as cells more likely to undergo EMT, which is believed to increase their ability to metastasize (Jain et al., 2014; Reymond et al., 2013).

Hypoxia and Tumor Progression

Due to the “angiogenic switch”, tumors are considered incapable of growing beyond 1--2 mm diameters in size without co-opting a new vascular supply, largely due to the effects of hypoxia. Under normal oxygen conditions, prolyl hydroxylase domain protein 2 (PHD2) hydrolyzes hypoxia inducible factors (HIFs) transcription factors to target them for ubiquitination by the von Hippel-Lindau (VHL) complex and ultimately proteasomal degradation (Giaccia et al., 2004; Mazzone et al., 2009). In hypoxia, PHD2 is unable to do so, allowing HIFs to bind to DNA sequence hypoxia response elements (HREs) to activate the expression of genes important for angiogenesis, survival, cell proliferation and glucose metabolism which include VEGF, transforming growth factor beta (TGF-β), PDGF-B, plasminogen activator-1 (PAI-1), erythropoietin (EPO) and glucose transporter 1 (GLUT-1). In addition, oncogenic signaling pathways in cancer cells have also been implicated in increasing HIF expression. Oncogene activation or tumor suppressor loss in cancer cells has also been shown to directly increase expression of angiogenesis-associated genes. For example, KRAS, human epidermal growth factor receptor 2 (HER2), EGFR, PI3K/AKT signaling have all been shown to upregulate VEGF (Viallard and Larrivee, 2017).

Anti-Angiogenic Therapies and Resistance Mechanisms

Currently, most anti-angiogenic therapeutic strategies focus on inhibition of the VEGF pathway, which has led to the U.S. Food and Drug Administration (FDA) approval of drugs for several cancer types (Table 1). Unfortunately, however, targeting the VEGF pathway thus far has had limited clinical success (Bergers and Hanahan, 2008). The effects are often temporary, modest, survival is only prolonged on the order of months, and are susceptible to numerous resistance mechanisms that have been shown to sometimes promote EC function or enhance metastasis (Bergers and Hanahan, 2008; Bottsford-Miller et al., 2012). Tumor-activated resistance mechanisms to VEGF inhibitors include activation of other pro-angiogenic pathways, vessel co-option, cancer cell vascular mimicry, and vasculogenesis (de novo vessel formation) from bone marrow-derived precursor ECs (Bergers and Hanahan, 2008; Ebos and Kerbel, 2011; Welti et al., 2013).

Vessel co-option is the process by which cancer cells recruit pre-existing vasculature of healthy host tissue to support their growth and metabolic demands, as opposed to stimulating the growth of new blood vessels via angiogenesis (Kuczynski et al., 2019). The mechanism of vessel co-option can be most easily recognized by distinct histopathological features of cancer growth and associated tumor vasculature: preserved, non-malignant vessel morphology that maintains the architecture of host tissue vessels; limited EC proliferation that is less than in angiogenic tumors and/or aligned with the low rate of endothelial proliferation in surrounding nonmalignant tissue; cancer growth into and invasion of surrounding normal tissue and a resulting irregular and undefined tumor border; cancer cell growth along pre-existing vascular structures which allows tumors to mimic or incorporate and ultimately preserve normal

Table 1 FDA Approved Anti-Angiogenic Drugs as of 2016

Drug	Type	Target/Mechanism	Approved Cancer Types
Axitinib	TKI	VEGFR and PDGFR	Renal cell carcinoma
Lenvatinib mesylate	TKI	VEGFR2	Thyroid
Pazopanib	TKI	VEGFR1,2,3, c-kit, PDGFR	Renal cell carcinoma, soft tissue carcinoma
Regorafenib	TKI	VEGFR2,3, Ret, Kit, PDGFR and Raf kinases	Colorectal
Sorafenib	TKI	RAF kinase, VEGFR2, PDGFRb	Hepatocellular carcinoma, renal cell carcinoma, thyroid
Sunitinib	TKI	VEGFR2, PDGFRb, c-kit, FLT3	Renal cell carcinoma, pancreatic neuroendocrine
Vandetanib	TKI	VEGFR2, EGFR	Medullary carcinoma of thyroid
Bevacizumab	Recombinant humanized monoclonal antibody	VEGF	Colorectal, non-small-cell lung, renal cell carcinoma, ovarian
Ramucirumab	Recombinant, fully human monoclonal antibody	VEGFR2	Gastric, gastro-esophageal junction, non-small-cell lung, colorectal
Ziv-aflibercept	Recombinant human soluble decoy receptor	Segments of extracellular domains of VEGFR1 and VEGFR2 fused to the constant region (Fc) of human IgG1; binds VEGF	Colorectal

FDA-approved anti-angiogenic drugs as of 2016 specifically indicated for anti-angiogenesis treatment; not including drugs with primary non angiogenesis-related indications. Information adapted from National Cancer Institute (https://www.cancer.gov) and REF (Jayson et al., 2016)

stromal tissue morphology as opposed to destroying it; preserved expression of normal tissue-specific endothelial markers within tumor endothelium; low expression of angiogenesis-associated markers; and preserved vascular membrane and vascular integrity of tumor vessels (Kuczynski et al., 2019).

Vessel co-option has been observed both as an intrinsic feature of solid tumors and as an acquired mechanism of resistance in response to anti-angiogenic therapy. For example, it has been demonstrated that hepatocellular carcinomas being treated with the anti-angiogenic tyrosine kinase inhibitor sorafenib undergo EMT to deeply invade the liver parenchyma and co-opt pre-existing liver vessels as a mechanism of resistance in response to angiogenesis inhibition (Kuczynski et al., 2016). In clinical samples of lung metastases, tumors have been demonstrated to vascularize via mechanisms of both angiogenesis or co-option of vessels. Cancer cells were shown to either growth within alveolar air spaces or invade the alveolar walls to co-opt alveolar capillaries, or, alternatively, cancer cells were also shown to grow as perivascular cuffs along larger lung vessels. In the alveolar growth pattern, cancer cells invaded the alveolar air spaces, facilitating the co-option of alveolar capillaries. In the interstitial growth pattern, cancer cells invaded the alveolar walls to co-opt alveolar capillaries. In the perivascular cuffing growth pattern, cancer cells grew by co-opting larger vessels of the lung (Bridgeman et al., 2017).

Mechanisms of vessel co-option are predicted to be associated with increased cancer cell invasiveness/motility, and increased cancer cell adhesion, both of which enable improved association of cancer cells with a pre-existing source of blood flow. ARP2/3, a protein complex involved in actin-mediated cell motility; zinc finger E-box-binding homeobox 2 (ZEB2), an important transcriptional driver of EMT, and Wnt signaling have all been implicated in promoting cancer cell motility in vessel co-option. Both L1 cell adhesion molecule (L1CAM) and β1 integrin have been implicated in cancer cell adhesion to brain blood vessels to enable vessel co-option (Kuczynski et al., 2019).

Another mechanism of angiogenesis or VEGF inhibition therapy resistance is the compensatory upregulation of alternative pro-angiogenic signaling pathways (Bergers and Hanahan, 2008). In a mouse model of pancreatic neuroendocrine cancer, treatment with the monoclonal antibody DC101 to inhibit VEGFR2 signaling caused an initial transitory inhibition of tumor growth and angiogenesis for 10-14 days, which was followed by a rebound during which tumor growth and vessel density were restored. This was found to be through increased expression of FGF and other growth factors. Treatment with an FGF trap after treatment with the VEGFR2 inhibitor slowed tumor rebound growth and angiogenesis, implicating the role of other signaling pathways in compensating for the loss of VEGF signaling (Casanovas et al., 2005). Similar phenomena have been observed in patients. Glioblastoma patients being treated with the VEGFR inhibitor cediranib had an initial period of responsiveness to the therapy, followed by a relapse, accompanied by re-initiation of tumor angiogenesis and a loss of vascular normalization as revealed by imaging. Circulating levels of FGF2 were found to be higher in relapsing patients compared to patients still in the response phase, indicating FGF2 may be involved in an angiogenesis resistance mechanism to VEGFR inhibition (Batchelor et al., 2007).

Another mechanism of resistance is the increased recruitment of vascular progenitor cells for incorporation into blood vessels. The hypoxic environment created by potent inhibition of angiogenesis can stimulate increased recruitment of bone marrow-derived cells which can eventually differentiate into ECs or pericytes (Bergers and Hanahan, 2008). For example, one study demonstrated that tumors treated with anti-angiogenic agents underwent acute hypoxia and necrosis, which caused a sudden accumulation of endothelial progenitor cells at the tumor margins and subsequent reactivated vascularization. Tumors not treated with an anti-angiogenic agent did not demonstrate this sudden increase in endothelial progenitors, suggesting their accumulation was an activated resistance mechanism (Shaked et al., 2006).

Increased pericyte coverage to stabilize vessels has also been observed to be a response of tumor vessels to anti-angiogenic therapy. It is believed that after pruning of

vasculature by an anti-angiogenic agent, tumors may begin to rely on pericytes to keep a select few vessels alive and functional to continue sustaining the tumor. It is believed that ECs induce pericyte recruitment to help promote their survival due to being deprived of VEGF signaling (Bergers and Hanahan, 2008). It has been shown that tumor vasculature with poor pericyte coverage are more susceptible to VEGF inhibition (Bergers et al., 2003) and that tumor pericytes express VEGF and other factors to support EC survival (Darland et al., 2003). Pericytes also regulate EC proliferation to allow vascular structures to mature and remain stabilized (Hirschi and D'Amore, 1997). Therefore, the remaining pericyte-covered vessels are thought to be less responsive to anti-angiogenic treatment (Bergers and Hanahan, 2008).

Another phenomenon that has been observed in tumors is cancer cell vasculogenic mimicry, in which tumor cells take on the phenotype of ECs. This was first observed as channel-like structures containing red blood cells within tumors (Maniotis et al., 1999). These cancer cells express markers of both tumors and endothelium (including VE-cadherin and CD31) and form perfused, extracellular matrix-rich vasculogenic-like networks (Viallard and Larrivee, 2017). VE-cadherin allows for the cancer cells to undergo tube formation and close cell-cell adhesions to create perfused “vessels” (Paulis et al., 2010). Cancer cells have also been found to integrate into the walls of already formed vessels and create mosaic vessels (Chang et al., 2000). Channels created by vasculogenic mimicry have been shown to anastomose with endothelial vessels and provide functional blood flow within tumors (Ruf et al., 2003). Because the cancer cells are lining the walls of the vasculature, they are directly exposed to constant blood flow and therefore have the possibility of easily detaching from the vessel wall and traveling via the circulation to distant sites (Viallard and Larrivee, 2017). Patients demonstrating evidence of vasculogenic mimicry have been shown to have worse clinical outcome (Yang et al., 2016).

In my dissertation, I aimed to characterize novel mechanisms of tumor angiogenesis and metastasis regulation independent of VEGF signaling to investigate alternate pathways to target for anti-angiogenic therapy and cancer treatment.

Overview of microRNAs

microRNAs (miRs) are small, non-coding RNAs 20-23 nucleotides long that are loaded into the RNA-induced silencing complex (RISC) to modulate target mRNA expression by binding to their 3'untranslated regions (UTRs) and promoting degradation or preventing translation (Winter et al., 2009). Because a single miR can regulate the expression of multiple mRNAs simultaneously, they are appealing targets to study for the development of novel cancer therapeutics.

Mammalian miRs are encoded in the genome either as individual genes or clusters that can contain up to a few hundred miRs. Clustered miRs are initially transcribed as polycistronic transcripts which are later processed to separate mature miRNAs. Many miRs are transcribed from intronic regions of the genome (Treiber et al., 2019). Transcription is usually carried out by RNA polymerase II to produced capped and polyadenylated primary miRs (pri-miRNAs) which have a hairpin structure (Ha and Kim, 2014). Pri-miRNAs are then processed by the microprocessor protein complex to generate single hairpins known as pre-miRNAs (Lee et al., 2003). Microprocessor consists of RNase III enzyme Drosha, the double-stranded RNA binding protein DiGeorge syndrome critical region gene 8 (DGCR8), and other less well-characterized factors (Denli et al., 2004; Gregory et al., 2004; Han et al., 2004a). pre-miRNAs are then exported to the cytoplasm by export receptor exportin 5 (EXP5) (Bohnsack et al., 2004; Lund et al., 2004; Yi et al., 2003). Then in the cytoplasm, RNase III type enzyme Dicer along with the double-stranded RNA-binding protein (RBP) trans-activation responsive RNA-binding protein (TRBP) processes the pre-miRNA stem to produce a double stranded RNA 20-25 nucleotides long (Grishok et al., 2001; Han et al., 2004b; Ketting et al., 2001). Next, the miR is loaded into RISC. An argonaute (AGO) protein selects one strand (guide strand) of the double stranded miR to become the mature miR, and the other strand (passenger strand) is believed to be discarded (Kobayashi and Tomari, 2016). The now loaded guide strand then leads the RISC complex to sequences complementary to the miR seed (which is found within nucleotides 2 to 7

of the miR) usually within 3'UTRs of target mRNAs (Bartel, 2009). Initially miRS are believed to inhibit the translation of their target mRNAs, but at later stages the target mRNAs can be degraded (Bazzini et al., 2012; Bethune et al., 2012; Djuranovic et al., 2012). Once the RISC complex has been brought to a target mRNA, AGO recruits the glycine-tryptophan (GW) repeat protein trinucleotide repeat containing 6 (TNRC6), which has both an AGO-binding domain and a silencing domain (Pfaff et al., 2013; Schirle and MacRae, 2012). The silencing domain allows for interaction with the poly(A) tail shortening deadenylase complexes (poly(A)-specific ribonuclease (PARN)2-3 or C-C motif chemokine receptor 4-negative regulator of transcription (CCR4-NOT). The shortened or lost poly(A) tail provides a signal for mRNA decapping by the decapping mRNA (DCP)1-DCP2 and DEAD-box helicase 6 (DDX6) containing complex, which is recruited to the 5' end of the target mRNA to remove the 7-methylguanylate cap. The unprotected 5' end is then degraded by a 5'→3' exoribonuclease. DDX6 is important both for inhibiting translation and for promoting mRNA decay (Jonas and Izaurralde, 2015; Treiber et al., 2019).

miRs have been shown to regulate many cancer biology hallmarks, including apoptosis, proliferation, metastasis, and the TME (Pichler and Calin, 2015), including tumor angiogenesis (Collet et al., 2012). In my dissertation, I chose to focus on mechanisms of the miR-200 family modulation of tumor angiogenesis and metastasis.

The microRNA-200 Family and Metastasis

The miR-200 family consists of 5 members and is split into 2 groups: Group A includes miR-200a and miR-141; Group B includes miR-200b, miR-200c, and miR-429. Group A and B members differ by 1 nucleotide in their seed sequences and have both overlapping and non-overlapping targets (Park et al., 2008). The miR-200 family has been implicated in the regulation of many important pathways in cancer progression and metastasis (Humphries and Yang, 2015). miR-200 has been most well-characterized for its roles in inhibiting EMT (Park et al., 2008). EMT

is believed to contribute to cancer metastasis by promoting cancer cell motility and invasiveness by causing cells to undergo changes in morphology and gene expression, including: loss of epithelial cell-to-cell junctions, alteration in cellular polarity, changes in cell cytoskeleton, downregulation of epithelial-related genes (including E-cadherin) and upregulation of mesenchymal genes (including vimentin), increased cellular protrusions, increased cell motility, and increased ability to degrade extracellular matrix (Lamouille et al., 2014). miR-200 has been shown to potently inhibit EMT-related genes such as the transcription factors ZEB1 and ZEB2 which modulate transcriptional repressors of E-cadherin and other EMT-related genes (Park et al., 2008). miR-200's effects on EMT-associated gene expression was shown to inhibit lung adenocarcinoma (LUAD) cell line 344SQ invasion, migration, and metastatic gene expression profiles (Gibbons et al., 2009), and was therefore speculated to be a metastasis suppressor. However, miR-200 has also been shown to promote metastatic colonization of 4TO7 breast cancer cells through inhibition of SEC23A, a component of vesicles involved in cellular transport of secreted proteins including metastasis suppressors tubulointerstitial nephritis antigen like 1 (TINAGL1) and insulin like growth factor binding protein 4 (IGFBP4) (Korpal et al., 2011). Thus, miR-200 regulation of cancer cells has been demonstrated to both inhibit and promote metastasis in different models and cancer types. The authors speculate that this may be due in part to which steps of the metastatic cascade are rate-limiting (Korpal et al., 2011). If the ability of cancer cells to undergo EMT and intravasate into vasculature is more critical to metastasis efficiency, then miR-200 may play more of a suppressive role due to its effects on inhibiting ZEB1 and ZEB2 expression and EMT. If the final steps of distant metastatic colonization are more inefficient, then miR-200 mediated inhibition of metastasis suppressors and promotion of the mesenchymal to epithelial transition (MET) and overall promotion of metastasis may play more of a dominant role.

The Pecot lab discovered a novel role of miR-200 suppression of metastasis through inhibition of tumor angiogenesis and promotion of vascular normalization. miR-200 delivery to cancer cells using neutrally charged 1,2-dioleoyl-sn-glycero-3-phosphatidylcholine (DOPC)

nanoparticles (NPs) potently inhibited primary tumor growth and metastasis with associated decreases in tumor vasculature in orthotopic ovarian and lung cancer models. These effects were due to miR-200 suppression of cancer cell secretion of the pro-angiogenic chemokines IL-8 and CXCL1 (Pecot et al., 2013). In a separate set of experiments, chitosan NPs were used for miR-200 delivery directly to tumor endothelium (as opposed to DOPC NPs which were used for delivery to cancer cells), which again resulted in suppression of primary tumor growth and metastasis and was accompanied by pronounced effects on tumor vasculature, including decreased vessel density, more organized and less tortuous morphology of vessels, increased pericyte coverage, and decreased vessel permeability (Pecot et al., 2013). These effects were speculated to again be due in part to miR-200 inhibition of IL-8 and CXCL1 expression, however the authors of the study hypothesized that other miR-200 targets in tumor endothelium likely also contributed to these effects.

The miR-200 family has previously been demonstrated to regulate general endothelial function, predominately in the context of wound healing and hypoxia, through suppression of direct targets in ECs including E26 oncogene homolog 1 (ETS-1), globin transcription factor binding protein 2 (GATA), VEGFR2, vasohibin-2 (VASH2), and ZEB1, among others (Chan et al., 2011; Chan et al., 2012; Ding et al., 2017; Gill et al., 2012; Magenta et al., 2011). However, in my dissertation, I sought to characterize direct targets regulated by the miR-200 family in ECs specifically in the context of the TME, as such targets remain largely unknown. I chose to focus specifically on miR-200b in my experiments, as the Pecot lab and other groups have observed miR-200b has the most potent effects on EC function of all miR-200 family members (Chan et al., 2011; Chan et al., 2012; Pecot et al., 2013). As described in Chapter 3, my work revealed that the RBP quaking (QKI) is a potently regulated miR-200 target in ECs.

Overview of Quaking and Molecular Function

The *qki* gene was originally discovered due to the occurrence of a spontaneous mutation quaking viable (qk^v) which caused mice to experience epileptic seizures after postnatal day 10. This phenotype was later attributed to poor myelination due to deficient oligodendrocyte function (Sidman et al., 1964). The hypomyelination was revealed to be due to defective mRNA processing, localization, and translation of myelin components in glial cells and thus implicating QKI as a regulator of RNA metabolism (Hardy, 1998; Vernet and Artzt, 1997). The qk^v mutation was determined to be a 1 mb deletion of QKI promoter and enhancer regions that caused disruption of expression of the two alternatively spliced QKI isoforms (QKI-6 and QKI-7, see below) that are usually elevated during myelination and remain most highly expressed in the adult brain (Ebersole et al., 1996; Hardy et al., 1996; Kondo et al., 1999).

QKI is a highly conserved member of the Signal Transduction and Activation of RNA (STAR) family of RBPs expressed as three major alternatively spliced isoforms that are 5 (QKI-5), 6 (QKI-6), and 7 (QKI-7) kb in length (Ebersole et al., 1996; Vernet and Artzt, 1997). The N terminus (first 311 amino acids) of the coding region is identical across all the isoforms and contains 3 conserved functional domains: K homology (KH) RNA-binding domain and QUA1 and QUA2 domains (Ebersole et al., 1996; Kondo et al., 1999; Zorn et al., 1997). The QUA1 domain is necessary for QKI dimerization, while the KH and QUA2 domains direct specific binding to the bipartite sequence RNA motif ACUAAY and “half-site” (UAAY) separated by at least 1 nucleotide (Beuck et al., 2012; Chen and Richard, 1998; Galarneau and Richard, 2005; Teplova et al., 2013). QKI dimerizes when interacting with its mRNA targets and has been shown to only be stable as a dimer in vivo (Beuck et al., 2012; Teplova et al., 2013). QKI also has a proline-rich domain, which suggests an ability to engage in protein-protein interactions (Vernet and Artzt, 1997; Williamson, 1994).

The QKI isoforms differ in their C termini and 3’UTRs. The QKI-5 3’UTR is distinct from the QKI-6 and QKI-7 3’UTRs, and the latter two share more homology with each other. QKI-5

contains a nuclear localization signal within its C terminus and localizes primarily to the nucleus, but it can shuttle between the nucleus and the cytoplasm (Wu et al., 1999). QKI-6 and QKI-7 are predominately cytoplasmic, and there is evidence to suggest that the C terminus of at least QKI-6 may help promote its localization in the cytoplasm (Fagg et al., 2017; Hardy et al., 1996; Pilotte et al., 2001). QKI regulates a wide range of functions related to RNA expression and processing, including RNA alternative splicing (de Bruin et al., 2016a; Hall et al., 2013; Wu et al., 2002), stability (Larocque et al., 2005; Li et al., 2000; Lobbardi et al., 2011; Zearfoss et al., 2011), translation (Saccomanno et al., 1999), nuclear export (Larocque et al., 2002), localization (Li et al., 2000), miR processing (Wang et al., 2013), and circular RNA (circRNA) biogenesis (Conn et al., 2015).

The differing subcellular localizations of the QKI isoforms help confer specificity of function, and changes in the ratios of QKI isoforms can impact their mRNA targets. In general, nuclear QKI-5 is considered most important for regulating splicing and nuclear export/retention, while cytoplasmic QKI-6 and QKI-7 are considered to play more roles in regulating RNA translation and stability. In one study, the authors found that a balance of the different QKI isoforms was required for efficient export of myelin basic protein (MBP) mRNA from the nucleus (Larocque et al., 2002). Overexpression of QKI-5 resulted in increased retention of MBP within the nucleus and caused a decrease in MBP protein expression as well as aberrant MBP protein localization. Overexpression of QKI-6 or QKI-7 in concert with QKI-5 overexpression partially rescued MBP mRNA nuclear export, while simultaneous overexpression of all isoforms completely restored MBP export from the nucleus into the cytoplasm, suggesting the appropriate ratio of all QKI-isoforms is required for appropriate MBP expression (Larocque et al., 2002). In another study, QKI-7 was found to induce apoptosis when present in the cytoplasm, but co-overexpression of QKI-7 with QKI-5 or QKI-6 caused QKI-7 to heterodimerize and redistribute to the nucleus, rendering it incapable of promoting apoptosis (Pilotte et al., 2001). In yet another study, authors characterized a complex self and cross-isoform regulatory

mechanism of QKI expression (Fagg et al., 2017). They observed that isoform-specific knockdown of QKI-5 caused an inhibition of expression of all QKI-isoforms, and that there are predicted QKI binding sites within both the QKI-5 and QKI-6 3'UTRs. At low levels of QKI-5 expression, QKI-5 promoted splicing of its own mRNA to generate higher levels of QKI-5. However, at high levels of QKI-5 expression, QKI-5 bound to its own 3'UTR to inhibit its expression (thus engaging in a negative feedback loop). QKI-6 appeared to negatively regulate QKI-5 protein expression by inhibiting QKI-5 translation while simultaneously stabilizing QKI-5 mRNA transcripts. QKI-6 also promoted its own translation (Fagg et al., 2017).

Role of QKI in Endothelium and in Cancer

Intriguingly, although QKI was initially discovered for its roles in regulating glial cell differentiation, mouse embryos homozygous null or mutant for *qkI* were determined to die *in utero* (in the range of E9.5 to E13.5) due to severe vascular defects (Bohnsack et al., 2006; Li et al., 2003; Noveroske et al., 2002).

In qk^{k2}/qk^{k2} mice which carry a point mutation in the KH domain, Noveroske et. al determined that mice were embryonic lethal due to deficiencies in embryologic vasculature. Normally during embryogenesis, at E9.5 wild type yolk sacs have a well-developed vascular system of endothelial tubes stabilized by recruitment of pericytes and vascular smooth muscle cells. However, in the mutants, although there was a primitive capillary plexus, it was poorly developed and lacked characteristic larger blood vessels, with sparse mural cell recruitment. This was considered to be due to poor remodeling (or angiogenesis) of the initially formed vascular network and/or deficient differentiation or maturation of vascular progenitor cells. Similar deficiencies in vascular remodeling and maturation were also observed in the embryo proper. Immunohistochemistry (IHC) revealed that QKI-5 (the isoform more highly expressed during early embryogenesis) was not expressed in the mesodermal endothelial or mural cells, but was instead expressed in the adjacent endoderm, suggesting QKI may be important for

endodermal signaling to the mesoderm to facilitate vascular progenitor function (Noveroske et al., 2002).

In another study, Li et. al generated a completely null QKI mouse, which was also embryonic lethal. At E9.5 the yolk sacs were lacking in large vitelline vessels and had only a primary vascular plexus, poor vascular remodeling was again observed in the embryo proper, and the connection between the intra-embryonic omphalomesenteric artery (OA) and the extra-embryonic vitelline artery (VA) was disrupted. The authors observed poor smooth muscle cell recruitment to the OA, VA, and dorsal artery, again suggesting poor mural cell recruitment contributed to the defective vascular phenotype. Staining for QKI-5 within wild type embryos revealed expression in ECs and later on in development, smooth muscle cells. Therefore, the authors hypothesized that QKI may play a direct role in smooth muscle cell differentiation to contribute to vascular remodeling. In an aortic explant culture system, the authors observed normal formation of a vascular bed (i.e. early vasculogenesis) suggesting initial differentiation, proliferation, and migration of ECs were not affected. However later stages of vascular network formation were severely impaired and few smooth muscle actin cells developed, suggesting poor vascular progenitor differentiation into mural cells accounted for deficient vascular modeling. In a rescue experiment, CD31/QKI dual positive cells were sorted from wild type E9.05 embryos and added back to the mutant aortic explant system. This resulted in the eventual appearance of smooth muscle cells and restored vascular remodeling. Some of the smooth muscle cells were QKI positive and some were not, suggesting that QKI may elicit intercellular signaling to promote smooth muscle cell differentiation (Li et al., 2003).

In another study Bohnsack et. al characterized both qk^{k2} (mutation in KH domain) and the qk^{l-1} (mutation which inhibits QKI-5-specific alternative splicing) mice and observed similar defects in embryonic angiogenesis. They demonstrate that QKI loss in the endoderm inhibits production of retinoic acid (RA) therefore perturbing RA-mediated signaling from the endoderm to the ECs within the mesoderm to control EC proliferation and allow their maturation. However,

RA did not completely account for all of the vascular remodeling defects or the embryonic lethality, suggesting other QKI targets in EC function were equally if not more important in proper vascular development (Bohnsack et al., 2006).

Apart from QKI's roles in embryologic angiogenesis, QKI has been characterized in a few other endothelial contexts. For example, QKI maintains endothelial barrier function by binding to quaking response elements (QREs) within the 3'UTRs of VE-cadherin and β-catenin and promoting their translation. QKI expression was induced by the exposure of ECs to laminar flow, at least partially due to increased transcription promoted by the flow-induced transcription factor kruppel like factor 2 (KLF2). QKI loss was demonstrated to increase vascular leakage of gut microvascular (de Bruin et al., 2016b). In another study, miR-214 was shown to inhibit endothelial function *in vitro* by targeting QKI expression, which resulted in decreased expression of pro-angiogenic growth factors including VEGFA, bFGF, and PDGF (van Mil et al., 2012). miR-214 was also shown to de-repress QKI-mediated inhibition of vascular smooth muscle cell differentiation. QKI was shown to inhibit transcription of smooth muscle cell specific genes including smooth muscle protein 22 (SM22), serum response factor (SRF), myocyte enhancer factor 2C (MEF2C) and myocardin (MYOCD) (Wu et al., 2017). Finally, QKI-5 has been shown to be upregulated during induced pluripotent stem cell differentiation into ECs by directly binding to the 3'UTR of STAT3 and stabilizing its mRNA. This stabilization of signal transducer and activator of transcription 3 (STAT3) resulted in increased VEGFR expression. QKI-5 overexpressing induced ECs were able to almost completely rescue neovascularization and blood flow recovery in a hind limb ischemia model as well as show increased angiogenesis in a Matrigel plug assay compared to control ECs (Cochrane et al., 2017). Although QKI has been demonstrated to contribute to vascular function, the mechanisms by which it exerts its pro-angiogenic effects remain poorly characterized and are unknown in the context of tumor angiogenesis.

QKI has also been shown to play varying and conflicting roles in cancer progression, including promoting metastasis through activating pro-EMT splicing programs (Pillman et al., 2018), inhibiting lung cancer cell invasion and migration through targeting β-catenin (Zhou et al., 2017), inhibiting lung cancer cell proliferation and Notch signaling activation by regulating NUMB alternative splicing (Zong et al., 2014), and acting as a p53-regulated tumor suppressor in glioblastoma (Chen et al., 2012).

In my dissertation, I sought characterize the function of QKI in regulating tumor angiogenesis specifically within tumor endothelium and to assess the therapeutic implications of targeting tumor endothelial QKI expression to inhibit metastasis and cancer progression.

Therapeutic RNAi for Tumor Angiogenesis Targeting

RNA interference (RNAi) has become an increasingly appreciated therapeutic approach in cancer due to its ability to inhibit targets that traditional therapeutics (such as small molecule inhibitors or monoclonal antibodies) cannot. Therapeutic RNAi relies on delivery of usually small interfering RNAs (siRs) or miRs packaged within NP carriers to silence targets that drive cancer progression. As virtually all mRNAs are susceptible to RNAi-mediated inhibition of expression, independent of their protein function or localization, RNAi demonstrates immense promise as a therapeutic strategy. However, there are still many limitations to therapeutic RNAi that need to be overcome, including poor intracellular delivery, exonuclease degradation of siRs (Pecot et al., 2011), and lack of tissue specificity of NP delivery.

Interestingly, it is the dysfunctional, “leaky” nature of tumor blood vessels as described above that both makes it challenging to deliver drugs such as chemotherapy to the tumor core, but also greatly facilitates delivery of NPs to cancer cells due to the “enhanced permeability and retention effect” (Prabhakar et al., 2013). Oligonucleotide delivery to tumor endothelium has been achieved with multiple NP platforms. Generally, successful delivery of NPs to vasculature is confirmed by visualizing colocalization of fluorescently labeled nucleic acids packaged in NPs

with an endothelial stain such as the cell surface marker CD31. Chitosan NPs have been demonstrated to co-localize to both tumor and ECs in vivo and effectively deliver siRs to both cell types (Lu et al., 2010). In an orthotopic model of ovarian carcinoma, treatment with chitosan NPs carrying siRs targeting human enhancer of zeste 2 polycomb repressive complex 2 subunit (EZH2; expressed in the transplanted cancer cells) or murine EZH2 (expressed in the endogenous murine vasculature) inhibited tumor growth. However, the NPs carrying murine targeting siR had more potent effects on inhibiting disease burden, suggesting chitosan-mediated targeting of tumor vasculature had more potent therapeutic effects than targeting cancer cells directly (Lu et al., 2010). Second-generation NPs rely on incorporation of ligands to target EC-specific surface proteins. For example, ligands to integrin αVβ3, such as the peptide arginine-glycine-aspartate (RGD), can be used to facilitate NP uptake into neo-vasculature. Studies have shown that NPs containing the chemotherapeutic drug doxorubicin can be directed specifically to tumor vasculature using this ligand, causing loss of tumor blood vessels and decreased metastasis (Murphy et al., 2008). Similarly, delivery of an anti-miR to inhibit the pro-angiogenic miR-132 with these same NPs in an orthotopic xenograft mouse model of human breast cancer yielded therapeutic effects on inhibiting tumor vasculature and decreasing tumor burden (Anand et al., 2010). miRs have also been delivered using RGD-labeled chitosan NPs. Delivery of miR-200 family members using this approach reduced angiogenesis by direct and indirect mechanisms and resulted in reduced disease burden in ovarian cancer models (Pecot et al., 2013). RGD-chitosan mediated delivery of siR targeting plexin domain containing 1 (PLXDC1), a growth-promoting gene, has been shown to effectively silence target gene expression in ECs, with subsequent effects on promoting endothelial apoptosis and inhibiting tumor growth (Han et al., 2010). The αVβ3 integrin also facilitates uptake of viral genomic material and therefore may be an effective route for NP-based gene delivery (Stewart and Nemerow, 2007). In one report, delivery of mutant Raf-1 gene with αVβ3- targeted cationic lipid NPs caused apoptosis of vessels and surrounding tumor tissues (Hood et al., 2002). Another

receptor that can mediate uptake into the vascular endothelium is CD31, a classical marker of blood vessels. While αVβ3 is thought to be expressed specifically by tumor neovasculature (as well as some cancer cell types), CD31 is expressed on all endothelium (both blood, and to a lesser extent, lymphatic). Using CD31 ligands to deliver siRs resulted in specific decrease of target genes in vascular endothelium. By delivering a siR against CD31 itself, tumor growth and metastasis were inhibited in a prostate cancer model (Santel et al., 2006). An alternative approach to ligand-based targeting is chemically modified dendrimers that can specifically target the endothelium (Khan et al., 2015). 7C1 NPs are another type of NP that have been reported to localize faithfully and specifically to the endothelium in multiple models of aberrant vascular function, including tumor angiogenesis. These NPs are able to elicit at least 50% knockdown of target endothelial gene expression, and simultaneously deliver siRs targeting multiple genes in the endothelium (Dahlman et al., 2014).

In my dissertation work, I utilized an RNAi therapeutic approach for targeting the miR-200b/QKI axis of regulation in tumor angiogenesis and employed chitosan NPs for tumor endothelial targeting.

CHAPTER 2: MATERIALS AND METHODS[2]

Cell Lines, Maintenance, Transfection Reagents, and *In Vitro* Drug Use

All cell lines were maintained in 5% CO_2/95% air at 37°C. 344SQ LUAD cells were kindly provided by Dr. John Kurie (M.D. Anderson Cancer Center; Houston, TX). 344SQ luciferase-expressing cells were generated by stably transducing 344SQ cells with a lentivirus expressing a green fluorescent protein (GFP)/firefly luciferase construct kindly provided by Dr. Shawn D Hingtgen (University of North Carolina at Chapel Hill, Chapel Hill, NC). 10T1/2 pericyte-like cells and normal human lung fibroblast (NHLF) cells were obtained from the American Type Culture Collection (ATCC). 10T1/2 ZsGreen cells were generated by stably transducing 10T1/2 cells with a ZsGreen construct. Human umbilical vein endothelial cells (HUVEC) were obtained from Lonza. 344SQ cells were maintained in RPMI 1640, NHLF cells in Dulbecco Modified Eagle Medium (DMEM), and 10T1/2 cells in Basal Medium Eagle, all supplemented with 10% fetal bovine serum (FBS) and 1% penicillin streptomycin. HUVEC were maintained in complete endothelial cell growth medium 2 (EGM2) supplemented with the growth factor bullet kit (Lonza) and 10% FBS. All cell lines were tested to confirm the absence of *Mycoplasma*, and all *in vitro* experiments were conducted with 60-80% confluent cultures. All cells were transiently reverse-

[2] The majority of this chapter was slightly modified and previously appeared as part of an article in the journal *Oncogene*. The original citation is as follows: Azam, S.H., Porrello, A., Harrison, E.B., Leslie, P.L., Liu, X., Waugh, T.A., Belanger, A., Mangala, L.S., Lopez-Berestein, G., Wilson, H.L., et al. (2019). Quaking orchestrates a post-transcriptional regulatory network of endothelial cell cycle progression critical to angiogenesis and metastasis. Oncogene.
The "Sprouting Assay" section was slightly modified and previously appeared as part of an article in the *Journal of Visualized Experiments*. The original citation is as follows: Azam, S.H., Smith, M., Somasundaram, V., and Pecot, C.V. (2018). Incorporating Pericytes into an Endothelial Cell Bead Sprouting Assay. J Vis Exp.

transfected with RNAiMax reagent (Invitrogen) using mirVana® mature miR mimic (Ambion, miR-200b, miR-200c, miR-249, or scrambled), anti-miRs (Ambion, negative control anti-miR or anti miR-200b), QKI siRs (Sigma or Ambion Silencer Select, QKI siR #1 sense: 5'CAGGCUGCUCCAAGGAUCAdTdT3', antisense: 5'UGAUCCUUGGAGCAGCCUGdTdT3'; Sigma, QKI siR #2 sense: 5'CUACAGAGAUGCCAACAUUdTdT3', antisense: 5'AAUGUUGGCAUCUCUGUAGdTdT3'; Ambion Silencer Select, QKI-5 siR sense: 5'CUAUUAACCCACAGCAUUAdTdT3', antisense: 5'UAAUGCUGUGGGUUAAUAGdTdT3'; Ambion Silencer Select QKI-6 siR sense: 5'GUGUAUUAGGUAUGGCUUUdTdT3', antisense: 5'AAAGCCAUACCUAAUACACdTdT3'; Ambion Silencer Select QKI-7 siR sense: 5'GAGUGGAUUGAAAUGCCAdTdT3', antisense: 5'UGGCAUUUCAAUCCACUC3dTdT') or a negative control siR (Sigma or Ambion Silencer Select, sense: 5'UUCUCCGAACGUGUCACGUdTdT3', antisense: 5'ACGUGACACGUUCGGAGAAdTdT3') at a final concentration of 20 nM. QKI siRs #1 and #2 targeted sequences that were conserved across all QKI isoforms in both mice and humans; QKI-5, QKI-6, and QKI-7 siRs targeted sequences unique to each mRNA isoform. For rescue experiments, cells were reverse transfected with miR or siR using RNAimax as described above, then the next day cells were forward transfected at a ratio of 2.5 uL of Lipofectamine 2000 (Invitrogen) per 1 µg of plasmid DNA. DNA plasmids used for the cyclin D1 (CCND1) open reading frame (orf) experiments were pCMV-Cyclin D1 (Addgene #19927) and pmCherry-C1 (as empty vector control), DNA plasmids (GeneCopoeia) used for the QKI orf experiments were EX-NEG-Lv224 (as empty vector control), EX-T4215-Lv224 (QKI-5), EX-H2552-Lv224 (QKI-6), and EX-H2553-Lv225 (QKI-7). Media was changed 4-6 hours following transfections to minimize toxicity. For all *in vitro* experiments, palbociclib HCl (MedKoo Biosciences, Chapel Hill, NC, # 202173) was reconstituted at a concentration of 300 nM or 1 µM in dimethylsulfoxide (DMSO). For all serum starve synchronization experiments, HUVEC were serum starved for 24 hours in 1% FBS

(Griffin, 1976). HUVEC were treated with 5-Azacytidine demethylating agent (Sigma #A2385) at working concentrations of 5 or 10 µM for 24 or 48 hours.

Chitosan Nanoparticle (CNP) Preparation

miRs or siRs for *in vivo* EC delivery was incorporated into chitosan (molecular weight 50–190 KDa). CNP was prepared based on ionic gelation of anionic tripolyphosphate and oligos. Briefly, predetermined tripolyphosphate (0.25% w/v) and miRs or siRs (1 µg/µl) were added in chitosan solution, and the miR or siR-CNP were spontaneously formed under constant stirring at room temperature. After incubation at 4 °C for 40 min, miR or siR-CNP was collected by centrifugation (Thermo Biofuge, Germany) at 13,000 r.p.m. for 40 min at 4 °C. The pellet was washed by sterile water 3 times to isolate miR or siR-CNP, which was stored at 4 °C until used.

Animals, *In Vivo* Models and Tissue Processing

Female athymic nude mice were purchased from Jackson Labs and from the UNC Chapel Hill Animal Studies Core. These animals were cared for according to guidelines set forth by the American Association for Accreditation of Laboratory Animal Care and the U.S. Public Health Service policy on Human Care and Use of Laboratory Animals. All mouse studies were approved and supervised by the University of North Carolina at Chapel Hill Institutional Animal Care and Use Committee. All animals used were between 6-10 weeks of age at the time of injection. For all animal experiments, cells were trypsinized, washed, and resuspended in Hanks balanced salt solution (HBSS; Gibco) prior to injection. 344SQ cancer cells were injected either subcutaneously over the posterior flank ($1x10^5$ cells in 100 µL HBSS) or by an intra-pulmonary technique ($5x10^3$ cells in 50 µL for therapeutic experiments or $1x10^5$ in 100 µL for the biodistribution experiment, both in 1:1 mixture of HBSS and BD Matrigel (BD Biosciences). For the intra-pulmonary injections, mice were anesthetized with ketamine (80 mg/kg) + xylazine (8

mg/kg) + acepromazine (1 mg/kg) and placed in the right lateral recumbency. Following sterile skin preparation, an incision parallel to the rib cage between ribs 10-11 was made to visualize the lung through the intact thoracic pleura. A 1 mL tuberculin syringe with a 30-g needle was used to inject the cell suspension directly into the lung parenchyma at the left lateral dorsal axillary line. After injection, the skin incision was closed using surgery clips, and the mice were turned on the left lateral recumbency and observed until fully recovered. Mice were randomized a few days after orthotopic or subcutaneous injection of cancer cells, before initiating treatment. Mice were all combined into one or two cages and then randomly redistributed into treatment groups. Caliper measurements of subcutaneous tumor growth were taken twice weekly and tumor volume was calculated as $L \times W^2$ where L is the greatest cross-sectional length across the tumor and W is the length perpendicular to L. Luciferase-labeled tumor progression was monitored once or twice weekly using an IVIS Lumina optical imaging system and D-Luciferin K^+ substrate (Perkin Elmer, # 122796) as per the manufacturer's instructions. Briefly, substrate was reconstituted at a concentration of 15 mg/mL in phosphate buffered saline (PBS) and 200 µL of substrate were administer via intraperitoneal (IP) injection. Mice were imaged after a 10-minute incubation. Palbociclib HCl (MedKoo Biosciences, Chapel Hill, NC, # 202173) was reconstituted in 50 mM sodium lactate buffer (pH 4.0, Sigma, # 71718) at a concentration of 37.5 mg/mL and was administered at a dose of 150 mg/kg/mouse, daily by oral gavage. CNPs packaged with miR or siR were administered at a dose of 150 ug of oligo/kg/mouse and intravenously, twice a week.

A biodistribution study was performed to assess CNP delivery of oligonucleotides to tumor endothelium in the orthotopic 344SQ lung model. 12 days after cell injection, mice were intravenously administered two doses (24 hours apart) at 200 µg/kg/mouse of Cy3-labeled oligonucleotides packaged in CNP. 24 hours after the second dose, mice were sacrificed and their primary tumors were snap frozen in optimal cutting temperature (OCT, Fisher Healthcare) media. Tumors were assessed for co-localization of Cy3 signal with endothelium.

In all therapeutic experiments 5-15 mice per group were used. Once mice in any group became moribund, they were all sacrificed, necropsied, and tumors were harvested. Tumor weights and number and location of lymphatic and distant metastases were recorded. For TME assessments, mice were injected intravenously with 100 µL of fluorescein isothiocyanate (FITC)-dextran at 10 mg/mL (2,000,000 molecular weight, Life Technologies, # D7137) 1 hour before sacrifice. All tissues used for immunostaining analysis were fixed in 10% neutral buffered formalin, cryoprotected in 30% sucrose, and then slowly frozen at -20°C in OCT.

Quantitative Real-Time Polymerase Chain Reaction (PCR)

For mRNA quantification, total RNA was extracted from cultured cells using the Quick RNA MiniPrep Zymo Research Kit (Genesee Scientific, # 11-328) or from *ex vivo* sorted cells using the Quick RNA MicroPrep Zymo Research Kit (Genesee Scientific, # 11-328M). For coding mRNA gene expression analyses, cDNA was synthesized using an iScript cDNA Synthesis Kit (Bio-Rad, # 1708891) as per the manufacturer's instructions. Analysis of mRNA levels was performed on a StepOnePlus Real-Time PCR System (Applied Biosystems). Specific primers for [QKI-5 (forward)-TACCCTATTGAACCCAGTGGTGT, (reverse)-TCGAACTTTAGTAGCCACCGC; QKI-6 (forward)-ACCCTATTGAACCCAGTGGTGT, (reverse)-TAGCCTTTCGTTGGGAAAGC; QKI-7 (forward)-CCCAGTGGTGTGTTAGAGTGGA, (reverse)-TGAAATATCAGGCATGACTGGC; CCND1 (forward)-GGCGGATTGGAAATGAACTT, (reverse)-TCCTCTCCAAAATGCCAGAG; CCND1 3'UTR (forward)-GGAGGAGGGTTGTGCTACAG, (reverse)- CGCCTCCTTTGTGTTAATGC; ANAPC13 (forward)-GCCACCATTGTCTTGTTCAG, (reverse)-TTTGATTGATGATGCTTGGC; CETN2 (forward)-AGGGCTCATTCTTTTTCGCT, (reverse)-TGTACACGTCGGTTGCCTAA; CKS1B (forward)-GCCAAGATTCCTCCATTCAG, (reverse)-CGACGACGAGGAGTTTGAGT; CDKN2D (forward)-GTCCTGGACATTGGGGCT, (reverse)-AACCGCTTCGGCAAGAC; RAD51 (forward)-

TATCCAGGACATCACTGCCA, (reverse)-GGTGAAGGAAAGGCCATGTA; AURKB (forward)-AGATGGGGTGACAGGCTCTT, (reverse)-AGGAGAACTCCTACCCCTGG; CHTF18 (forward)-ACGCAGGAAGTTGTCAAACA, (reverse)-CTCACAGCGATTCTACCGTG; AVPI1 (forward)-GGTACCCATTGTGGATGCTC, (reverse)-TGAAGGCTGTGGAAGAGGTT; p27 (forward)-AACGTGCGAGTGTCTAACGG, (reverse)-CCCTCTAGGGGTTTGTGATTCT; GAPDH (forward)-TTCCAGGAGCGAGATCCCT, (reverse)-CACCCATGACGAACATGGG; VE Cadherin (forward)- GCACCAGTTTGGCCAATATA, (reverse)-GGGTTTTTGCATAATAAGCAGG] were used for SYBR Green-based real-time PCR, and 18S rRNA (or GAPDH for Supplementary Fig. **2a**) was used as a housekeeping gene. PCR was done with reverse-transcribed RNA, 1 µL each of 20 µM forward and reverse primers, and 2X PowerUp SYBR Green Master Mix (Life Technologies, # 100029284) in a total volume of 25 µL. TaqMan Assays (Applied Biosystems) were used for miR-200b expression (Assay ID # 002251), and U6 snRNA (Asay ID #001973) was used as a housekeeping gene. PCR was done with reverse-transcribed RNA, 20x TaqMan probe, and TaqMan Universal Master Mix II as per the manufacturer's instructions. For both SYBR and TaqMan-based PCR, each cycle consisted of 15 seconds of denaturation at 95°C and 1 min of annealing and extension at 60°C (40 cycles). Reactions were run in duplicate or triplicate.

Target Gene Binding Sites, Luciferase Reporter Assays and 3'UTR Site Mutagenesis

The putative binding sites for miR-200b were predicted bioinformatically using the TargetScan algorithm (publicly available at http://www.targetscan.org) for predicting miR targets and binding sites for QKI. GoClone pLightSwitch luciferase reporters for the QKI 3' UTR reporter was obtained from SwitchGear Genomics (Menlo Park, CA). HEK293 cells (obtained from the ATCC) were transfected with FuGENE HD TFX reagent in a 96-well plate with scrambled control or miR-200b mimics along with the 3' UTR reporter gene and Cypridina TK control

construct (pTK-Cluc). After 48 hours of transfection, luciferase activity was obtained with the LightSwitch Dual Luciferase assay kits using a microplate luminometer per manufacturer guidelines. Two independent experiments were performed with 3 replicates each. An empty luciferase reporter vector was used as a negative control. The ratios obtained were further normalized according to the scrambled control. Mutants of the QKI 3' UTR were generated using the QuikChange Lightning Multi Site-direct Mutagenesis kit (Agilent Technologies, La Jolla, CA) using the following primers to delete 7 nucleotides in a miR-200b binding site: (forward) cttttgaaatctctgaatgccttggttctatcattctttattgaatttatttcttatta; (reverse) taataagaaataaattcaataaagaatgatagaaccaaggcattcagagatttcaaaag. Proper site mutagenesis was confirmed with sequencing prior to luciferase assays.

Western Blotting

After reverse transfection, cells were lysed by scraping in RIPA buffer (ThermoFisher, # PI89901) containing 1x cOmplete Mini protease inhibitor cocktail (Roche, # 11836153001). Equal amounts of lysates (10-40 µg of total protein) were run on 4-20% SDS-PAGE gradient gels, after which protein was transferred to nitrocellulose membranes (BioRad, Hercules, CA). Membranes were blocked in 5% milk/Tris-buffered saline-Tween 20 (TBS-T) for one hour at room temperature prior to probing with primary antibodies overnight at 4°C. Primary antibodies included pan-QKI (Clone N147/6, # 75-168, Neuromab), QKI-5 (rabbit anti-QKI, Millipore, # AB9904), QKI-6 (rabbit anti-QKI, Millipore, # AB9906), QKI-7 (mouse anti-QKI, Neuromab, # 75-200), Cyclin D1 (# 2922s, Cell Signaling Technology, Danvers, MA), and anti-vinculin (clone hVIN-1, # V9131, Sigma), all at a 1:1000 dilution in blocking buffer. After probing with primary antibodies, membranes were washed three times in TBS-T and then probed with the appropriate horseradish peroxidase-conjugated secondary antibodies (anti-mouse [# 115-035-003] or anti-rabbit [# 111-035-003] from Jackson ImmunoResearch) diluted 1:5,000 to 1:10,000.

Then, the membranes were washed four times in TBS-T and developed using Clarity Western ECL substrate (BioRad, Hercules, CA, # 1705060). Membranes were visualized using a BioRad ChemiDoc MP system (BioRad, Hercules, CA). Densitometry quantifications were determined using Fiji software.

Proliferation Assays

Transfected or treated HUVEC were seeded at a density of 5,000 or 7,500 cells per well in 12-well plates in triplicate and counted on a hemocytometer using Trypan Blue counterstain.

Cell Cycle Analysis

Cells were fixed in cold 70% EtOH and stored at -20°C until ready for staining. Cells were washed with PBS and incubated with staining solution (Propidium iodide [Roche, # 11348639001 stock concentration 500 µg/mL, working concentration 50 µg/mL] and RNAse A [Qiagen, stock concentration 100 mg/mL, working concentration 100 µg/mL] diluted in PBS) for 30 minutes at room temperature in the dark. Stained cells were analyzed on a Beckman Coulter CyAn ADP.

RNA Immunoprecipitation

RNA immunoprecipitation assay was performed using the Magna Rip Kit (Millipore Sigma, # 17-700) per the manufacturer's instructions using the following antibodies for QKI isoform pulldown: QKI-5 (rabbit anti-QKI, Millipore, # AB9904), QKI-6 (rabbit anti-QKI, Millipore, # AB9906), and QKI-7 (rabbit anti-QKI, Millipore, #AB9908).

Argonaute-2 Immunoprecipitation

One or two confluent 10 cm plates of cells were washed with cold PBS and ultraviolet (UV) crosslinked at 400J. Cells were washed with cold PBS again, scraped into 15 mL conical tubes, and centrifuged at 810 g for 5 minutes. Cell pellet was resuspended in 1 mL cold Ago immunoprecipitation buffer (50 µM HEPES, 100 µM NaCl, 0.5% NP40), vortexed, and incubated on ice for 20 minutes with intermittent vortexing. Samples were centrifuged at maximum speed for 30 seconds. Supernatants were collected and incubated with 10 µL of Ago2 Mab (Diagenode, #c15200167) on ice for 1 hour. Next, 25 µL of Protein A dynabeads (Invitrogen, #10001d) and 25 µL of Protein G dynabeads (Invitrogen, #10003d) were mixed together and washed 2 times with cold Ago immunoprecipitation buffer. Samples were then added to the beads and rotated at 4°C for 30 minutes. Beads were then washed 2 times with cold Ago immunoprecipitation buffer and then 2 times with 0.5 M NaCl Ago immunoprecipitation buffer. Beads were then resuspended in 100 µL Ago immunoprecipitation buffer, 200 µL Trizol, and 50 µL of chloroform. Samples were vigorously vortexed and centrifuged at 12000g 4°C for 15 minutes. The top aqueous layer was removed and mixed with 5 µL glycogen and100 µL isopropanol and centrifuged at 12000g 4°C for 10 minutes. The pellet was washed 1X in 75% EtOH and then resuspended in 10 µL. All the resulting RNA was loaded into an iScript cDNA reaction and subjected to qPCR analysis.

mRNA Stability Assay

CCND1 mRNA stability was assessed using the Click-it Nascent RNA capture kit (Life Technologies, # C10365) according to the manufacturer's instructions.

In Vivo Angiogenesis Plug Assay

A 450-500 µL solution of Matrigel containing 500 ng/mL rVEGF 165 containing DMSO or 300 nM palbociclib was subcutaneously implanted on to the flanks of nude mice. 8 days after implantation, the plugs were extracted and snap frozen. Plugs were then dissociated using Dispase (Worthington Biochemical, # LS02104) and hemoglobin content was quantified using the QuantiChrom Hemoglobin Assay Kit (BioAssay Systems, # DIHB-250) according to the manufacturer's instructions.

Sprouting Assay

Both the standard and pericyte-coated sprouting assays were performed, quantified, and immunostained as described in (Azam et al., 2018) and the detailed steps are presented below. Beads in proximity to one another or near the edge of the imaging well were excluded from analysis due to possible confounding effects on sprouting. Primary antibodies used for immunofluorescence staining include CD31 (mouse anti-human, Dako, clone # JC70A, 1:1000) and Ki-67 (rabbit anti-mouse, 1:200, Abcam ab15580). Secondary antibodies used include goat anti-rabbit Alexa 488 (Molecular Probes, #A10034, 1:600) and goat anti-mouse Alexa 594 (Molecular Probes, #A11005, 1:600).

Day 1:

1. Transient Transfection of Endothelial Cells

1.1. If desired, perform a transient transfection of Human Umbilical Vein Endothelial Cells (HUVEC) using gene-regulatory oligonucleotides (*e.g.* micro-RNAs or small interfering RNA (siRNA)) and the appropriate lipofectamine reagent according to manufacturer's instructions. Note: This protocol has had great success performing reverse transfections with custom siRNA sequences and a commercial transfection reagent. The authors have not tested other

transfection protocols and reagents with this assay. The steps for the reverse transfection using the reagents listed are as follows:

1.2. Reconstitute lyophilized siRNAs or microRNAs at a concentration of 20 µM in nuclease free water.

1.3. Make transfection solutions at the following ratio: 1 mL of any serum free media with 9 µL of siRNA or microRNA.

1.4. Agitate the solution and allow it to incubate for 5 min at room temperature.

1.5. Add 18 µL of transfection reagent to the solution and agitate.

1.6. Allow the solution to incubate at room temperature for 20-40 min, agitating the solution every 10 to 15 min for the duration of the incubation.

1.7. While the transfection solution is incubating, detach HUVEC using a cell detachment solution (*e.g.*, Accutase). For a T175 flask, wash the flask with 10 mL of Phosphate Buffered Saline (PBS), and then add 5 mL of cell detachment solution and incubate the flask at 37 °C for 10 min.

1.8. Add 5 mL of complete media to the T175 flask, remove the cell suspension from the flask and centrifuge at 1200 rpm for 3 min.

1.9. Remove the supernatant using a vacuum aspirator and resuspend the cell pellet at a density of 1 X 10^6 cells per mL in EGM2.

Note: This protocol has had great success using Endothelial Cell Growth Medium (EGM2) containing the standard growth factor bullet kit as well as an additional 10% FBS.

1.10. Once the transfection solution has finished incubating, plate 1 mL of solution in a 10-cm plate, and add 1 mL of HUVEC suspension on top.

1.11. Add an additional 7 mL of complete media to bring the final volume in the 10-cm plate to 9 mL.

1.12. Make up at least two 10 cm plates worth of cells for each transfection condition to ensure that there are enough cells available for later steps in the assay.

Note: These conditions result in a final working concentration of gene regulatory oligonucleotide of 20 nM. The authors have found these conditions to result in a 60-80% knockdown of gene expression for their targets of interest. Other researchers may need to optimize transfection conditions according to their experimental needs.

1.13. Exchange the media 4-6 h post addition of siRNA complexes with fresh complete media.

Note: This protocol was developed using passage 1 - 2 HUVEC.

Day 2

2. Coating of Microcarrier Beads with Endothelial Cells

2.1. Reconstitute microcarrier beads (*e.g.*, Cytodex 3) at a concentration of 60,000 beads/mL in PBS and autoclave.

Note: microcarrier beads come at a concentration of approximately 3 x 10^6 beads per gram. Reconstitute the beads at a ratio of 20 mg of beads per mL of PBS to get a bead density of approximately 60,000 beads/mL.

2.2. Aliquot 1 mL of complete media into the desired number of round-bottomed Fluorescence Activated Cell Sorting (FACS) tubes.

2.3. Pipette 20 µL of microcarrier bead suspension into each tube (take care to ensure that the bead solution is well resuspended prior to pipetting).

Note: There will likely be dramatic variability in the final working concentration of beads present in a given microcarrier bead suspension. Beads can easily adhere to the sides of plastic and glass container which can greatly alter bead concentration in the solution. The most appropriate volume of bead solution added to the FACS tube for each batch of microcarrier bead suspension will need to be determined empirically by the investigator. The numbers presented here are meant to serve more as a starting point. Ideally, conditions should be optimized so there are 10-20 beads embedded within the fibrin gel per well in the 24 well plate at the end of the assay.

2.4. Detach transfected HUVEC 24 h post transfection using the cell detachment solution as follows:

2.4.1. Wash each 10-cm plate of cells with 5 mL of PBS, and then add 2 mL of the cell detachment solution and incubate the cells at 37 °C for 10 min.

2.4.2. Resuspend the cells at a concentration of 1 X 10^6 cells/mL in complete media.

2.5. Add 1 mL of cell suspension (*i.e.* 1 X 10^6 HUVEC) to each FACS tube.

2.6. Gently agitate the FACS tubes every 20 min for the duration of 4 h at 37 °C (if proceeding to step 3.4) or 2.5 to 3 h (if proceeding to step 3.2).

Note: This duration and frequency of agitation has been empirically determined by previous researchers who have optimized the basic bead sprouting assay. Other frequencies of agitation and durations of the bead coating step have not been tested by the authors.(Nakatsu and Hughes, 2008)

3. Sequential Coating of Pericytes on HUVEC-Coated Microcarrier Beads

3.1. Begin detaching 10T1/2 cells (pericytes) using the cell detachment solution (trypsin) as follows:

3.1.1. Wash a T175 flask with 10 mL of PBS, then add 5 mL of trypsin and incubate at 37 °C for 10 min.

3.1.2. Resuspend 10T1/2 at a concentration of 2 X 10^5 cells/0.5 mL in complete media.

Note: Cells were purchased from the ATCC.

Note: Culture 10T1/2 cells in Minimum Essential Medium (MEM) supplemented with 10% FBS and 1% Penicillin Streptomycin.

3.2. After 2.5 to 3 h of agitating the bead + HUVEC solution, wait 5 min to allow the beads and free-floating HUVEC to settle to the bottom of the tube.

3.3. Remove 0.5 mL of complete media using a P1000 pipette and add 2 X 10^5 10T1/2 in complete media in a volume of 0.5 mL to each FACs tube. Continue to agitate every 20 min until the beads have been agitated for a total of 4 h.

Note: The ratio of 5 HUVEC: 1 pericyte on the beads is essential to maintain appropriate pericyte coverage of the vessels.

Note: The following alternative steps can be followed instead at this point in the protocol:

3.4. Agitate beads and HUVEC only for 4 h.

3.5. Once the 4 h of HUVEC coating of the microcarrier beads is complete, agitate the tubes one last time, wait 30-60 s, then immediately remove 1.5-1.75 mL of solution from the FACS tube.

Note: This should allow enough time for most of the beads to settle while many free-floating HUVEC in the media will be removed.

3.5.1. Add 2 X 10^5 10T1/2 in complete media and bring the volume of the FACS tube up to 2 mL.

3.5.2. Gently agitate the FACS tubes every 20 min for an additional hour.

3.6. Once the agitating is complete, gently agitate the tubes one last time and immediately remove the entire solution (2 mL), and add it to a 6-cm plate. Add an additional 3 mL of complete media to each plate and place the plates in the 37 °C incubator overnight.

Day 3

4. Preparation of Fibrin Gel Solutions

4.1. Prepare working solutions of aprotinin at a concentration of 1 mg/mL in PBS and thrombin at 50 units/mL.

Note: A large stock of each of these solutions can be made and stored at 4 °C for at least a year.

4.2. Make a fresh solution of fibrinogen at a concentration of 2 mg/mL. Make enough solution to have 2.5 mL of solution per agitated FACS tube.

4.2.1. Warm the solution in a 37 °C water bath for 10 min to allow all of the fibrinogen to go into solution.

4.2.2. Add 37.5 µL of aprotinin solution per 1 mL of fibrinogen solution.

4.2.3. Sterile-filter the solution and set aside at room temperature.

5. Preparing Beads for Gel Implantation

5.1. Examine the dishes containing the microcarrier-coated beads under the microscope using the 20X objective to ensure that all beads have been sufficiently coated by endothelial cells.

5.2. Vigorously pipette the plated solution of cells to detach them from the 6-cm plate and place the solution into a FACs tube. Wash the plate 2X additional times with complete media and transfer to the FACS tube to collect all residual beads that may be adhered to the plate.

5.2.1. Avoid introducing air bubbles and use a p1000 pipette to minimize shear stress on the endothelial cell-coated beads.

5.2.2. If assessing siRNA knockdown efficiency in the endothelial cells is needed, in step 2, be sure to have a plate of HUVEC-only coated beads. Then during this step (5.2), detach the beads and collect the residual HUVEC attached to the plate for RNA isolation and qPCR analysis.

5.3. Wait 3 min to allow the beads in the solution to settle to the bottom of the tube.

5.4. Remove as much of the supernatant as possible without disturbing the bead pellet using a p1000 pipette tip (do not use a vacuum aspirator).

5.5. Add 1 mL of complete media to each tube and resuspend the beads.

5.6. Wait 30-60 s to allow the beads to settle to the bottom. Then remove as much of the supernatant as possible using a P1000 pipette without disturbing the bead pellet. Do not use a vacuum aspirator as the likelihood of accidentally removing the bead pellet is greatly increased.

5.7. Repeat Steps 5.5 and 5.6 two additional times. The goal is to remove as much of the free-floating HUVEC that may have been detached from the 6-cm plate as possible, while not removing too many HUVEC-coated beads, which should settle in the FACS tube more quickly than free-floating cells.

5.8. Add 1 mL of complete media to the beads.

6. Embedding Coated Beads in a Fibrin Gel

6.1. Remove as much media as possible without disturbing the bead pellet in each FACS tube using a P1000 pipette.

6.2. Resuspend the beads in 2.5 mL of fibrinogen solution.

6.3. Pipette 13 µL of thrombin solution into each desired well of a 24-well glass-bottomed plate. Plating in a glass-bottomed plate is essential for enabling optimal imaging of the sprouts.

Note: Do not leave thrombin sitting in a well for more than 5-10 min before the next step.

6.4. Add 0.5 mL of bead/fibrinogen solution to each well.

6.4.1. Be sure to resuspend the bead solution well prior to pipetting the solution each time.

6.4.2. Take caution to carefully pipette directly into the thrombin already present in the well. Slowly pipette up and down 2-3 times to thoroughly mix the solution, taking caution to not introduce any air bubbles.

6.4.3. Be sure to change the pipette tip between wells.

6.4.4. Take caution to not move or disturb the plate at any point during initial fibrin clotting, as any movement may disrupt the gel formation.

6.5. Leave the plate sitting in the hood for 30 min at room temperature.

6.6. Carefully transfer the plate to a 37 °C incubator for an additional 1.5-2 h to allow the gel to fully solidify

7. Plating Fibroblasts on Top of the Fibrin Gel

7.1. During the last 30 min of the gel solidifying, detach Normal Human Lung Fibroblasts (NHLF) as follows:

7.1.1. Wash a T175 flask of cells with 10 mL of PBS, then add 5 mL of cell detachment solution and incubate at 37 °C for 10 min.

7.1.2. Resuspend NHLF at a concentration of 20,000 cells/mL in complete media.

Note: NHLF cells can be cultured with Dulbecco Modified Eagle Medium (DMEM) supplemented with 10% FBS and 1% Penicillin Streptomycin.

7.2. Plate 1 mL of the NHLF cell suspension onto the gel of each well and place back in the incubator.

7.3. Change complete media every other day for the duration of the assay.

8. Observe sprouting over the course of 2-7 days following bead implantation in the fibrin gel. The length of time required for sprouting will depend on the passage and lot number of HUVEC.

9. Fixation of Sprouting Assay

9.1. Once sufficient sprouting has occurred to be able to determine a phenotypic difference between treatment groups, wash all wells one time with 2 mL of PBS.

9.2. Add 0.5 mL of cell detachment solution to each well and place the plate in a 37 °C incubator for 5 min.

9.3. Remove the plate from the incubator and tap the sides of the plate.

Note: The purpose of this step is to remove as many of the NHLF cells growing on top of the fibrin gel as possible to facilitate antibody penetration into the gel as well as imaging of the gel. The total incubation time with cell detachment solution may need to be adjusted to optimize NHLF removal. Researchers are cautioned to not incubate the gel for excessive periods of time as the cell detachment solution may penetrate into the gel and begin disrupting the endothelial structures within.

9.4. Once a sufficient amount of NHLF cells have been removed, quench the cell detachment solution with 1 mL of complete media.

9.5. Aspirate the detached NHLF and media using a vacuum aspirator, and wash the wells once with 1 mL of PBS.

9.6. Add 300 µL of 2% paraformaldehyde solution in PBS to each well and incubate at room temperature for 10 min.

9.7. Remove the 2% paraformaldehyde solution and wash each well 3 times with 1 mL of PBS for 3 min at room temperature.

Note: Please dispose of 2% paraformaldehyde solution appropriately in accordance with Environmental Health and Safety (EHS) guidelines.

9.7.1. Add 1 mL of PBS to each well and store at 4 °C until ready to stain or image the sprouts.

10. Staining of Sprouting Assay

10.1. Add 300 µL of 0.5% Triton-X 100 in PBS to each well and incubate for 30 to 45 min at room temperature.

10.2. Using a vacuum aspirator, remove Triton-X100 and wash 3 times in PBS for 5 min each.

10.3. Add 500 µL of blocking solution to each gel and incubate overnight at 4 °C.

Note: The blocking solution is made up of the following components: 1% bovine serum albumin (BSA), 5% FBS, 0.1% tween-20, and 1% antiserum (use the same species from which your secondary antibodies are derived) in PBS.

10.4. Remove blocking solution from each well and add 300 µL of staining solution containing primary antibody to each well.

Note: The staining solution is the same as the blocking solution, but without the antiserum present. The authors have had success incubating with primary antibodies at dilutions of 1:200 to 1:400.

10.5. Incubate primary antibodies in staining solution for 24 h at 4 °C.

10.6. Aspirate primary antibody solution and wash 3 times in TBS with 0.5% tween for 20 min each at room temperature with gentle rocking. After the third wash, replace with fresh wash buffer again, and store at 4 °C overnight.

10.7. Incubate with fluorescent secondary antibody diluted 1:1000 in staining solution for 2 h at room temperature.

10.8. Remove secondary antibody staining solution and wash 5 times for 20 min each with TBS containing 0.5% tween at room temperature with gentle rocking.

10.9. Dilute nuclear stain in PBS and incubate overnight at 4 °C.

Note: This protocol has had great success with Hoechst diluted 1:10000 in PBS.

Note: There is no need to remove nuclear staining solution prior to imaging.

10.10. Image within a few days of completing the staining to capture optimal fluorescent signal.

11. Sprouting Assay Quantification

11.1. After the sprouts have been imaged, import the image files into ImageJ and use the Count tool to count the number of sprouts, or the Line tool to measure sprout lengths.

Note:

Sprouts are defined as endothelial protrusions with a length greater than or equal to the diameter of the bead from which they are sprouting (Popson et al., 2014), or as protrusions greater than or equal to 100 µm. Sprout length can be measured as the distance from the point at which the sprout begins protruding from the bead to the tip of the sprout. Average sprout length per bead and average number of sprouts per bead are useful metrics to assess phenotypic effects of gene silencing in sprouting angiogenesis. The average number of beads containing at least one sprout per treatment group can also be used as a metric to assess the robustness of sprouting.

Important factors to consider:

When performing the assay, it is essential that efficient endothelial coating of the beads takes place during the bead agitation steps. Poor endothelial coating will be made evident if the beads do not appear to have a golf ball-like rough surface the next morning prior to gel implantation and instead appear completely smooth. Take care to ensure that the beads are sufficiently resuspended during each agitation step by vigorously agitating the tubes to allow maximum exposure of the bead surface to the endothelial cells, but not so aggressively that it causes the endothelial cells already attached to become detached from the beads.

When adding pericytes into the assay, it is essential that the ratio of 5 endothelial cells to 1 pericyte is maintained. An excess of pericytes causes them to overgrow and overtake the endothelial cell populations during the assay, and a deficiency in pericytes causes poor coverage of the vessels. If the appropriate cell density is maintained but poor pericyte coverage

of the vessels is still observed, agitation time with pericytes may need to be modified. It is not recommended that the cell numbers are altered. An alternative approach may be to coat the beads with endothelial cells only for 4 h, then remove the endothelial cells from the media by resuspending the bead and cell solution and removing the media once the beads have settled but before the cells have settled, then adding in pericytes and agitating every 20 min for an additional hour.

When embedding the coated beads in the fibrin clot, it is also essential to not disturb the integrity of the gel by disrupting the plate during clot formation. Disruption of the matrix formation may result in aberrant sprouting. It is also essential to ensure that the appropriate bead density is maintained in the gel. If the population of beads is too dense, then beads in close proximity to one another will affect the sprouting of neighboring beads and will begin to sprout towards one another and anastomose. Depending on the ultimate goal of the researcher and interest in characterizing vessel-vessel interactions, the bead density may need to be modified. However, a heterogeneous population of isolated beads and beads in close proximity to one another within the gel may give largely variable sprouting phenotypes. Bead density can be adjusted by altering the volume of bead solution added to the FACS tubes during the agitation step of the protocol, or by altering the volume of fibrin solution used to resuspend the beads prior to gel implantation.

It is also essential that healthy NHLFs at a density of 20,000 cells per mL are plated on top of each fibrin clot. Please note that the continuous supply of growth factors supplied by the actively dividing NHLFs are necessary for robust sprouting during the assay. NHLF-conditioned EGM2 is not a sufficient alternative.(Newman et al., 2011) If poor sprouting is observed during the assay, it is recommended that a fresh bottle of complete media and a new, healthy passage of NHLF cells are used.

The conditions described within this protocol are important to adhere to obtain sufficiently-coated beads that will be able to undergo robust sprouting in the fibrin gel. The

authors have found that an excess of pericytes (such as pericytes coated at a ratio of 1 10T1/2 to 1 HUVEC) result in pericyte overgrowth of the entire well and subsequent inability to discern distinct vascular structures within the well.

Immunostaining

Staining was performed in OCT-embedded frozen tissue sections (10-20 µm thick) either with or without prior formalin fixation and 30% sucrose cryoprotection. Sections were permeabilized with cold acetone for 10 minutes. For immunohistochemistry, 3% H_2O_2 was used to block endogenous peroxidase activity for 10 minutes. Avidin Biotin blocking was performed using an Avidin/Biotin blocking kit (Vector Labs, # sp-2001) per the manufacturer's instructions. Protein blocking of non-specific epitopes was performed using 4% fish gelatin in PBS for 20 minutes. Slides were incubated with primary antibody for overnight at 4ºC. After washing with PBS, the appropriate amount of biotinylated secondary antibody was added, and the signal was amplified using an ABC kit (Vector Labs, # PK-6200) per the manufacturer's instructions. The slides were then visualized with 3,3'-diaminobenzidine chromogen (Vector Labs, # SK-4105), counterstained with Gill's hematoxylin #3, and mounted with Permount medium. For immunofluorescence, after acetone permeabilization, protein blocking using 4% fish gelatin was performed, and slides were incubated with primary antibody overnight at 4ºC. After washing with PBS, secondary antibody staining was performed in blocking buffer for 1 hour at room temperature. Hoechst 33342 (BD Pharmingen, 1:10,000, # 561908) was used for nuclear staining. Slides were mounted with Prolong Gold (Invitrogen). A Leica DMi8 inverted microscope was used for both fluorescent and light microscopy.

Primary antibodies used include the following: desmin (rabbit anti-mouse, 1:200, Abcam, # 15200), CD31 (rat anti-mouse, 1:400, BD Pharmingen # 553370 for non-fixed tissues or rat anti-mouse, 1:50, BD Pharmingen # 550274 for fixed tissues), and carbonic anhydrous IX (CA9) (Novus Biologicals, 1:1000, # NB100-417SS). Immunofluorescent secondary antibodies used

include the following: goat anti-mouse Alexa 594 (Molecular Probes, # A11005 ,1:600); goat anti-rat Alexa 488 (Molecular Probes, # A11006, 1:500); and goat anti-rat Alexa 594 (Molecular Probes, # A11007, 1:600). The horseradish peroxidase-conjugated secondary antibody used was Biotinylated anti-Rat IgG (Vector Labs, # BA-9401, 1:100)

To quantify microvessel density (MVD), I examined fields at 20x magnification for each tumor in a blinded fashion and counted the microvessels within those fields. A vessel was defined as an open lumen with at least one adjacent CD31-positive cell. Multiple positive cells beside a single lumen were counted as one vessel. To quantify pericyte-covered vessels, I determined the percent of vessels in each field that had at least 50% pericyte-coverage. To quantify FITC-dextran extravasation, I measured the total area of FITC signal per field of view. Enumeration of CD31- and CA9-positive cells per high powered field were determined using a pipeline in CellProfiler 3.0 software (Lamprecht et al., 2007). In general, 4-5 mice were analyzed per experimental group for all immunofluorescent and immunohistochemistry analyses, and 10-20 images were analyzed per mouse.

Adenoviral Cre Recombinase Induction

Adeno Cre virus was complexed with 0.016 M CaCl2 (i.e. 0.6 µL of 2 M CaCl2 in 75 µL of DMEM) in serum free DMEM for 20 minutes and administered intranasally to *Lox*-Stop-*Lox* $Kras^{G12D}$; $Lkb1^{L/L}$; $p53^{L/L}$ mice at a final concentration of 5 X 10^6 plaque-forming units per mouse. Mice were induced at age 6 weeks.

Flow Cytometry

Resected murine tissue (lung tumor for tumor EC samples; healthy lung tissue for normal EC samples) was washed with serum free DMEM on ice. Tissues were placed in a 10 cm plate with 2.2 mL of digestion buffer (1 mL DMEM, 1 mL collagenase type II [Worthington

Biochemical, # 4176] at 2 mg/mL in HBSS, 200 µL dispase [Worthington Biochemical, # LS02104] at 2.5 U/mL in HBSS, and 15 µL DNase [Worthington Biochemical, # EPO0366360] at 1mg/mL in PBS) and mechanically dissociated using a sterile scalpel blade. The resulting solution was transferred to a 15 mL conical tube and incubated at 37°C with shaking for 1 hour. The digested solution was filtered through a 40 µm cell strainer. The filter was rinsed once with an additional 10 mL of FACS buffer (0.5% BSA and 2 mM EDTA in PBS) to collect any residual cells adhered to the filter. The cell suspension was spun at 1200 RPM for 5 minutes. The supernatant was removed and the resulting cell pellet was resuspended in 2 mL of ACK Lysis buffer and incubated for 2 minutes at room temperature. Then 3 mL of FACS buffer was added, and the solution was spun at 1200 RPM for 5 minutes. The supernatant was removed and the resulting cell pellet was resuspended in 100 µL of FACS buffer. Then 10 µL of mouse FcR block was added and the solution was incubated for 10 minutes on ice. Then staining antibodies were added to the cell solution: AlexaFluor 488 rat anti mouse LYVE-1 (1:20, R&D Systems, # FAB2125G), APC rat anti-mouse EpCAM (1:100, Abcam, # ab95641), PE rat anti-moue CD31 (1:100, BD Pharmingen, 553373), and PerCP-Cy 5.5 rat anti-mouse CD45 (1:100, BD Pharmingen, # 550994). Cells were stained for 1 hour in the dark on ice, with agitation every 15-20 minutes. Cells were washed with FACS buffer and resuspended in a final volume of 300 µL FACS buffer and filtered through a cell strainer. Cells were sorted on a Beckman Coulter MoFlo and were sorted into EGM2 media. ECs were identified as CD45-/ epithelial cellular adhesion molecule (EPCAM)-/CD31+/lymphatic vessel endothelial hyaluronan receptor 1 (LYVE1)-. OneComp eBeads (Thermo Fisher Scientific, # 01-1111-41) were used for single color gating controls.

All clinical samples were collected following patient consent on an approved University of North Carolina Institutional Review Board (IRB) protocol. Resected patient tissue (lung tumor for tumor EC samples; healthy lung tissue for normal EC samples) was washed with serum free

DMEM on ice. Tissues were placed in a 10 cm plate with 2.2 mL of digestion buffer (1 mL DMEM, 1 mL collagenase type II [Worthington Biochemical, # 4176] at 2mg/mL in HBSS, 200 µL dispase [Worthington Biochemical, # LS02104] at 2.5 U/mL in HBSS, and 15 µL DNase [Worthington Biochemical, # EPO0366360] at 1mg/mL in PBS) and mechanically dissociated using a sterile scalpel blade. The resulting solution was transferred to a 15 mL conical tube and incubated at 37°C with shaking for 1 hour. The digested solution was filtered through a 40 µm cell strainer. The filter was rinsed once with an additional 10 mL of FACS buffer (0.5% BSA and 2 mM EDTA in PBS) to collect any residual cells adhered to the filter. The cell suspension was spun at 1200 RPM for 5 minutes. The supernatant was removed and the resulting cell pellet was resuspended in 2 mL of ACK Lysis buffer and incubated for 2 minutes at room temperature. Then 3 mL of FACS buffer was added, and the solution was spun at 1200 RPM for 5 minutes. The supernatant was removed and the resulting cell pellet was resuspended in 100 µL of FACS buffer. Then staining antibodies were added to the cell solution: FITC mouse anti-human EPCAM (1:5, BD Biosciences, # 347197), PerCP-Cy5.5 mouse anti-human CD45 (1:20, BD Biosciences, # 564105), AlexaFluor 647 mouse anti-human CD31 (1:20, BD Biosciences, # 561654), PE rabbit anti-human LYVE-1 (1:25, Novus, # NB100-725PE), BioLegend Zombie Aqua viability dye (1:16.7, Biolgened, # 423101). Cells were stained for 1 hour in the dark on ice, with agitation every 15-20 minutes. Cells were washed with FACS buffer and resuspended in a final volume of 300 µL FACS buffer and filtered through a cell strainer. The samples were sorted on a Becton Dickinson FACSAria II and were sorted directly into RNA lysis buffer. ECs were identified as CD45-/EPCAM-/CD31+/LYVE-1-. ArC Amine Reactive Compensation Bead Kit (Life Technologies, # A10346) was used for compensation control for the viability dye. OneComp eBeads (Thermo Fisher Scientific, # 01-1111-41) were used for single color gating controls.

μCT Imaging

Micro computed tomography imaging was performed by the UNC Biomedical Research Imaging Center on a GE eXplore CT120. The chest cavity was imaged as the region of interest, and respiration gating was used.

mRNA Microarray

Total RNA was extracted from HUVEC using the Quick RNA MiniPrep Zymo Research Kit (Genesee Scientific, # 11-328). RNA purity was assessed by a Nanodrop (Thermo Scientific) spectrophotometric measurement of the OD260/280 ratio, with acceptable values falling between 1.9 and 2.1. RNA was then submitted to the UNC Functional Genomics Core for further analysis and processing. The RNA integrity number (RIN score) was determined using an Agilent TapeStation 2200 with acceptable values considered to be above 7.5. Total RNA (580 ng) was used to synthesize fragmented and labeled sense-strand cDNA and hybridize onto Affymetrx arrays (AffyMetrix HuGene 2.1 ST 16-Array Plate) per the manufacturer's instructions.

RNA-Sequencing

HUVEC were serum starved for 24 hours in 1% FBS (Brooks, 1976; Campisi et al., 1984; Griffin, 1976), then transfected with NC siR or QKI siR#1 and lysed 24 hours post transfection. 5 NC siR and 5 QKI siR#1 samples were collected (each sample consisted of two 10 cm plates worth of cells). RNA was isolated using the Quick RNA MiniPrep Zymo Research Kit (Genesee Scientific, # 11-328) and ribosomal RNA was removed using the RiboMinus Eukaryote Kit for RNA-Seq (Life Technologies, # A10837-08) according to the manufacturer's instructions. The remaining total RNA was then submitted to the UNC High Throughput Sequencing Facility. The RNA underwent library preparation and was submitted for sequencing

on the HiSeq2500 Illumina platform (https://www.illumina.com/). Samples were multiplexed and pooled across two lanes with a cycle number of 100x (paired ends).

Tissue Microarray

Tissue microarray (TMA) samples for lung squamous cell carcinoma (LUSC) and LUAD cancers were obtained and prepared following IRB approval for UNC Chapel Hill. The TMAs were then submitted to UNC's Tissue Pathology Laboratory (TPL) for staining and analysis. The TMAs were stained with the following: CD31 (mouse monoclonal anti human CD31 clone JC70A, # M082329-2, DAKO, Santa Clara, CA), pan-QKI (mouse monoclonal anti pan-QKI clone N147/6, # 75-168, Neuromab); and pan cytokeratin (CK; mouse monoclonal anti panCK, clone AE1/AE3, # M3515, Agilent Technologies/ DAKO, Santa Clara, CA). Single IHC and triple immunofluorescence (IF) (3plex IF) stains were carried in the Leica Bond-III fully automated staining platform (Leica Biosystems Inc., Norwell, MA). Slides were dewaxed in Bond™ Dewax solution (# AR9222) and hydrated in Bond Wash solution (# AR9590). Epitope retrieval for pan-QKI was done for 20 minutes and for the remaining targets for 30 minutes in Bond-epitope retrieval solution 1 pH6.0 (# AR9661). The epitope retrieval was followed with 10 minutes endogenous peroxidase blocking using Bond peroxide blocking solution (# DS9800) and 10 minutes protein blocking (DAKO, # X0909). For the 3-plex CK-pan-QKI-CD31 IF stain, the application order, primary antibody dilution, incubation times of the primary and secondary antibodies, and TSA systems used were the following: (1) panCK, 1:1000, 1 hour, Bond post primary (# DS9800) for 8 minutes, Bond polymer (# DS9800) for 8 minutes, and TSA-Cy3 (1:50) (Perkin Elmer, # SAT704A001EA; (2) pan-QKI, 1:400, 30 minutes, Bond post primary (# DS9800) for 8 minutes, Bond polymer (# DS9800) for 8 minutes and TSA-Cy5 (1:50)-15 minutes (Perkin Elmer, # SAT705A001EA and (3) CD31, 1:50, 2 h, Bond post primary (# DS9800) for 8 minutes, Bond polymer (# DS9800) for 8 minutes, and Tyramide Reagent Alexa

Fluor™ 488 (1:100) 15 minutes (Invitrogen, # B40953). Between stains the appropriate antigen retrieval and peroxide blocking steps were inserted. Stained slides were counterstained with Hoechst 33258 (Invitrogen, # H3569) and mounted with ProLong® Gold Antifade Mountant (Invitrogen, # P36930). Single IF stain controls were performed to ensure that cross reactivity between antibodies did not occur. Positive and negative controls (no primary antibody) were included for the stains. High resolution acquisition of CK-pan-QKI-CD31 IF slides in the DAPI, AF 488, Cy3 and Cy5 channels was performed in the Aperio ScanScope FL (Leica Biosystems) using the 20X objective. Nuclei were visualized in the DAPI channel (blue), CD31 in AF 488 (green), panCK in Cy3 (cyan) and pan-QKI in Cy5 (red).

Scanned images were archived in TPL's eSlide Manger database (Leica Biosystems). TMA images were segmented into individual cores using the Tissue Studio IF TMA portal (Tissue Studio version 2.7 with Tissue Studio Library version 4.4.2; Definiens Inc., Carlsbad CA). CK and CD31 staining were used to digitally separate tissue cores into panCK positive (tumor), CD31 positive, and stromal regions (Tissue Studio Composer, Definiens). Automated digital analysis of individual tissue cores was run separately in these three regions of interest (ROIs). Tissue Studio software, specifically the Nuclei and Simulated Cells algorithm in the IF TMA Portal, was then used to detect and enumerate cells that expressed pan-QKI in each ROI. Briefly, nuclei were digitally detected by the presence of Hoechst stain (nuclear counterstain). From these nuclei, a cell simulation was performed – cell margins were grown out from nuclear boundaries. For this data set, positivity thresholds for pan-QKI were determined by measuring the staining intensities both inside and outside simulated cells. Once thresholds were set, the algorithm evaluated each cell individually for the presence of pan-QKI positive signal. Cells were separated by the algorithm into negative, low positive, medium positive, or high positive categories based on the intensity of pan-QKI.

Affymetrix Microarray

The Affymetrix HuGene 2.1 ST 16-Array (http://www.thermofisher.com/us/en/home.html) was used for measuring the gene expression of HUVEC transfected with a) Negative Control (NC) miR for 24 hours (4 biological replicates), b) miR-200b for 24 hours (3 biological replicates), and c) miR-200b for 48 hours (3 biological replicates).

Statistical Analyses

Between 5 and 10 mice were assigned per treatment group; this sample size gave approximately 80% power to detect a 50% reduction in tumor weight with 95% confidence. Results for each group were compared using a Student's t test (for comparisons of two groups) and analysis of variance (for multiple group comparisons). For values that were not normally distributed (as determined by the Kolmogorov-Smirnov test), the Mann–Whitney rank sum test was used. A P-value less than 0.05 was deemed statistically significant. All other statistical tests for *in vitro* and *in vivo* experiments were performed using GraphPad Prism 7 (GraphPad Software, Inc., San Diego, CA). All line and bar graphs represent mean values, and all error bars represent standard error of the mean.

CHAPTER 3: RESULTS[3]

miR-200b is Downregulated in Endothelium During Lung Cancer Progression

To investigate the importance of endothelial miR-200b expression during tumor development, I intranasally delivered adenoviral Cre recombinase to *Lox*-Stop-*Lox* $Kras^{G12D}$; liver kinase B1 $(Lkb1)^{L/L}$; $p53^{L/L}$ mice to generate an autochthonous model of LUAD (Ji et al., 2007). I collected tumor-bearing lungs at early and late stages of disease progression (4 and 8 weeks, respectively, post adenoviral Cre delivery), as well as age-matched healthy lungs from non-induced control littermates (Figure 1a). I verified disease progression over time by micro computed tomography (μCT) imaging of the outgrowth of primary tumors in the lung (Figure 1b). Employing FACS, I isolated healthy lung normal ECs (LNECs) as well as tumor ECs (TECs) derived from early and late-stage tumor-bearing mice (Figure 1c). qPCR analysis of the collected ECs revealed that while miR-200b was largely unchanged in early-stage TECs relative to age-matched LNECs, miR-200b expression was significantly down-regulated by more than 50% in TECs isolated from late-stage LUAD tumors compared to age-matched LNECs (Figure 2a). To determine whether this finding was clinically relevant, I assessed miR-200b expression in surgically resected lung cancer samples from 3 patients and found that miR-200b expression was significantly downregulated in FACS-sorted TECs relative to patient-matched LNECs

[3] This chapter was slightly modified and previously appeared as part of an article in the journal *Oncogene*. The original citation is as follows: Azam, S.H., Porrello, A., Harrison, E.B., Leslie, P.L., Liu, X., Waugh, T.A., Belanger, A., Mangala, L.S., Lopez-Berestein, G., Wilson, H.L., et al. (2019). Quaking orchestrates a post-transcriptional regulatory network of endothelial cell cycle progression critical to angiogenesis and metastasis. Oncogene.

(Figure 2b). These data demonstrate that miR-200b is downregulated in TECs during tumor progression and further implicate miR-200b as a modulator of pro-angiogenic pathways.

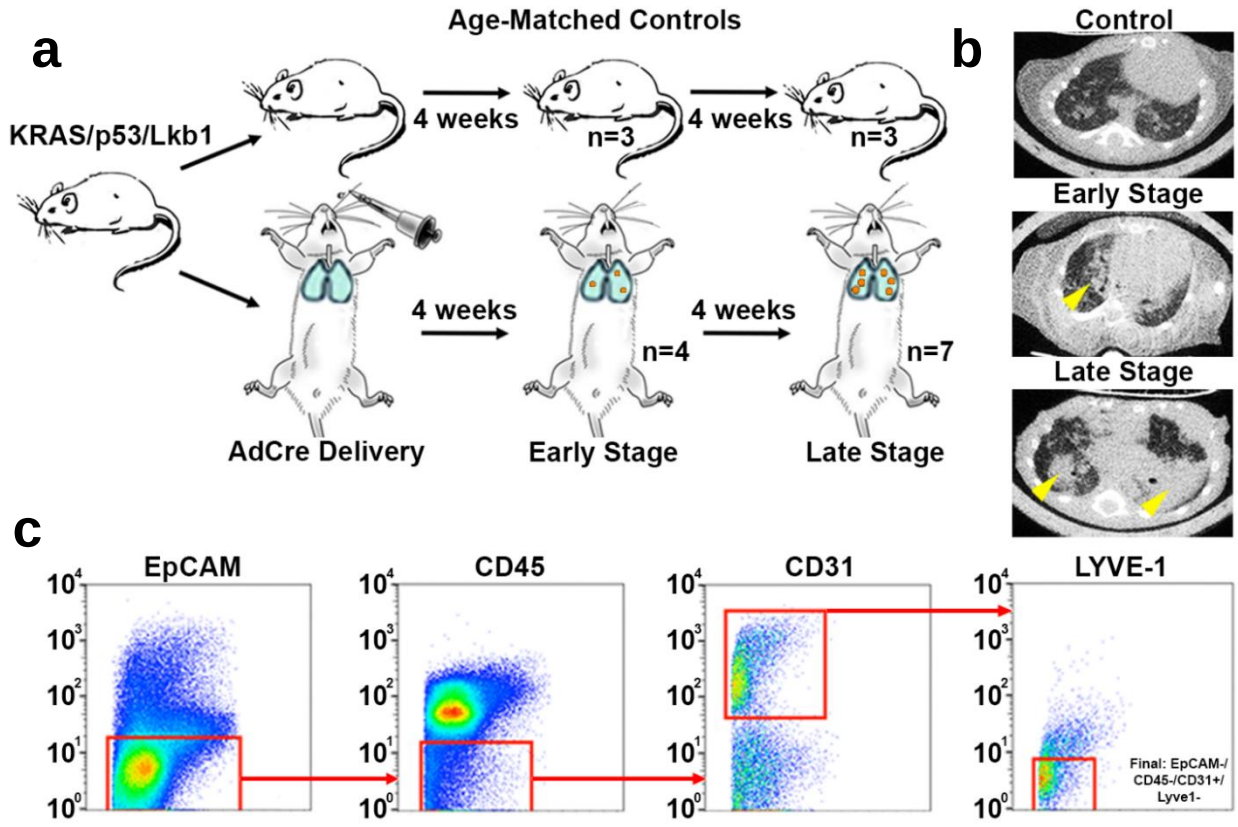

Figure 1. The KRAS;p53;LKB1 mouse can be used to model early and late stage tumor angiogenesis.

a Schematic for genetically engineered mouse model of LUAD disease progression and number of mice per treatment group. Intranasal delivery of adenoviral Cre recombinase to *Lox*-Stop-*Lox* $Kras^{G12D}$; $Lkb1^{L/L}$; $p53^{L/L}$ mice was used to initiate tumorigenesis. Non-induced littermates were used as age-matched controls.

b µCT imaging of adenoviral Cre-treated mice demonstrates increased lung cancer progression over time. Yellow arrowheads indicate presence of tumor. *Imaging was performed with the help of UNC's Biomedical Research Imaging Center.*

c Representative image of FACS gating strategy for isolating ECs from murine and human lung tumors and normal lungs. ECs were defined as cluster of differentiation (CD)45 negative/epithelial cell adhesion molecule (EPCAM) negative/CD31 POSITIVE/lymphatic vessel endothelial hyaluronan receptor 1 (LYVE1) negative populations. LYVE1 was used as a final negative selection marker to remove possible contaminating lymphatic ECs from the desired vascular EC population. *Flow cytometry was performed with the help of UNC's Flow Cytometry Core*

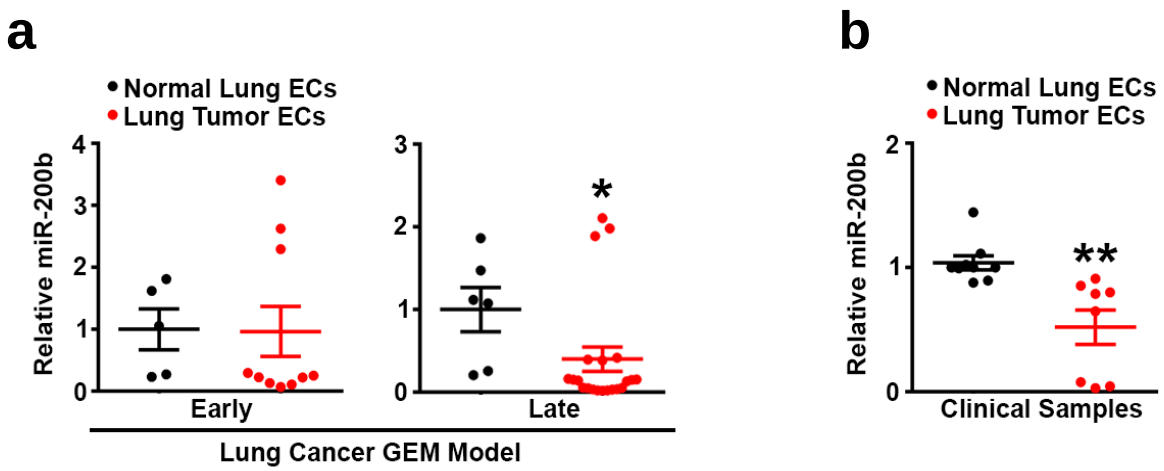

Figure 2 miR-200b is downregulated in tumor endothelium.

a qPCR analysis for miR-200b in ECs isolated from early and late stage lung tumors from a genetically engineered mouse (GEM) LUAD model and age-matched littermate healthy lungs (early, n=2 control mice, n=4 disease mice; late, n=4 control mice, n=7 disease mice; data points represent qPCR technical duplicates or triplicates per mouse).

b qPCR analysis for miR-200b in tumor and matched healthy lung ECs from lung cancer patients (n=3 patients, data points represent qPCR technical duplicates or triplicates per patient).

Statistical significance was measured by Mann-Whitney test; p-values are indicated as *p<0.05, **p<0.01, ***p<0.001; error bars represent standard error of the mean.

Quaking is a miR-200b Target in Tumor Endothelium

To investigate clinically relevant targets of miR-200b with roles in tumor angiogenesis, the Pecot lab performed an integrated analysis of The Cancer Genome Atlas (TCGA) datasets using 3 highly angiogenic and metastatic cancer types: basal-like breast, lung, and high-grade serous ovarian carcinomas. Previously, the Pecot lab had identified protein-coding genes that had a strong inverse correlation of expression with any of the 5 members of the miR-200 family (false discovery rate [FDR] <0.01, Benjamini-Hochberg multiple testing correction) and performed *in silico* enrichment for genes that were predicted to be putative miR-200 target genes as determined by *TargetScan* (Pecot et al., 2013). Using Ingenuity Pathway Analysis (IPA) of these prior identified genes, the Pecot lab generated a network visualization of all enriched genes associated with angiogenesis based on their Gene Ontology terms (Figure 3a). This list was then filtered for genes that were predicted to be regulated by miR-200 family members in all 3 cancer types, producing a list of 4 leading candidates (Table 2 and Figure 3b). Of these 4 genes, 2 genes were predicted to be regulated by a much larger number of miR-200 family members: QKI and ZEB2 (Table 2). ZEB2 is a well-characterized target of the miR-200 family that has been extensively studied for its role in EMT (Gregory et al., 2008; Park et al., 2008). Because the TCGA analyses reflected miR:mRNA interactions across all cellular compartments of the TME, I next transfected ECs with negative control (NC) or miR-200b and performed microarray analyses (Figure 3c) to identify putative miR-200 targets with direct relevance in endothelium. Both QKI and ZEB2 were potently downregulated upon miR-200b transfection into ECs (Figure 3c), thus implicating their importance as clinically relevant targets in the context of the endothelial compartment of the TME.

QKI was the top ranked target gene identified in the IPA assessment of the TCGA datasets based on it being a predicted target amongst the majority of miR-200 family members across the 3 cancer types (Table 2). *TargetScan* analysis revealed that there are 4 predicted miR-200b binding sites in QKI-5 isoform 3'UTR and 2 predicted miR-200b binding sites in a

conserved region across the QKI-6 and QKI-7 isoform 3'UTRs. Although QKI has been demonstrated to play a vital role in embryologic angiogenesis (Bohnsack et al., 2006; Li et al., 2003; Noveroske et al., 2002) and to regulate EC biology (Cochrane et al., 2017; de Bruin et al., 2016b; van Mil et al., 2012), the mechanisms by which QKI regulates normal vascular function are poorly understood and remain entirely unknown in the context of tumor angiogenesis. I therefore investigated the role of QKI as a miR-200b target in the context of the TME. I found that transient transfection of miR-200b into ECs dramatically downregulated expression of all QKI mRNA isoforms in a time-dependent manner (Figure 4a and b) as well as protein expression of all QKI isoforms (Figure 4c). miR-200b overexpression also inhibited expression of a QKI 3'UTR luciferase reporter, and this suppression was abrogated upon deletion of predicted miR-200b binding sites in the QKI 3'UTR (Figure 4d). I next performed an AGO2 immunoprecipitation to verify binding of miR-200b to each QKI mRNA isoform within RISC. I observed an enrichment of all QKI isoforms upon AGO2 pulldown in miR-200b-transfected ECs compared to NC miR-transfected ECs (Figure 4e). In addition, treatment of ECs with an anti-miR inhibiting expression of miR-200b significantly increased expression of all QKI mRNA isoforms relative to treatment with a scrambled anti-miR (Figure 5a). I also observed that transient transfection of ECs with miR mimics of the other group B members of the miR-200 family (miR-200c and miR-429) also significantly downregulated expression of all QKI mRNA isoforms (Figure 5b), further validating QKI is potently regulated by the miR-200 family in endothelium. These results also align with previous findings suggesting QKI-5 is directly regulated by miR-200c during EMT in cancer cells (Pillman et al., 2018). Altogether, these data validate QKI as a direct miR-200b target in ECs with potential clinical relevance in tumor angiogenesis. Intriguingly, I also found that direct QKI suppression using two different pan-QKI siRs resulted in an inhibition of miR-200b expression in ECs (Figure 5c). These results raise the possibility that there may in fact be a regulatory feedback loop between QKI and miR-200b, which needs to be further characterized in future studies.

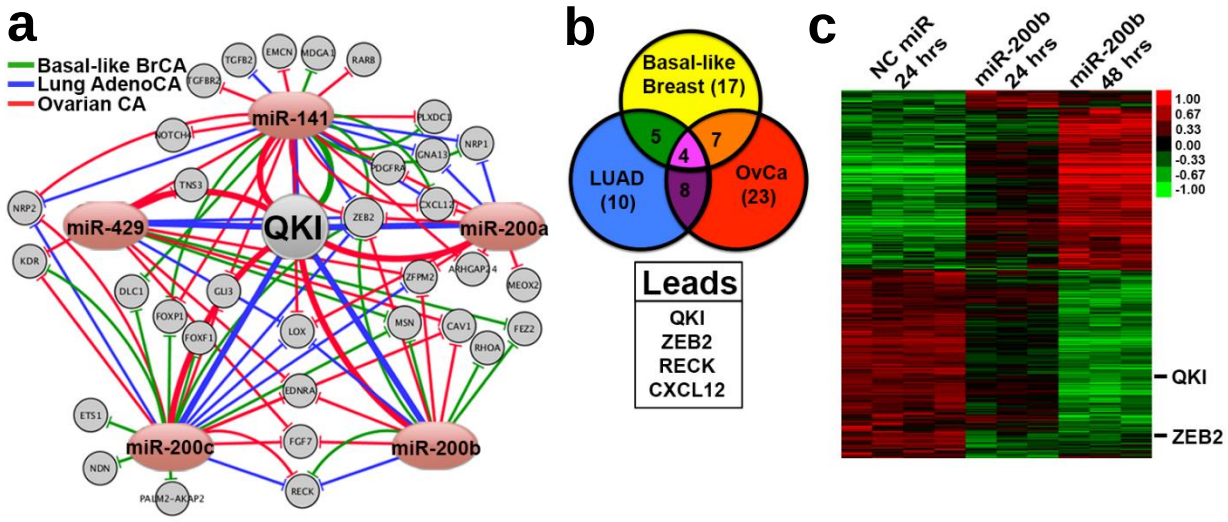

Figure 3 QKI is a predicted miR-200b target in cancer and in endothelium.

a Protein-coding genes with a strong inverse correlation of expression with any of the 5 members of the miR-200 family using the TCGA datasets for LUAD, high-grade serous ovarian and basal-like breast carcinoma (FDR<0.01, Benjamini-Hochberg multiple testing correction) have been previously identified (Pecot et al., 2013). in silico enrichment for genes that were predicted to be putative miR-200 target genes as determined by TargetScan was then performed. These putative target genes were then assessed using Ingenuity Pathway Analysis for statistically significant Gene Ontology pathways (Pecot et al., 2013). The angiogenesis network visualization was performed by selecting all genes within each angiogenesis-related Gene Ontology term for each of the 3 cancer types. Cytoscape software was used for the network visualization to display the numbers of times each miR-200 family member was predicted to target each gene (Shannon et al., 2003). Connecting lines represent relationships of inverse correlation of expression, and line thickness represents strength of correlation. Pink ovals represent members of the miR-200 family. Gray circles represent putative miR-200 targets. *Cytoscape revisualization and analysis was performed by Chad Pecot.*

b List of overlapping lead miR-200 candidate targets identified in **a** in all 3 cancer types.

c Heatmap of the microarray analysis performed on HUVEC transfected with Negative Control (NC) miR or miR-200b. Lead candidates that overlap with **c** are demarcated with black lines. Samples were run in triplicate or quadruplicate. *Microarray samples were hybridized by UNC Genomics Core. Heatmap analysis was performed by Alessandro Porrello.*

Table 2 TCGA Predicted miR-200 Family Targets

Predicted mRNA Target (miR score*)	Cancer Type	miR-200 Family Member
QKI (11)	Basal-Like Breast	miR-141
	Lung Adenocarcinoma	miR-141 miR-200a miR-200b miR-200c miR-429
	Ovarian	miR-141 miR-200a miR-200b miR-200c miR-429
ZEB2 (9)	Basal-Like Breast	miR-141 miR-200b miR-200c
	Lung Adenocarcinoma	miR-141 miR-200c miR-429
	Ovarian	miR-141 miR-200a miR-200b
LOX (5)	Lung Adenocarcinoma	miR-200b miR-200c miR-429
	Ovarian	miR-141 miR-200a
CXCL12 (4)	Basal-Like Breast	miR-141
	Lung Adenocarcinoma	miR-141
	Ovarian	miR-141 miR-200a
NRP2 (4)	Lung Adenocarcinoma	miR-141 miR-200c
	Ovarian	miR-141 miR-200c
RECK (4)	Basal-Like Breast	miR-200b
	Lung Adenocarcinoma	miR-200b miR-200c
	Ovarian	miR-200c
ZFPM2 (4)	Lung Adenocarcinoma	miR-200c
	Ovarian	miR-200a miR-200b miR-429
CAV1 (3)	Ovarian	miR-200b miR-200c miR-429
EDNRA (3)	Ovarian	miR-200b miR-200c miR-429

Predicted mRNA Target (miR score*)	Cancer Type	miR-200 Family Member
FGF7 (3)	Ovarian	miR-200b miR-200c miR-429
FOXP1 (3)	Basal-Like Breast	miR-141 miR-200c
	Ovarian	miR-141
KDR (3)	Basal-Like Breast	miR-200c
	Ovarian	miR-141 miR-200c
MSN (3)	Basal-Like Breast	miR-200b miR-200c miR-429
NRP1 (3)	Basal-Like Breast	miR-141
	Lung Adenocarcinoma	miR-141 miR-200a
ARHGAP24 (2)	Ovarian	miR-141 miR-200a
DLC1 (2)	Basal-Like Breast	miR-141 miR-200c
FEZ2 (2)	Basal-Like Breast	miR-200b miR-429
GLI3 (2)	Ovarian	miR-141 miR-200c
GNA13 (2)	Lung Adenocarcinoma	miR-141 miR-200a
PDGFRA (2)	Ovarian	miR-141 miR-200a
PLXDC1 (2)	Basal-Like Breast	miR-141
	Ovarian	miR-141
EMCN (1)	Ovarian	miR-141
ETS1 (1)	Basal-Like Breast	miR-200c
FOXF1 (1)	Basal-Like Breast	miR-200c
MDGA1 (1)	Basal-Like Breast	miR-141
MEOX2 (1)	Ovarian	miR-200a
NDN (1)	Basal-Like Breast	miR-200c
NOTCH4 (1)	Ovarian	miR-141
PALM2-AKAP2 (1)	Basal-Like Breast	miR-200c
RARB (1)	Ovarian	miR-141
RHOA (1)	Basal-Like Breast	miR-200b
TGFB2 (1)	Lung Adenocarcinoma	miR-141
TGFBR2 (1)	Ovarian	miR-141
TNS3 (1)	Ovarian	miR-429

*miR scores were calculated by adding the number of predicted targeting miR-200 family members in each cancer type.

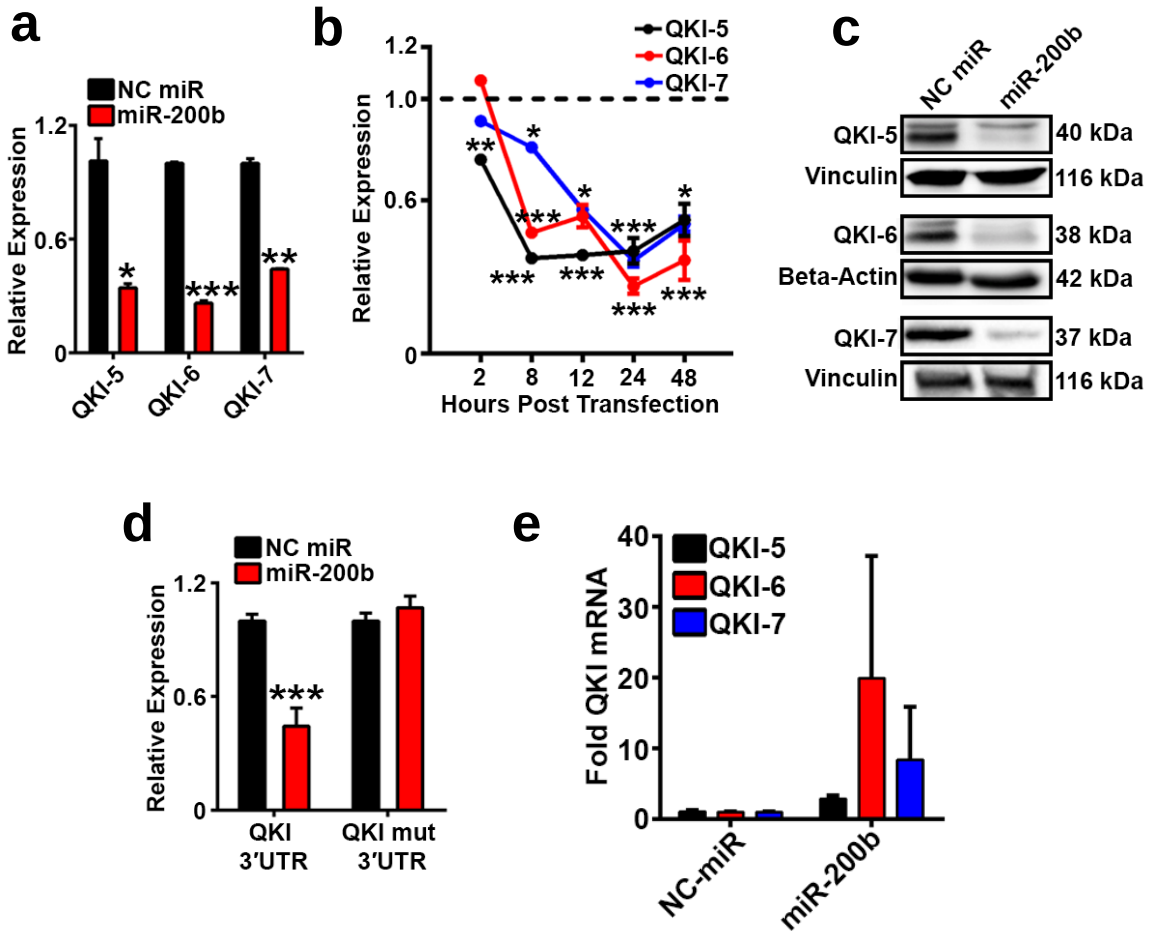

Figure 4 QKI is a direct miR-200b target in endothelium.

a – b qPCR analysis of QKI mRNA isoform expression in HUVEC transfected with NC miR or miR-200b at 24 hours or between 2-48 hours. (**a** shows representative results from two independent experiments)

c Western blot of QKI protein isoform expression in HUVEC following transfection with NC miR or miR-200b.

d QKI 3'UTR or QKI 3'UTR mutated luciferase reporter activity in HEK293 cells transfected with NC miR or miR-200b. Luciferase signal was measured 48 hours post transfection of luciferase-expressing plasmids and miRs (shows representative results from two independent experiments).

e qPCR to detect QKI mRNA isoform enrichment from AGO2 immunoprecipitations in miR-200b transfected HUVEC relative to NC-miR transfected HUVEC. Glyceraldehyde-3-phosphate dehydrogenase (GAPDH) expression was used as a housekeeping control. Cells were lysed 24 hours post transfection. Shows aggregate results from 2 independent experiments

Statistical significance was measured by unpaired t-tests; p-values are indicated as *p<0.05, **p<0.01, ***p<0.001; all qPCR and luciferase assays were run in duplicate or triplicate; error bars represent standard error of the mean.

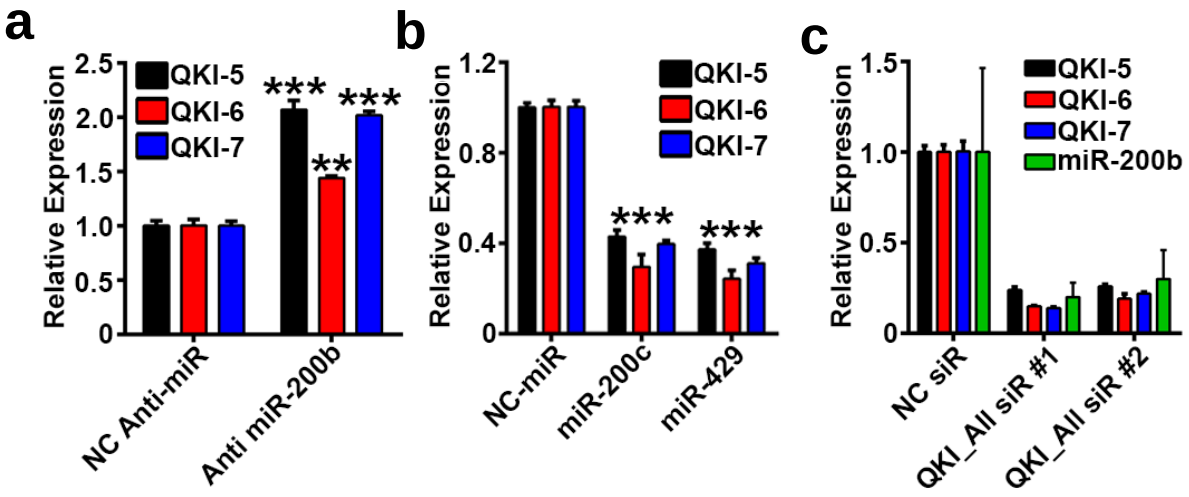

Figure 5 QKI and miR-200 expression.

a qPCR for QKI expression in HUVEC transfected with control or anti-miR targeting miR-200b (48 hours post transfection).

b qPCR for QKI expression in HUVEC transfected with miR-200 B family members miR-200c and miR-429 (24 hours post transfection). Shows aggregate results from 2 independent experiments.

c qPCR for miR-200b and QKI expression in HUVEC transfected with control or QKI siRs (48 hours post transfection).

All qPCR assays were run in triplicate. Statistical significance was measured by unpaired t-tests; p-values are indicated as *p<0.05, **p<0.01, ***p<0.001; error bars represent standard error of the mean.

QKI Silencing Recapitulates the Effects of miR-200b on EC Sprouting

I next determined whether QKI knockdown mimics the effects of miR-200b on EC function *in vitro*. I found that pan-QKI isoform knockdown phenocopied miR-200b activation by reducing the number of elongated sprouting vessels per bead in a 3-dimensional bead assay of sprouting angiogenesis (Nakatsu et al., 2007) (Figure 6a). I found that dual treatment with both miR-200b and QKI siR did not further abrogate EC sprouting compared to miR-200b treatment alone (Figure 6b). Recently, I optimized a new version of this sprouting assay to also incorporate pericytes, which more accurately models the complex heterotypic cellular interactions involved in angiogenesis *in vivo* (Figure 7; see detailed method in Chapter 2: Materials and Methods, subsection Sprouting Assay) (Azam et al., 2018). Both QKI silencing and miR-200b overexpression in the ECs in pericyte-associated sprouts dramatically altered endothelial sprouting (Figure 8a). Intriguingly, QKI silencing in pericytes alone also resulted in reduction of vessels per bead (Figure 8b), suggesting QKI may also play a role in modulating the function of mural cells associated with blood vessels. These results demonstrate that QKI expression is important for promoting angiogenesis and that QKI inhibition plays a significant role in the effects of miR-200b-mediated inhibition of EC (and pericyte) function and angiogenesis.

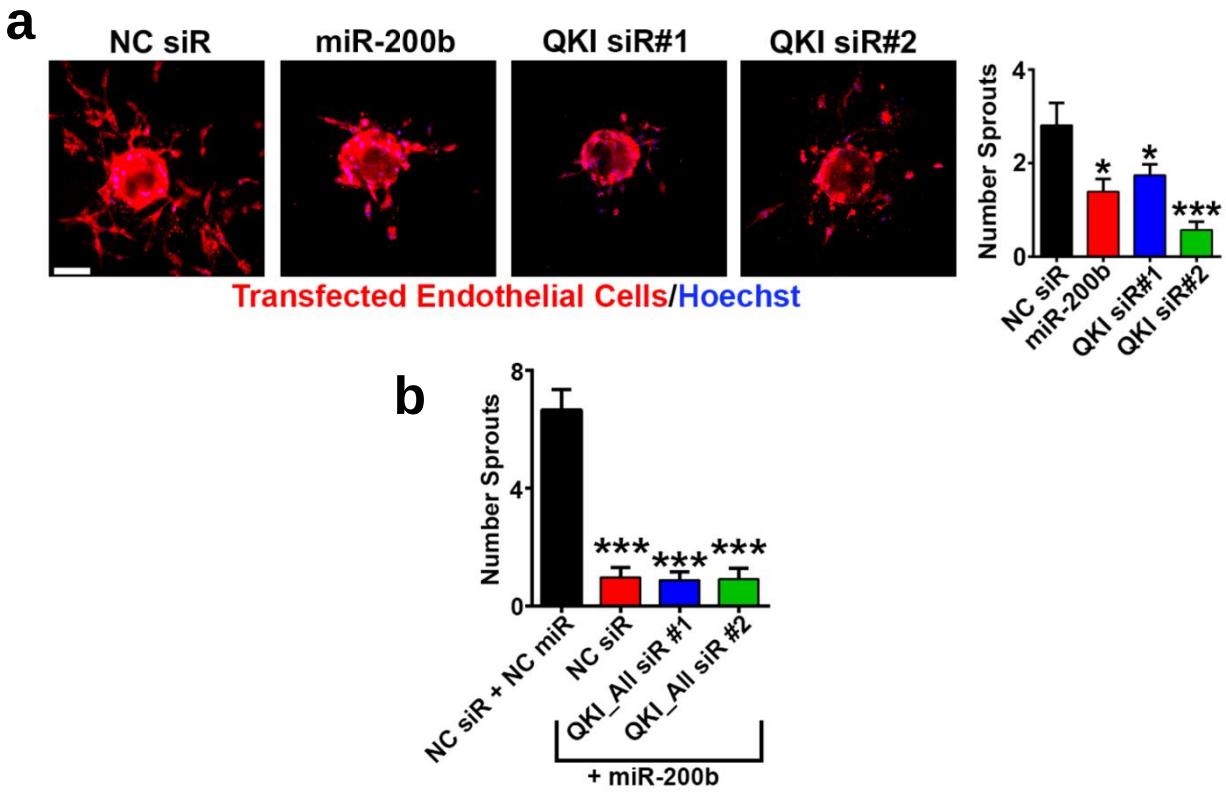

Figure 6 QKI silencing recapitulates miR-200b mediated inhibition of sprouting.

a Immunofluorescent imaging and associated quantification of a standard sprouting assay with HUVEC transiently transfected with NC siR, miR-200b, or QKI siRs (n=16 to 27 beads per group). Red = CD31; blue = Hoechst nuclear stain; scale bar = 100 µm

b Quantification of a standard sprouting assay with HUVEC dually transfected with NC siR and NC miR, NC siR and miR-200b, QKI siR #1 and miR-200b, or QKI siR #2 and miR-200b (n = 29 to 43 beads per group).

Statistical significance was measured by unpaired t-tests; p-values are indicated as *p<0.05, **p<0.01, ***p<0.001; error bars represent standard error of the mean.

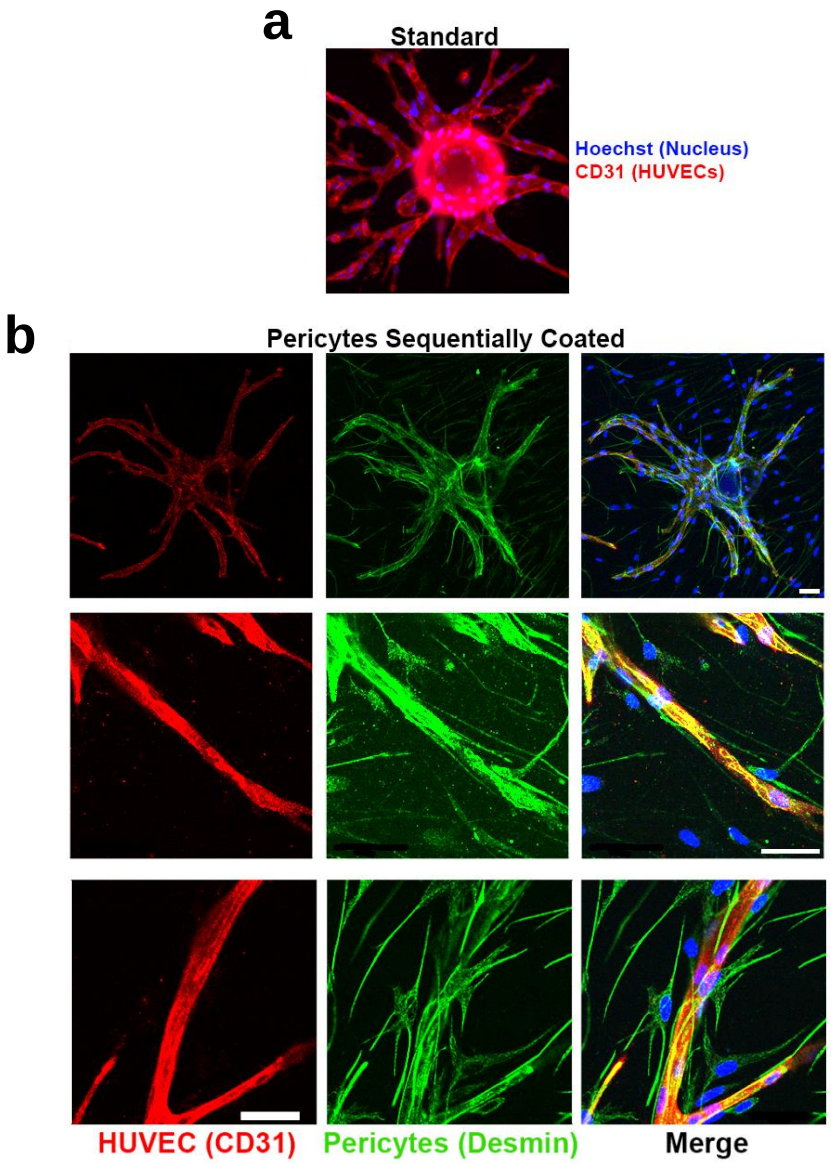

Figure 7 Pericytes tightly associate with endothelial vessels in the bead sprouting assay.

a Standard sprouting assay with HUVEC only coated beads.

b Confocal microscopy images of the pericyte sprouting assay demonstrate that pericytes wrap around endothelial vessels in the sprouting assay, but do not hinder their sprouting. Blue is Hoechst (nuclear stain); red is CD31 (endothelial stain), and green is Desmin (pericyte stain). All scale bars, 50 µm.

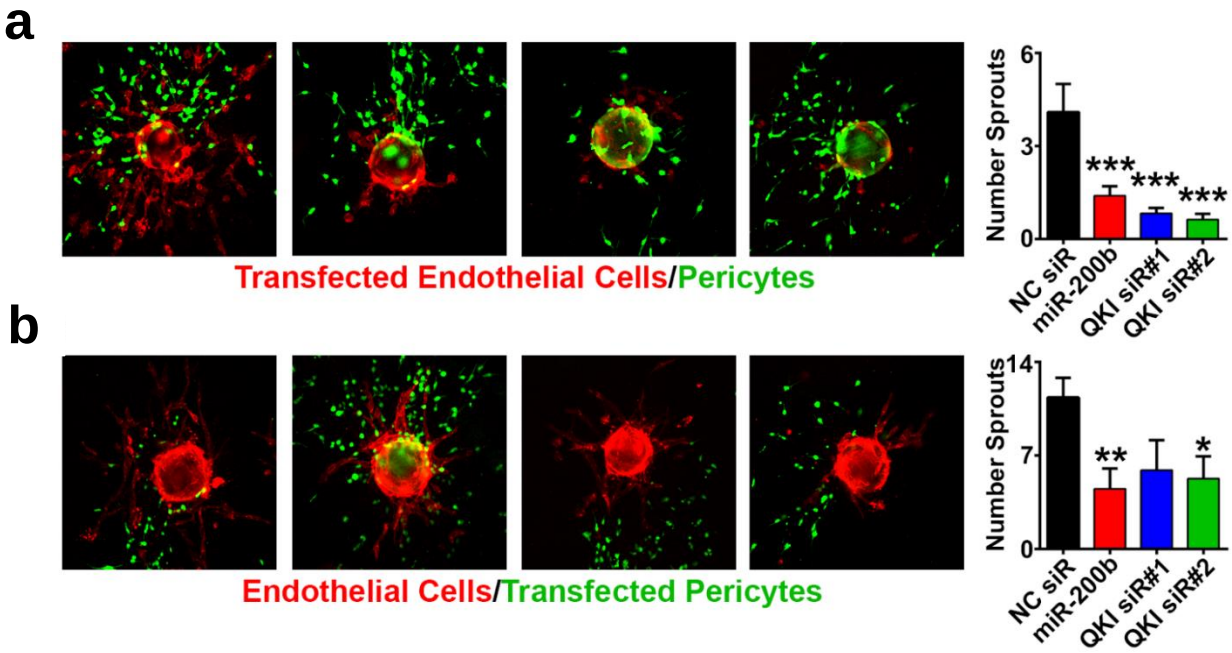

Figure 8 QKI silencing in either ECs or pericytes recapitulates miR-200b mediated inhibition of pericyte-covered vessels.

a Immunofluorescent imaging and associated quantification of pericyte-coated sprouting assay with HUVEC transiently transfected with NC siR, miR-200b, or QKI siRs (n=11 to 43 beads per group)

b Immunofluorescent imaging and associated quantification of pericyte-coated sprouting assay with pericytes transiently transfected with NC siR, miR-200b mimic, or QKI siRs (n=6 to 11 beads per group).

Red = CD31; green = Zsgreen labeled 10T1/2 (pericytes); blue = Hoechst nuclear stain; scale bar = 100 µm; statistical significance was measured by unpaired t-tests; p-values are indicated as *p<0.05, **p<0.01, ***p<0.001; error bars represent standard error of the mean.

QKI Expression in Clinical Samples is Associated with Angiogenesis and Poor Survival

To characterize the clinical relevance of QKI in tumor progression and survival, the Pecot lab assembled a clinically annotated TMA consisting of duplicate core biopsies of LUAD (n=150 patients), LUSC (n=103 patients), and matched normal lung (n=54 patients) cores. To distinguish the relative contributions of QKI in cancer cells and the tumor endothelium, multiplex IHC was used to stain the TMAs for pan-QKI, pan-CK (cancer cell marker), and CD31 (blood vessel marker). Interestingly, although QKI was heterogeneously expressed throughout cancer cells (Figure 9a-c), in several tumor regions I observed high QKI expression at the leading edge near the vasculature (Figure 9a-3), further implicating the role of QKI in promoting a more metastatic and invasive phenotype in cancer cells (Pillman et al., 2018). QKI was also abundantly expressed throughout tumor endothelium (Figs. 9a-2, b, and c). The lung TMAs were then analyzed for relationships between QKI expression and indices of tumor angiogenesis (Figure 10) and clinical outcome. QKI expression in ECs was significantly and positively correlated with numbers of CD31 positive cells (Spearman r=0.247 and two-tailed $p<0.0001$, Figure 11a). In addition, there was a significantly higher percentage of ECs expressing QKI in tumor vasculature compared with normal lung vasculature (Figure 11b). Intriguingly, there was a significant positive correlation between QKI expression in TECs and cancer cells (Spearman r=0.204 and two-tailed $p<0.0001$, Figure 11c), suggesting QKI expression may be regulated between TME compartments in a coordinated manner. Importantly, an assessment of the clinical features of the TMAs revealed that patients with higher densities of QKI-positive TECs or QKI-positive cancer cells had significantly worse overall survival (Figure 11d and e). These results highlight the importance of characterizing the function of QKI specifically in the tumor endothelium, as QKI expression in TECs alone is associated with poor survival. Altogether, these data reveal that QKI is a clinically relevant target expressed during tumor angiogenesis and promotes poor survival. Even more

intriguingly, these findings highlight the importance of assessing the spatial relationship of QKI expression across various compartments of the TME.

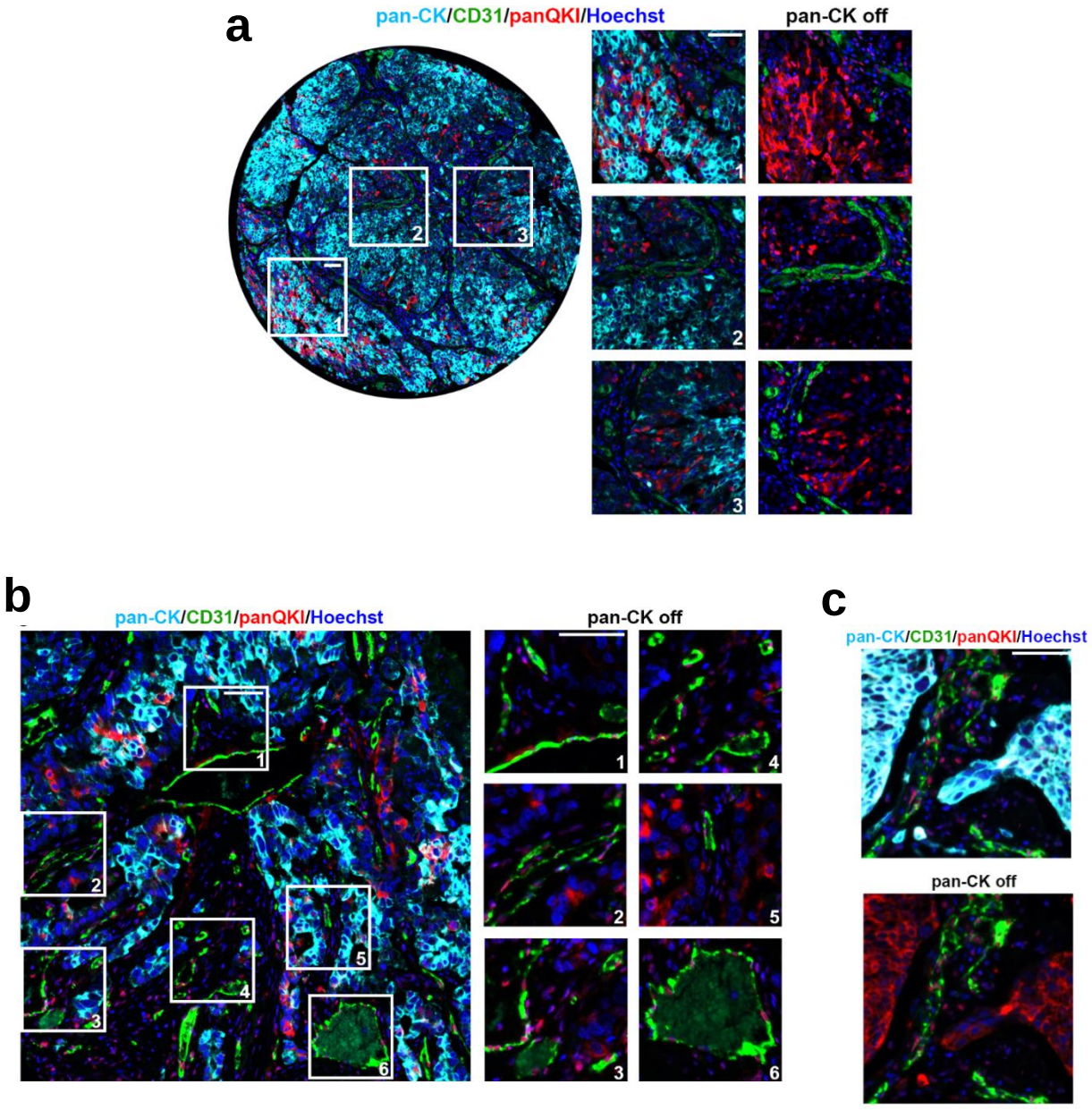

Figure 9 QKI is expressed in multiple cellular compartments of the tumor microenvironment in clinical lung cancer samples.

a Immunofluorescence staining of a clinical lung adenocarcinoma (LUAD) tissue section demonstrating QKI expression in (1) cancer cells, (2) TECs, and (3) at the tumor periphery of invading vessels.

b Immunofluorescence staining in clinical LUAD tissue section demonstrating high endothelial QKI expression in highly vascular tumor tissue.

c Immunofluorescent staining in clinical lung squamous cell carcinoma (LUSC) tissue section demonstrating QKI expression in cancer cells and TECs.

All scale bars 50 µm; cyan = pan-CK, green = CD31, red = pan-QKI isoforms, blue = Hoechst nuclear stain.

Staining was performed by UNC's Translational Pathology Lab

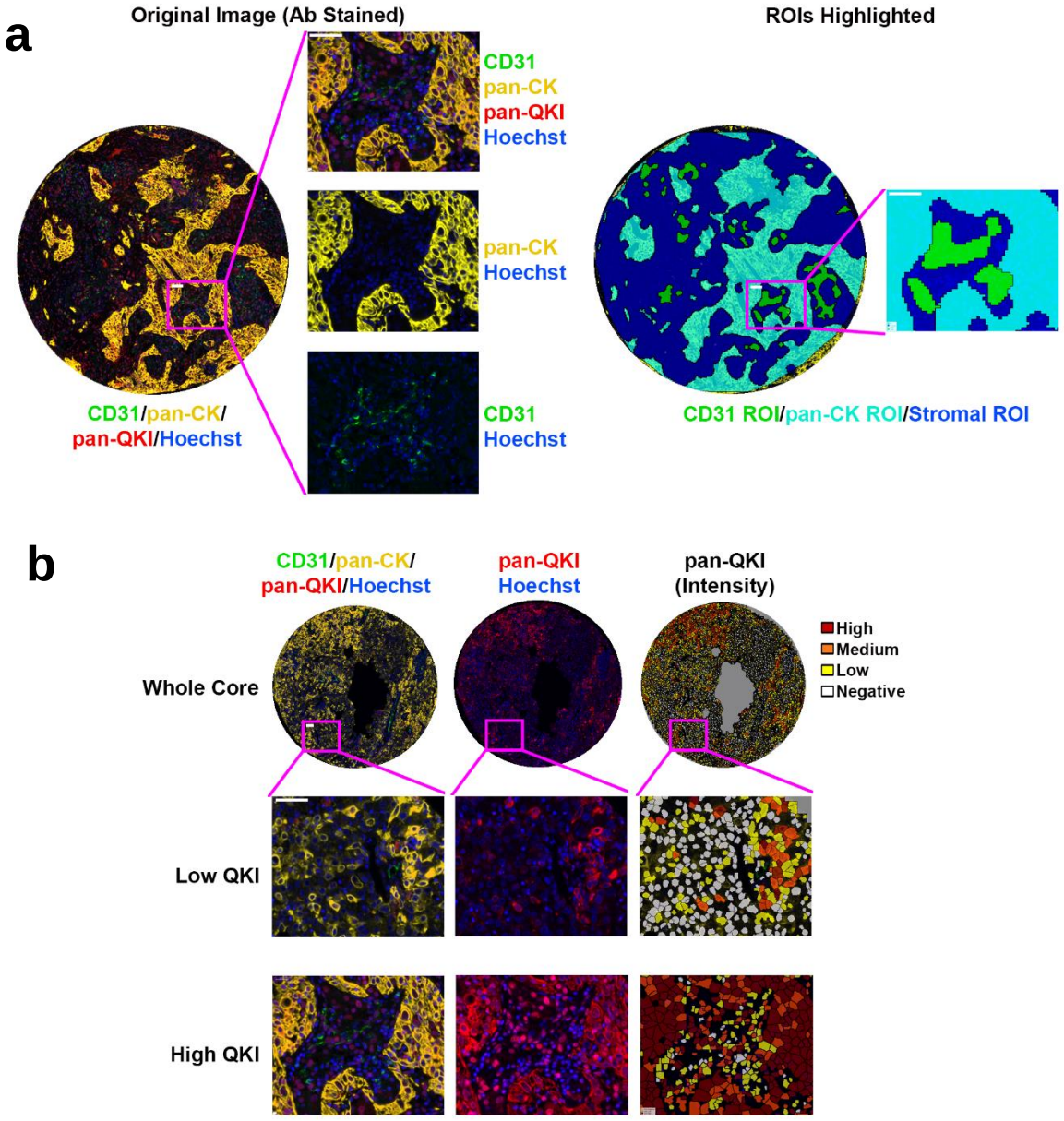

Figure 10 Stained TMA sections can be partitioned into endothelial and cancer cell regions and scored for QKI staining intensity.

a Left: Original multiplex antibody stained TMA core section; green = CD31, yellow = pan-CK, red = pan-QKI isoform, blue = Hoechst nuclear stain. Right: Stained section partitioned into regions of interest (ROI) by Aperio software; green = endothelial ROI; cyan = tumor ROI; blue = stromal ROI.

b Left: Original multiplex antibody-stained TMA core section; green = CD31, yellow = pan-CK, red = pan-QKI isoform, blue = Hoechst nuclear stain. Middle: TMA core section showing only pan-QKI staining. Right: QKI staining intensity analysis.

All scale bars 50 µm.

Analysis was performed by UNC's Translational Pathology Lab

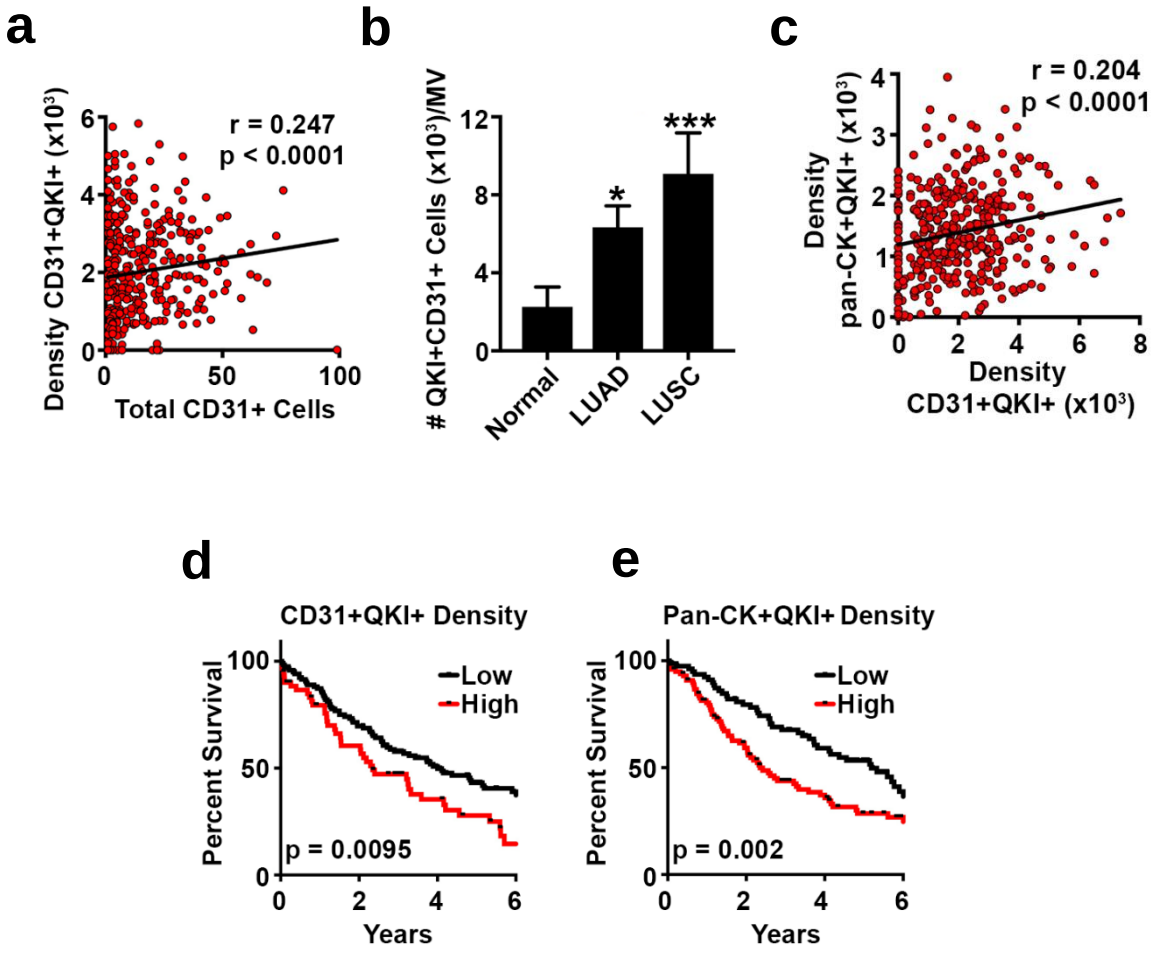

Figure 11 QKI is clinically relevant in tumor angiogenesis and survival.

a Two-tailed Spearman's correlation of the density of pan-QKI low intensity staining ECs per mm^2 of tissue versus the total number of CD31+ cells per tissue section.

b Two-tailed Mann Whitney tests comparing the percent of pan-QKI low intensity staining ECs per mm^2 of endothelial tissue in normal lung, LUAD, and LUSC tissue sections (p-values are indicated as *p<0.05 and ***p<0.001; error bars represent standard error of the mean).

c Two-tailed Spearman's correlation of the density of pan-QKI medium intensity staining pan-CK positive cells per mm^2 of tissue versus the density of pan-QKI low intensity staining ECs per mm^2 of tissue.

d Kaplan-Meier curves for overall survival for high and low density of pan-QKI low intensity staining ECs (n=180 patients).

e Kaplan-Meier curves for overall survival for high and low density of pan-QKI medium intensity staining in pan-CK positive staining cells (n=180 patients).

Analyses were performed by Chad Pecot.

QKI Regulates EC Cell Cycle Progression

To investigate the molecular mechanisms by which QKI regulates EC function, I submitted ECs for RNA-sequencing after transfection with QKI siR for 24 hours. I discovered that pan-QKI isoform knockdown led to both decreases and increases in expression of a large cohort of mRNAs (Figure 12a). Gene Ontology analysis revealed many of the genes downregulated upon QKI silencing play roles in cell cycle regulation (Figure 12a and b). Consistent with these findings, I observed that QKI knockdown induces a potent G1 arrest in ECs synchronized by serum starvation (Figure 13a). Indeed, both miR-200b and QKI siR treatment substantially suppressed EC proliferation (Figure 13b), and miR-200b-mediated inhibition of proliferation was rescued by overexpression of each QKI isoform (Figure 13c). Furthermore, inhibition of endothelial sprouting following miR-200b transfection or QKI knockdown was accompanied by a pronounced and significant decrease in Ki-67 proliferative indices amongst sprouting vessels (Figure 13d). Therefore, QKI-mediated regulation of the EC cell cycle is an important mechanism by which QKI regulates angiogenesis and largely accounts for miR-200b's effects on EC function.

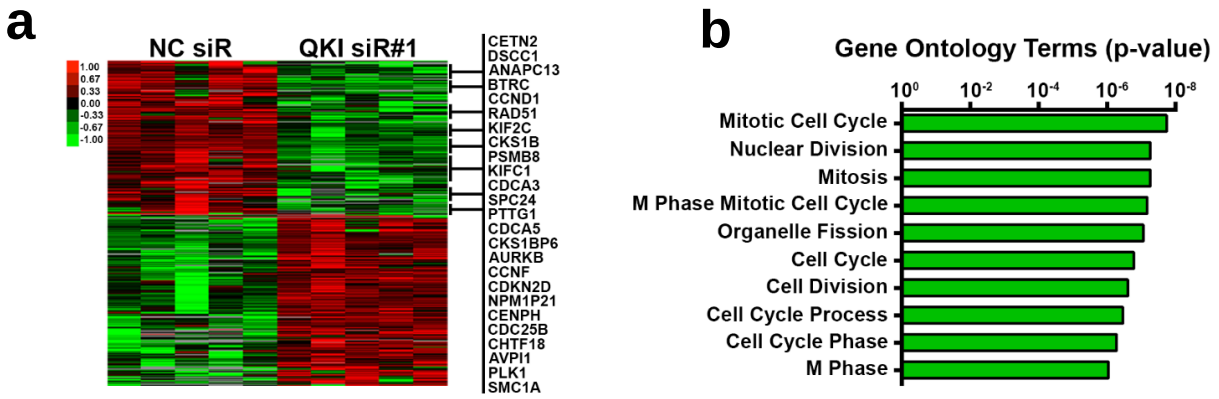

Figure 12 QKI regulates expression of a large cohort of cell cycle-related genes in ECs.

a Heatmap representing the RNA-sequencing analysis performed on HUVEC synchronized by serum starvation with 1% FBS for 24 hours and then transiently transfected with NC siR or QKI siR upon serum starvation release. All genes associated with the Gene Ontology terms presented in **b** are listed to the right.

b Top 10 Gene Ontology terms with corresponding p-values associated with the cohort of genes downregulated in **a** (shown in the upper portion of the heat map).

RNA-Sequencing was performed by UNC's High Throughput Sequencing Core. Heatmap and Gene Ontology Analyses were performed by Alessandro Porrello.

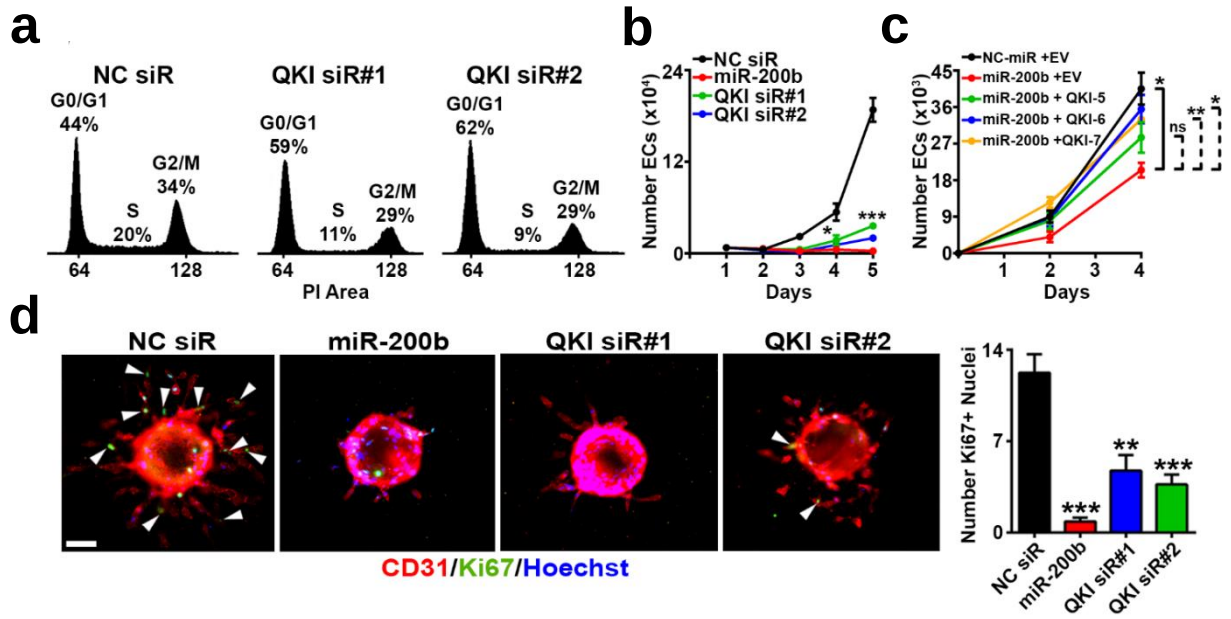

Figure 13 QKI regulates EC cell cycle progression.

a Cell cycle analysis via propidium iodide staining of HUVEC transiently transfected with NC or QKI siRs.

b *In vitro* proliferation assay of HUVEC transiently transfected with NC siR, miR-200b, or QKI siRs.

c *In vitro proliferation* assay of HUVEC serially transfected with NC miR or miR-200b mimic; and empty vector (EV), or QKI-5, QKI-6, or QKI-7 overexpression plasmid.

d Endothelial Ki-67 staining and quantification in standard sprouting assay with HUVEC transiently transfected with NC siR, miR-200b, or QKI siRs; n = 11 to 30 beads per group; red = CD31, green = Ki-67, blue = Hoechst nuclear stain; white arrows demarcate Ki-67 POSITIVE nuclei; scale bar 75 µm).

a and **b** show representative results from at least 2 independent experiments; **b** and **c** were run in triplicate; statistical significance was measured by unpaired t-tests; p-values are indicated as *p<0.05, **p<0.01, ***p<0.001; error bars represent standard error of the mean.

QKI Promotes Cyclin D1 mRNA Stability to Regulate EC Growth

To investigate which candidate mRNA targets are most important for modulating the effects of QKI on EC proliferation and cell cycle progression, the cell cycle-related genes downregulated in the RNA-sequencing dataset were ranked according to fold inhibition relative to control siR-treated cells. This revealed cyclin D1 (CCND1) as the gene most decreased in expression upon QKI silencing (Figure 14a). Using 2 independent siRs to suppress QKI expression, I assessed the top 9 candidates by qPCR in ECs synchronized by serum starvation (Figure 14b). Although it was not significantly altered in expression in the EC RNA-sequencing dataset, I also added p27 to this qPCR panel for comparison, as it has been previously shown to be a QKI cell cycle target during oligodendrocyte differentiation (Larocque et al., 2005). In the panel of genes investigated, CCND1 was the gene most potently and reproducibly downregulated upon QKI knockdown with both siRs, even more so than the previously published QKI target p27 (Figure 14b). CCND1 mRNA expression remained repressed at both 24 and 48 hours post QKI siR transfection (Figure 14c). Consistent with these observations, both miR-200b transfection and direct QKI silencing resulted in inhibition of CCND1 protein expression (Figure 14d). Together, these data support CCND1 mRNA as a novel and important QKI target for its role as a regulator of EC cell cycle progression.

CCND1 mRNA has 4 predicted Quaking Response Elements (QREs) in its 3'UTR based on an *in silico* prediction using RBPMap (Akerman et al., 2009) (Figure 15a, top). To directly assess the interaction between QKI and CCND1 mRNA, I performed an RNA immunoprecipitation using isoform-specific antibodies to pull down each QKI protein isoform and probe for CCND1 mRNA association. Relative to IgG control antibody, I observed dramatic enrichment of CCND1 mRNA with each QKI isoform antibody (Figure 15a, bottom). As a positive control, I also observed enrichment of the previously published QKI mRNA target VE-cadherin (de Bruin et al., 2016b), while I observed no enrichment of negative control GAPDH mRNA (no predicted QKI binding sites) upon QKI pulldown (Figure 15b). QKI has been

shown to bind to the 3'UTR of mRNA targets to regulate their stability (Larocque et al., 2005; Li et al., 2000; Zearfoss et al., 2011). Therefore, to determine whether QKI modulates CCND1 expression by regulating its mRNA stability, I performed a nascent RNA labeling experiment in synchronized ECs (Figure 16a). QKI silencing in ECs resulted in significantly accelerated CCND1 mRNA degradation (Figure 16b) relative to control ECs, whereas the rate of degradation of the predicted non-target 18S rRNA was not similarly affected by QKI silencing (Figure 16c). Although QKI has also been demonstrated to regulate the alternative splicing of mRNA targets (de Bruin et al., 2016a; Wu et al., 2002), the absence of predicted QREs in CCND1 intronic regions (Figure 15a, top), as well as Sashimi plots generated from the RNA-sequencing data set (Figure 17), strongly suggest QKI does not regulate CCND1 alternative splicing. Together, these data demonstrate QKI directly binds to and stabilizes CCND1 mRNA as a mechanism of EC cell cycle progression regulation.

To assess QKI isoform specific contributions to EC proliferation regulation, I used QKI isoform siRs. Silencing of each QKI isoform resulted in inhibition of CCND1 expression in ECs (Figure 18a), however the effects of QKI-6 silencing on CCND1 expression were not as potent. Interestingly, both QKI-5 and QKI-7 silencing, but not QKI-6, recapitulated the effects of pan-QKI isoform silencing on inhibiting EC proliferation (Figure 18b) and sprouting (Figure 18c). These results suggest multiple QKI isoforms are important for CCND1 regulation.

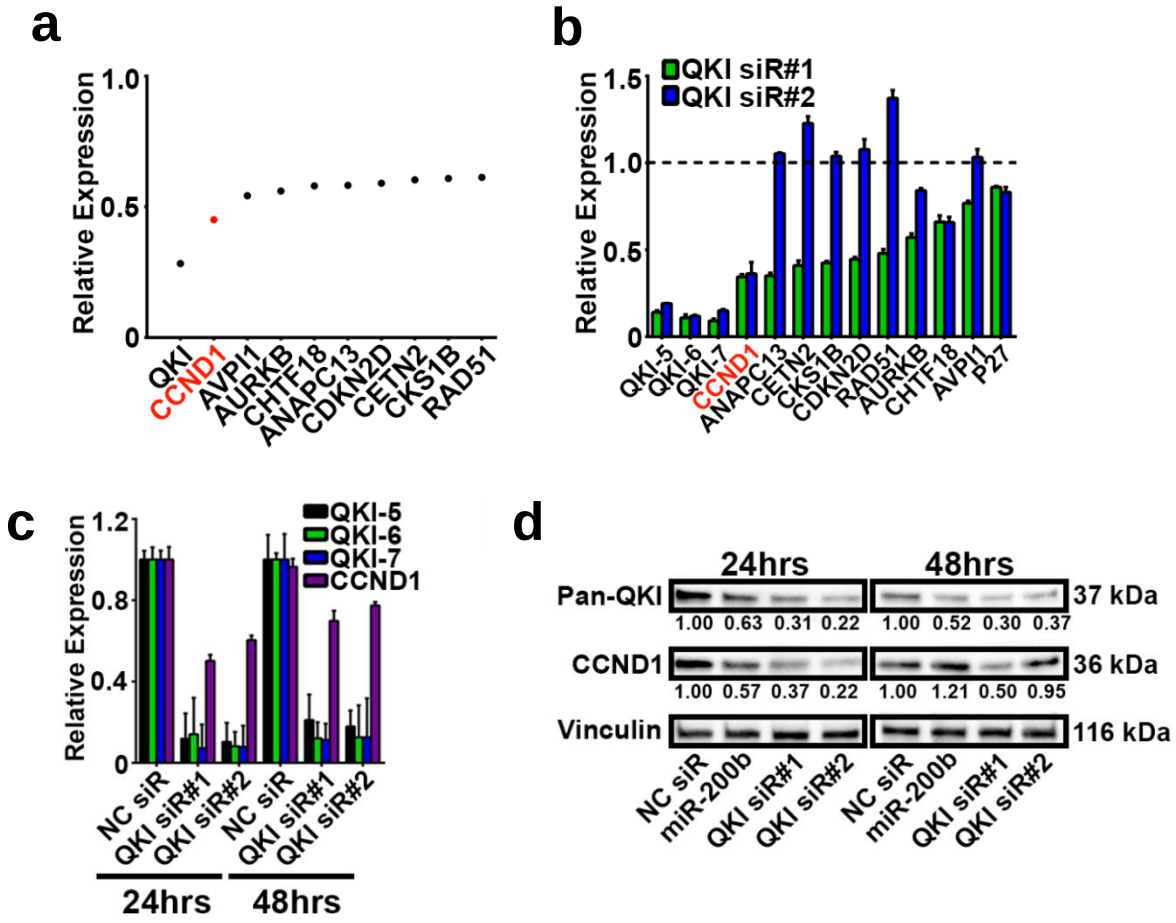

Figure 14 CCND1 is a top cell cycle-related QKI target.

a Relative expression of the 9 protein-coding genes most dramatically downregulated in the RNA-sequencing data set out of all the genes associated with the top 10 Gene Ontology terms (according to their p-value) presented in Figure 12b.

b qPCR validation of genes identified in **a** in HUVEC serum starved for 24 hours in 1% FBS. p27, a previously validated QKI cell cycle target, was included for comparison.

c qPCR analysis for CCND1 mRNA in HUVEC transfected with NC or QKI siRs (representative of at least 2 independent experiments).

d Western blot for QKI and CCND1 protein expression in HUVEC transfected with NC siR, miR-200b, or QKI siRs. Relative densitometric quantifications (normalized to Vinculin) are presented below the bands (representative of at least 2 independent experiments).

All qPCR assays were performed in triplicate; statistical significance was measured by unpaired t-tests; p-values are indicated as *p<0.05, **p<0.01, ***p<0.001; error bars represent standard error of the mean.

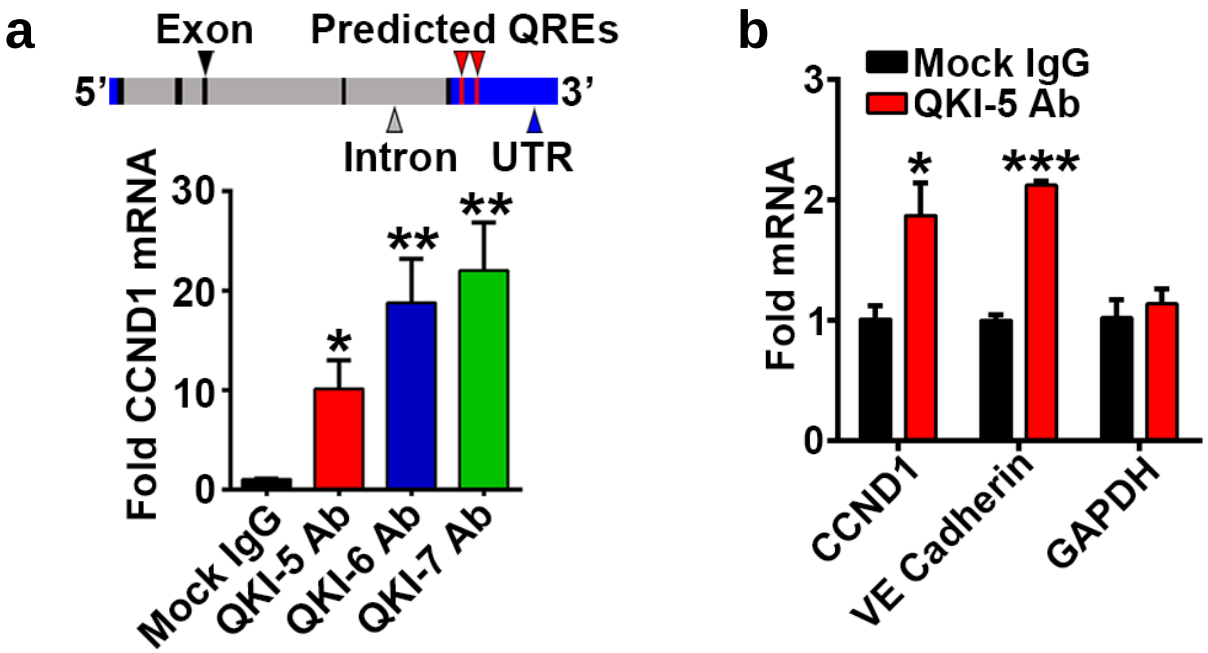

Figure 15 QKI directly regulates CCND1 mRNA.

a Top: CCND1 mRNA schematic; QREs were predicted using RBPmap. Bottom: RNA immunoprecipitation in 2 hours post serum starvation-released HUVEC using mock IgG control or QKI isoform-specific antibody. qPCR was run using CCND1 3'UTR-specific primers (representative of 2 independent experiments).

b RNA immunoprecipitation in HUVEC arrested in serum starvation for 24 hours using mock IgG control or QKI -5 antibody. qPCR for CCND1 was run using CCND1 3'UTR-specific primers.

All qPCR assays were run in triplicate. Statistical significance was measured by unpaired t-tests; p-values are indicated as *p<0.05, **p<0.01, ***p<0.001; error bars represent standard error of the mean.

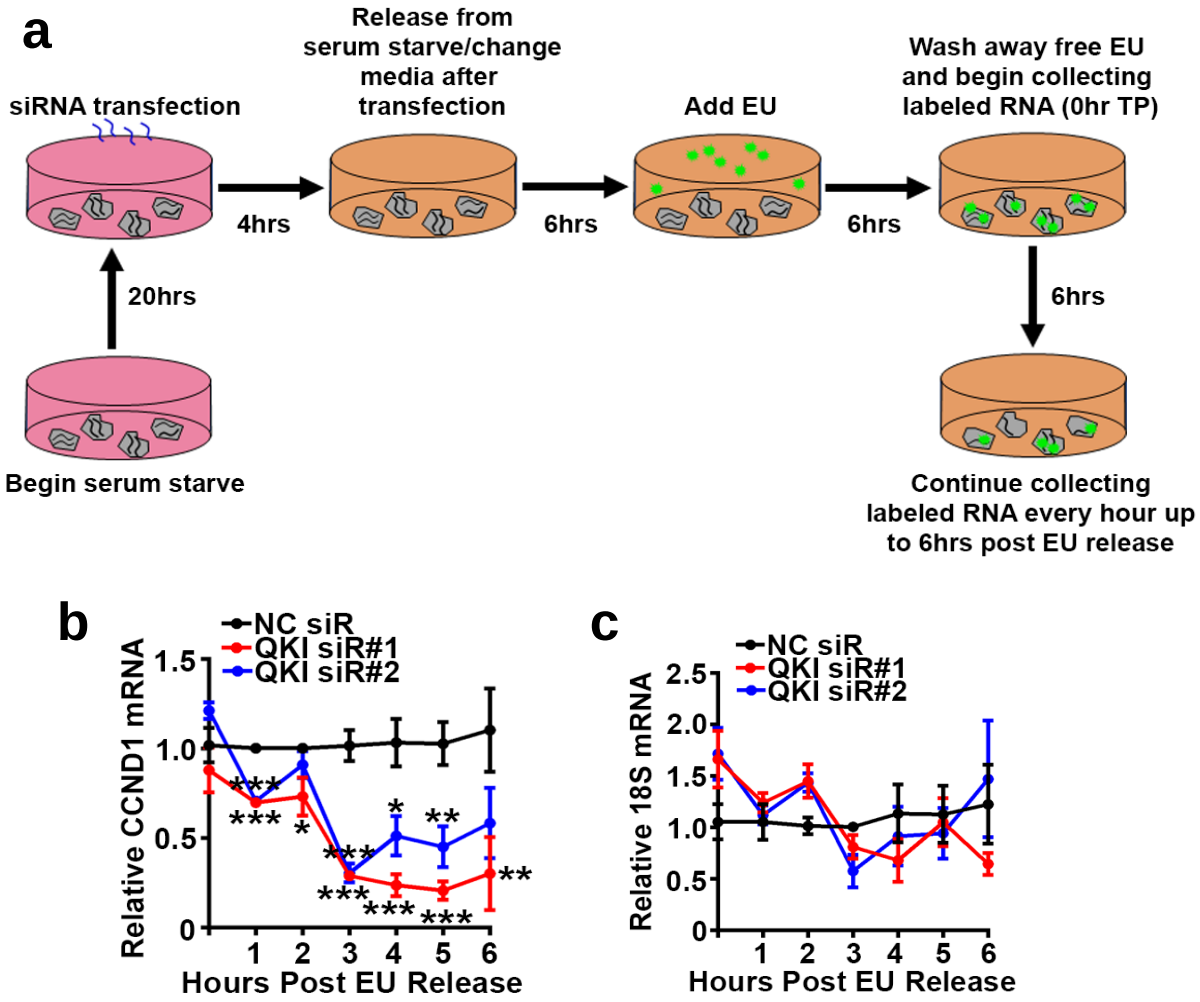

Figure 16 QKI regulates CCND1 mRNA stability.

a Schematic for nascent RNA-labeling experiment.

b qPCR analysis of remaining ethylene uridine ribonucleotide homolog (EU)-labeled CCND1 mRNA in HUVEC transfected with NC or QKI siRs; normalized to the NC siR group at each timepoint (aggregate results from 2 independent experiments).

c qPCR analysis of remaining EU-labeled 18S rRNA in HUVEC transfected with NC or QKI siRs; normalized to the NC siR group at each timepoint (aggregate results from 2 independent experiments).

All qPCR assays were run in triplicate. Statistical significance was measured by unpaired t-tests; p-values are indicated as *p<0.05, **p<0.01, ***p<0.001; error bars represent standard error of the mean.

Figure 17 CCND1 splicing in ECs is not altered upon QKI knockdown.

Sashimi plot of RNA-sequencing data assessing CCND1 alternative splicing. Heights of bars represent the read coverage on exonic bases. Numbers in brackets are the minimum and maximum coverages in each track (sample). Arcs represent splice junctions, and the number in each arc shows the corresponding read coverage for each splice junction.

Analysis was performed by Xinan Liu.

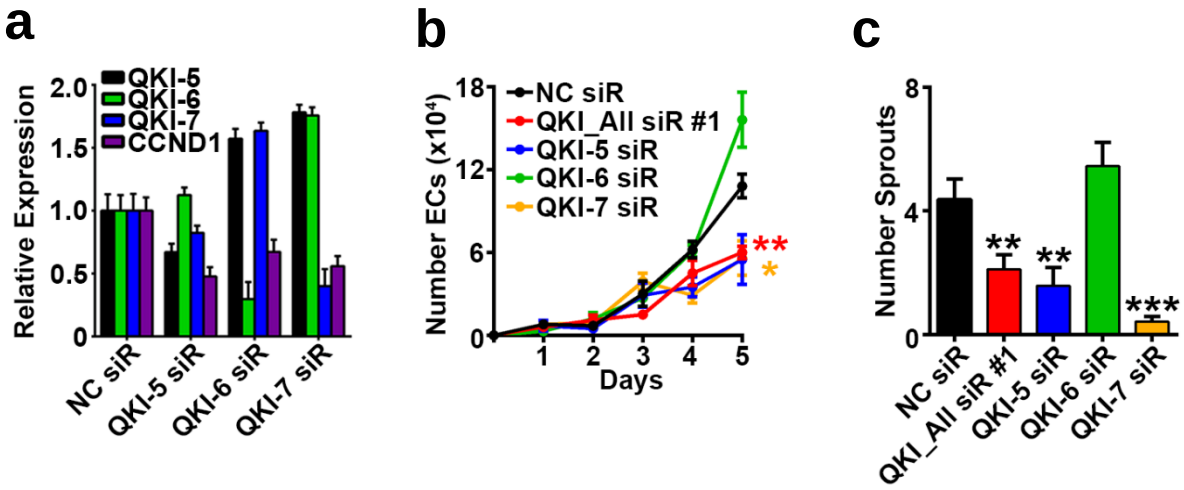

Figure 18 The different QKI isoforms have distinct effects on EC function

a qPCR analysis of QKI and CCND1 expression in HUVEC transfected with isoform-specific QKI siRs (performed in triplicate).

b *In vitro* proliferation assay with HUVEC transfected with NC siR, QKI siR #1, QKI-5 siR, QKI-6 siR, or QKI-7 siR (performed in triplicate).

c Quantification of standard sprouting assay with HUVEC transfected with same groups as **c** (n=26 to 46 beads per group).

Statistical significance was measured by unpaired t-tests; p-values are indicated as *p<0.05, **p<0.01, ***p<0.001; error bars represent standard error of the mean.

Palbociclib Recapitulates the Effects of QKI Silencing on EC Function

I next hypothesized that CCND1-mediated promotion of cell cycle progression is important for the miR-200b/QKI regulatory axis of EC function and angiogenesis. Importantly, I found that CCND1 overexpression rescued the effects of QKI siR-mediated inhibition of EC proliferation (Figure 19), suggesting QKI regulation of CCND1 largely accounts for QKI's effects on EC growth. To determine the implications for angiogenesis regulation upon direct, pharmacologic inhibition of CCND1 function, I used palbociclib to inhibit the cyclin dependent kinase (CDK)4/6-cyclin D complex (Fry et al., 2004). As with miR-200b over-expression or QKI silencing (Figure 13b), I observed a potent and significant reduction in EC proliferation (Figure 20a). Palbociclib treatment also dramatically decreased the number of sprouting vessels per bead (Figure 20b), as well as the Ki-67 proliferative index of the sprouting ECs (Figure 20c). In addition, palbociclib elicited potent effects on EC sprouting in the context of pericyte coverage (Figure 20d) and disrupted blood flow in an angiogenesis Matrigel plug assay *in vivo* (Figure 20e).

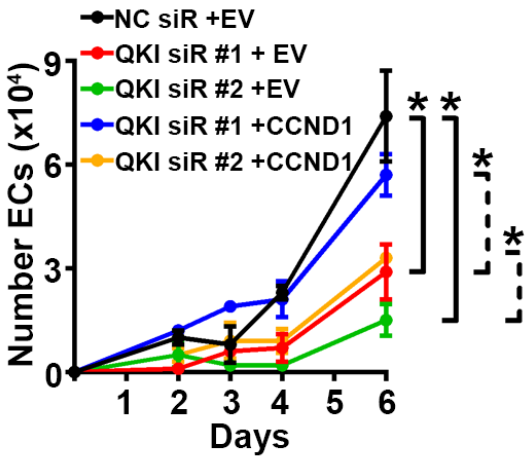

Figure 19 CCND1 overexpression is sufficient to rescue QKI siR-mediated inhibition of EC proliferation

Proliferation assay of HUVEC serially transfected with NC siR or QKI siR; and EV or CCND1 overexpression plasmid (representative of 2 independent experiments an performed in triplicate). Statistical significance was measured by unpaired t-tests; p-values are indicated as *p<0.05; error bars represent standard error of the mean.

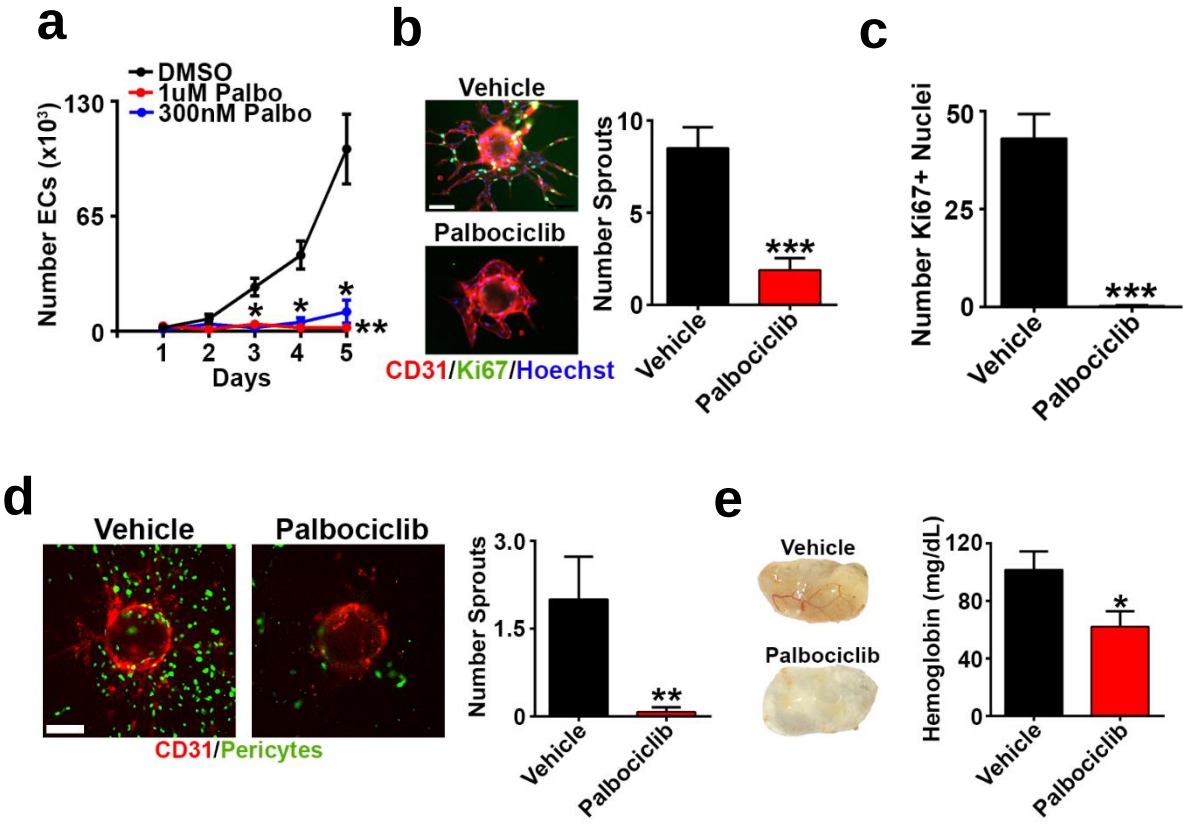

Figure 20 The CDK4/6-cyclin D inhibitor palbociclib inhibits EC function.

a Proliferation assay of HUVEC treated with DMSO, 1uM, or 300 nM palbociclib (representative of at least 2 independent experiments).

b Immunofluorescent staining and quantification of sprouting assay treated with DMSO or 1 µM palbociclib (n=22 to 27 beads per group).

c Quantification of Ki-67 positive nuclei in **g** (n=10 to 14 beads per group).

d Immunofluorescent imaging and quantification of pericyte-coated sprouting assay treated with DMSO or 1 µM palbociclib (n=10 to 13 beads per group).

e Matrigel plugs containing DMSO or 300 nM palbociclib 8 days post subcutaneous implantation and hemoglobin quantification (n=3-4 plugs per group; quantification was performed in triplicate).

Red = CD31; green = Ki-67 in **b** or ZsGreen-labeled 10T1/2 (pericytes) in **d**; blue = Hoechst nuclear stain; scale bars 100 µm. Statistical significance was measured by unpaired t-tests; p-values are indicated as *p<0.05, **p<0.01, ***p<0.001; error bars represent standard error of the mean.

Inhibition of QKI or CCND1 Potently Affects Tumor Angiogenesis and Metastasis

To assess the therapeutic relevance of targeting the miR-200b/QKI/CCND1 regulatory axis on tumor angiogenesis and metastasis *in vivo*, I used the metastatic 344SQ LUAD model (Gibbons et al., 2009; Pecot et al., 2013). First, following orthotopic injection and tumor formation within the left lung, I performed immunofluorescence staining and verified QKI over-expression in TECs compared with LNECs (Figure 21), consistent with the results in clinical LUAD samples (Figure 11b). To target the miR-200b/QKI/CCND1 regulatory axis in the tumor endothelium, I utilized chitosan nanoparticles (CNPs), which has previously been demonstrated to deliver oligonucleotide payloads to TECs (Harrison et al., 2018; Lu et al., 2010; Pecot et al., 2013). I found that in established orthotopic 344SQ tumors, CNPs carrying Cy3-labeled miR payloads predominately localized to TECs and peri-vascular regions (Figure 22).

Next, following orthotopic injection of luciferase-labeled 344SQ cells, mice were randomized into the following groups (n=12 mice/group): 1) NC siR-CNP, 2) miR-200b-CNP, 3) QKI siR#1-CNP, or 4) QKI siR #2-CNP. Four days after 344SQ injection, mice received twice weekly treatments and were euthanized after 4 treatments. Disease burden was assessed, and tumors were collected for staining. There was no evident toxicity from the CNP treatments. Relative to NC siR-CNP treatment, miR-200b-CNP led to modest decreases in metastases (16% reduction in mass and 38% reduction in *ex vivo* bioluminescence [BLI] signal), while direct QKI silencing led to a more robust inhibition of metastasis (QKI siR#1-CNP 40% reduction in mass, $p=0.0247$, Student's t-test and 65% reduction in BLI signal; QKI siR#2-CNP 42% reduction in mass and 64% reduction in BLI signal, $p=0.0405$, Student's t-test, Figure 23a and b). Intriguingly, inhibition of metastasis was associated with statistically significant increases in micro-vessel density (MVD) in tumors scored for CD31 staining, particularly in the QKI siR-CNP-treated groups (52-69% increase in MVD, both $p\leq0.001$, Figure 23c).

Next, I assessed whether palbociclib could recapitulate the effects of QKI siR-CNP *in vivo*. One week following orthotopic injection of luciferase-expressing 344SQ cells, mice were

randomized into the following treatment groups (n=10 mice/group): 1) vehicle or 2) palbociclib. After 1 week of treatment, I assessed disease burden using *ex vivo* BLI. Similar to treatment with QKI siR-CNPs, I observed that direct pharmacologic inhibition of the CCND-CDK4/6 pathway resulted in a 73% reduction in metastatic disease burden (p=0.0086, Student's t-test, Figure 24a). To directly compare the therapeutic effects of QKI siR-CNP delivery and palbociclib treatment, I orthotopically injected 344SQ cells and 5 days later randomized mice into 4 treatment groups: 1) vehicle + NC siR-CNP, 2) palbociclib, 3) QKI siR#1-CNP, or 4) QKI siR#2-CNP. After 10 days of vehicle or palbociclib treatment or 3 doses of CNP, mice were euthanized and assessed for disease burden. Relative to the control group, palbociclib treatment and QKI siR-CNP delivery inhibited the development of distant metastases (Figure 24b). Intriguingly, the inhibitory effects of QKI siR-CNP and palbociclib on metastasis did not correlate with an inhibition of primary orthotopic lung tumor growth (Figure 24c).

To more thoroughly assess the effects of QKI silencing and CCND1-CDK4/6 blockade on TECs in the TME, I subcutaneously injected 344SQ cells, and once tumors reached ~100 mm^3, mice were randomized into 4 treatment groups (n=15 mice/group): 1) vehicle + NC siR-CNP, 2) palbociclib, 3) QKI siR#1-CNP, or 4) QKI siR#2-CNP. Only palbociclib treatment significantly slowed tumor growth, while QKI siR#1-CNP and QKI siR#2-CNP did not have any consistent effects (Figure 25a). These results reflected the direct effects of palbociclib and QKI siR treatments on 344SQ cell proliferation *in vitro* (Figure 25b and c). The lack of an effect of direct QKI silencing on 344SQ growth strongly suggests that the phenotypic effects of QKI siR-CNP-mediated metastasis inhibition *in vivo* are specifically due to effects on the TME and not on cancer cell growth. After 1 week of treatment (6 days of oral gavage, 2 deliveries of CNP), mice were euthanized and tumors were collected for staining (n=5 mice/group). Immunofluorescence analysis of the stained tumors revealed that both the palbociclib and QKI siR-CNP treatment groups displayed pronounced effects on the TME. Intriguingly, relative to the control group, there were significant increases (60-94%, all $p<0.001$) in MVD in the tumors for all treatment

groups (Figure 26a), similar to the results in the orthotopic QKI siR-CNP experiment (Figure 23c). These increases in MVD were associated with consistent, statistically significant decreases (ranging from 32 to 45%) in the percentage of pericyte-covered vessels relative to the control group (Figure 26b) but inconsistent effects on vessel leakiness as determined by FITC-dextran extravasation (Figure 26c).

I hypothesized that the increases in MVD and associated decreases in metastasis induced by QKI siR-CNP and palbociclib treatments may in part be due to decreased tumor hypoxia. To test this, I compared carbonic anhydrous IX (CA9, a marker of hypoxia) staining in subcutaneous tumors treated twice with NC siR-CNP or QKI siR#2-CNP (treatments started when tumors were ~100 mm^3, n=5 mice/group); the latter treatment of which consistently produced the greatest MVD increases compared to all other treatment groups (Figures 23c and 26a). Consistent with decreases in hypoxia leading to less metastatic tumors, I observed a significant reduction in hypoxia upon QKI siR#2-CNP delivery (Figure 26d). In summary, these results demonstrate the importance and therapeutic potential of the miR-200b/QKI/CCND1 axis in regulating tumor angiogenesis and inhibiting metastasis.

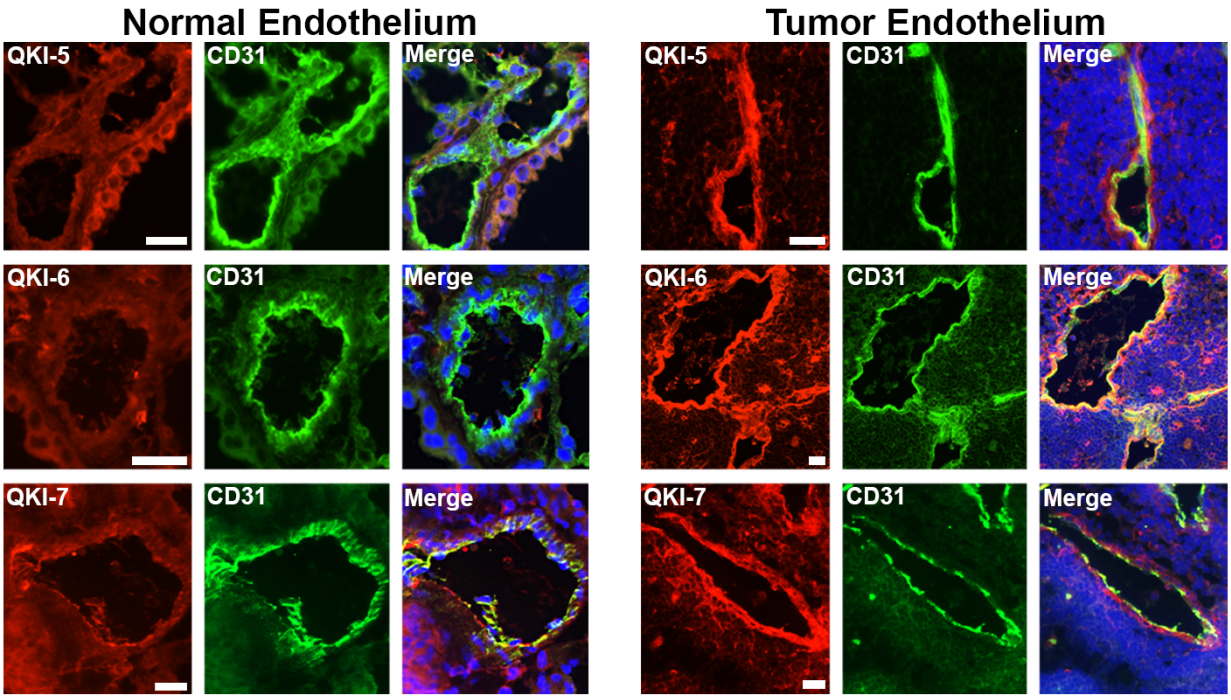

Figure 21 QKI is highly expressed in tumor endothelium in the 344SQ metastatic lung adenocarcinoma mouse model.

Immunofluorescent staining for QKI protein isoform expression in tumor and normal lung endothelium in murine 344SQ orthotopic lung tumor sections; red = QKI isoform, green = CD31, blue = Hoechst nuclear stain; all scale bars 18 µm.

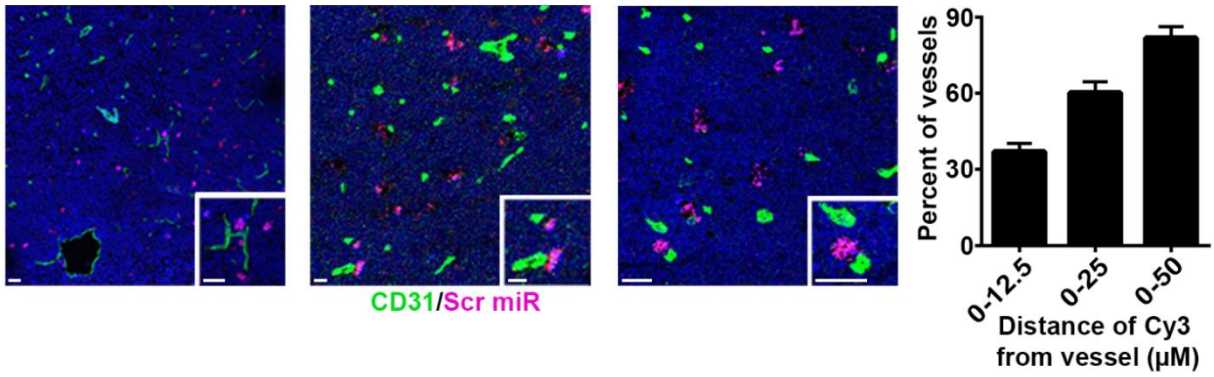

Figure 22 Chitosan nanoparticles can deliver payloads to tumor endothelium.

Immunofluorescent imaging of orthotopic 344SQ lung adenocarcinoma tumor sections from mice intravenously injected with CNPs carrying a scrambled, Cy3-labeled miR. Mice were necropsied 12 days post orthotopic 344SQ injection, with CNP deliveries 48 and 24 hours before sacrifice. Associated quantification of proximity of CNP payload signal to tumor vessels is shown to the right. n=21 images; green = CD31; purple = scrambled miR-CNP; all scale bars 20 μm; error bars represent standard error of the mean.

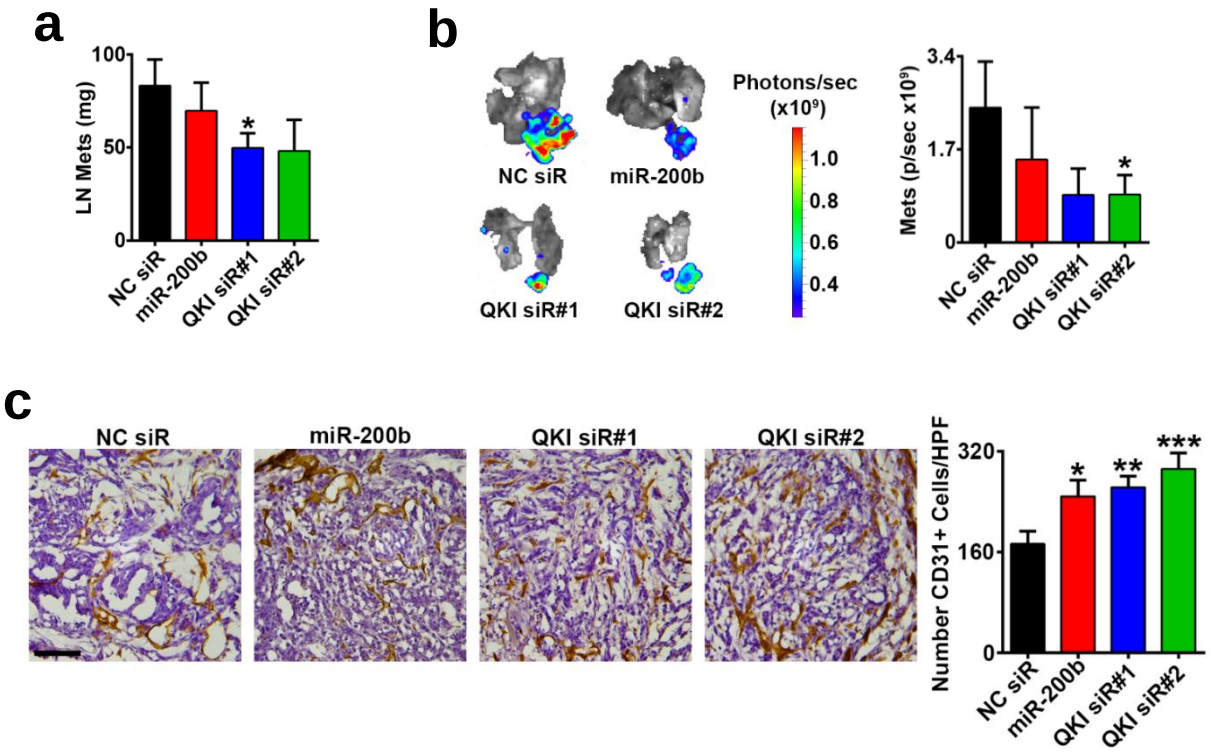

Figure 23 Endothelial QKI and miR-200b targeting alters tumor vasculature and inhibits metastasis.

a – b Mass of 344SQ gross lymph node metastases and *ex vivo* bioluminescent imaging and quantification of luciferase-labeled lymph node metastases from mice treated with NC siR-CNP, miR-200b-CNP, QKI siR#1-CNP, or QKI siR#2-CNP (n=12 mice/group). Mice were necropsied 15 days post 344SQ orthotopic injection, and mice received 4 CNP deliveries.

c Immunohistochemistry 3,3'-diaminobenzidine stain for CD31 in 344SQ lymph node metastases from mice in the treatment groups described in **a – b** (n=4-5 mice per group and 72-94 images per group). Scale bar 100 μm.

Statistical significance was measured by unpaired t-tests; p-values are indicated as *p<0.05, **p<0.01, ***p<0.001; error bars represent standard error of the mean.

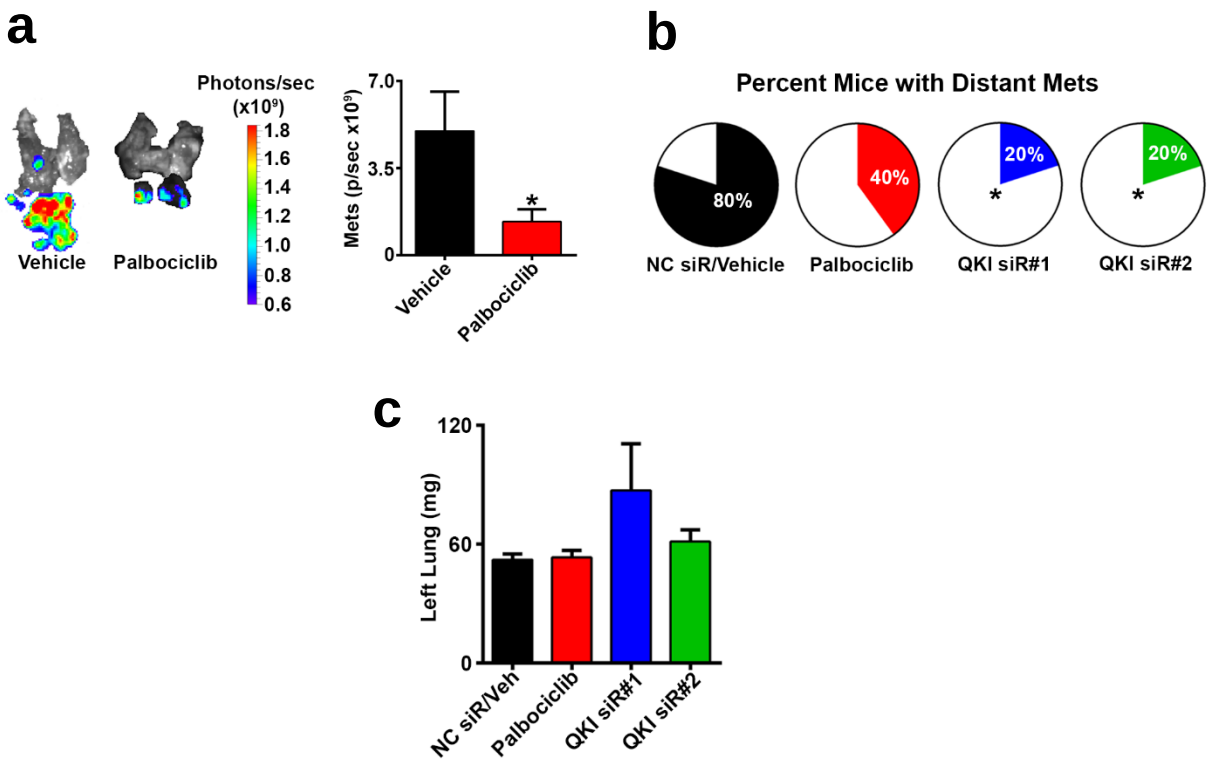

Figure 24 Palbociclib treatment recapitulates the effects of endothelial QKI siR treatment on metastasis.

a *Ex vivo* bioluminescent imaging and quantification of luciferase-labeled lymph node metastases from mice treated with vehicle or palbociclib. Mice were necropsied 15 days post 344SQ orthotopic injection. Mice started daily drug treatments 8 days post 344SQ orthotopic injection (n=10 mice/group). Statistical significance was measured by unpaired t-tests.

b Number of contralateral 344SQ metastases from mice treated with the following groups: vehicle/NC siR-CNP, palbociclib, QKI siR#1-CNP, or QKI siR#2-CNP. Mice were necropsied 15 days post 344SQ orthotopic injection. Mice started daily drug treatments 6 days post orthotopic injections or received 3 CNP deliveries (n=5 mice/group). Statistical significance was measured by Chi-square test.

c Left lung mass from mice orthotopically injected with 344SQ cells and treated with vehicle/NC siR-CNP, palbociclib, QKI siR#1-CNP, or QKI siR#2-CNP (n=5 mice per group). Mice were necropsied 15 days post 344SQ orthotopic injection. Mice started daily drug treatments 6 days post orthotopic injections or received 3 CNP deliveries (n=5 mice/group).

p-values are indicated as *p<0.05; error bars represent standard error of the mean.

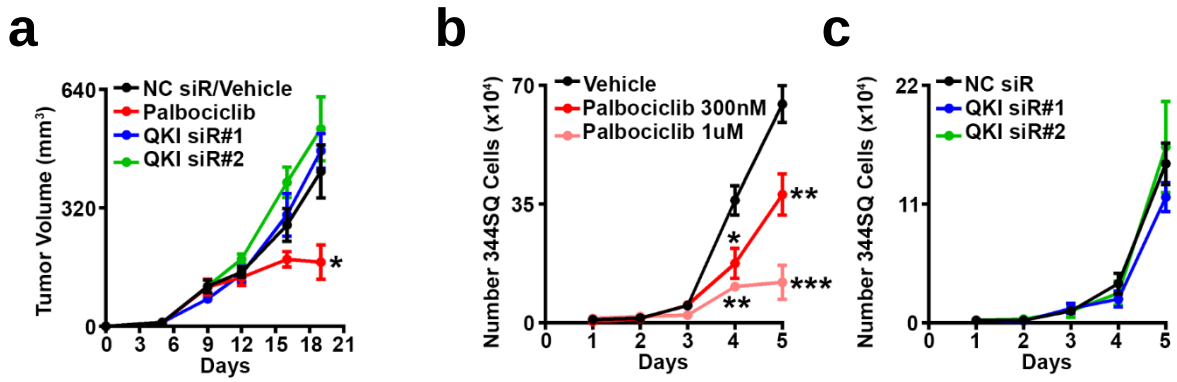

Figure 25 QKI does not regulate primary tumor growth.

a Caliper measurements of 344SQ subcutaneous tumors of mice treated with the following groups: vehicle/NC siR-CNP, palbociclib, QKI siR#1-CNP, or QKI siR#2-CNP. Mice started daily drug treatments 10 days post subcutaenous injections or received 3 CNP deliveries (once every 3 days starting at day 10 for a total of 3 deliveries; n=5 mice/group).

b *In vitro* proliferation assay of 344SQ cells treated with DMSO or palbociclib (representative of 2 independent experiments; run in triplicate).

c *In vitro* proliferation assay of 344SQ cells transfected with NC siR, QKI siR#1, or QKI siR#2 (representative of 2 independent experiments; run in triplicate).

Statistical significance was measured by unpaired t-tests; p-values are indicated as *p<0.05, **p<0.01, ***p<0.001; error bars represent standard error of the mean.

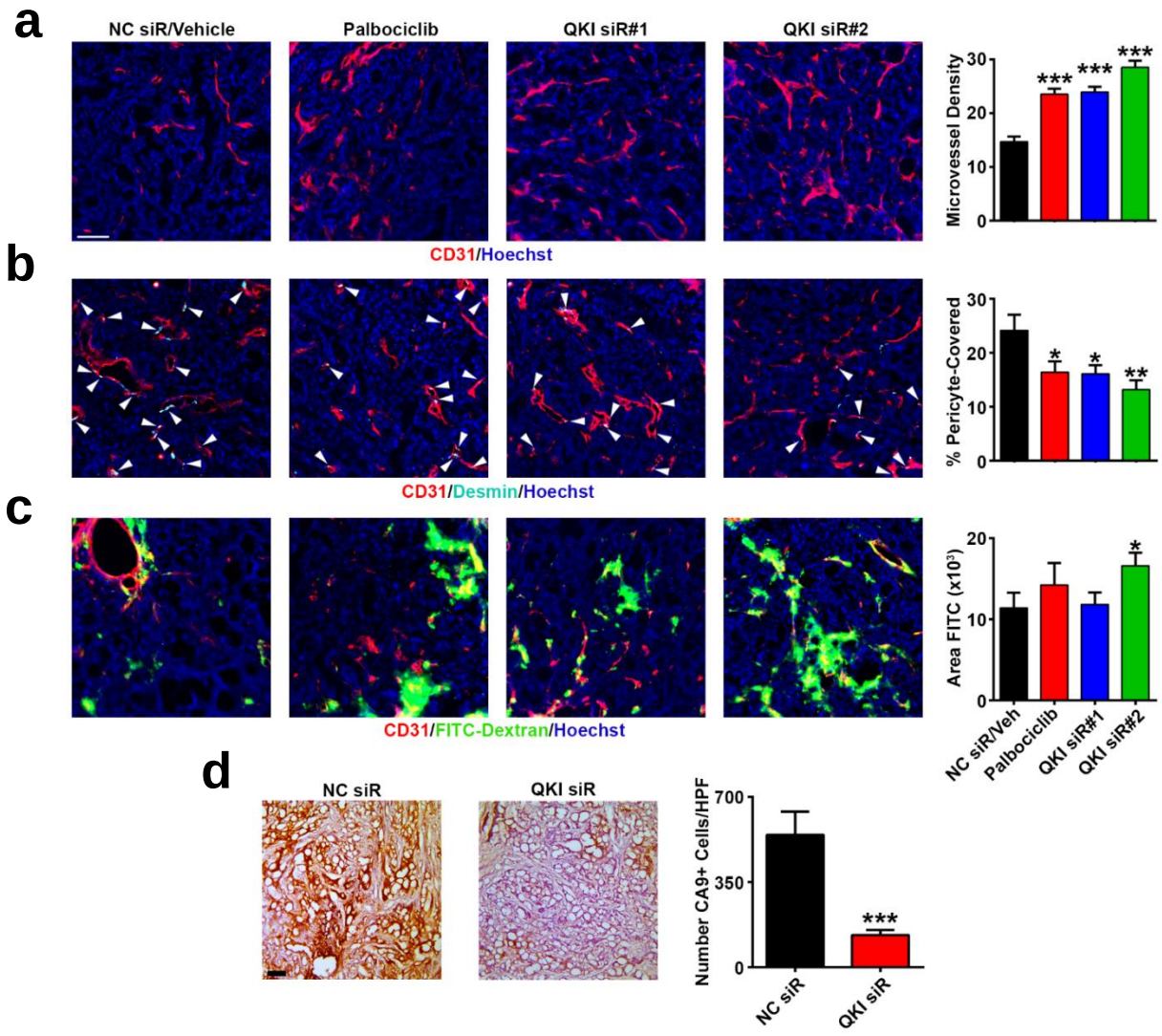

Figure 26 Palbociclib treatment recapitulates the effects of endothelial QKI siR treatment on the tumor microenvironment.

a – **c** Immunofluorescent stained 344SQ subcutaneous tumors from mice treated with the same groups as described in **b** (n=44 to 62 images per group; red = CD31; cyan = desmin; green = FITC-dextran; blue = Hoechst nuclear stain; scale bar 75 µm).

d Immunohistochemistry 3,3'-diaminobenzidine stain for CA9 in 344SQ subcutaneous tumors in mice treated with either NC siR-CNP or QKI siR#2-CNP (n=45 to 46 images per group). Scale bar 100 µm.

Mice were necropsied 16 days post subcutaneous 344SQ injection, after 2 CNP deliveries or 6 days of drug treatment (n=4-5 mice/group). Statistical significance was measured by unpaired t-tests; p-values are indicated as *p<0.05, **p<0.01, ***p<0.001; error bars represent standard error of the mean.

CHAPTER 4: DISCUSSION AND UNANSWERED QUESTIONS[4]

Working Model

I sought to investigate downstream mechanisms in the tumor endothelium responsible for the effects of miR-200b on the TME. I identified QKI as a potent target gene of miR-200b in ECs and found that QKI silencing recapitulated the effects of miR-200b overexpression on endothelial sprouting. I report a novel mechanism whereby QKI promotes CCND1 mRNA stability to facilitate EC proliferation and endothelial function (Figure 27a), and I demonstrate that inhibition of QKI in tumor endothelium *in vivo* alters the tumor vasculature and inhibits metastasis (Figure 27b).

[4] Portions of this chapter were modified and previously appeared as parts of an article in the journal *Oncogene*. The original citation is as follows: Azam, S.H., Porrello, A., Harrison, E.B., Leslie, P.L., Liu, X., Waugh, T.A., Belanger, A., Mangala, L.S., Lopez-Berestein, G., Wilson, H.L., et al. (2019). Quaking orchestrates a post-transcriptional regulatory network of endothelial cell cycle progression critical to angiogenesis and metastasis. Oncogene.
The section “Developing Novel Angiogenesis Models” was slightly modified and previously appeared as part of an article in the *Journal of Visualized Experiments*. The original citation is as follows: Azam, S.H., Smith, M., Somasundaram, V., and Pecot, C.V. (2018). Incorporating Pericytes into an Endothelial Cell Bead Sprouting Assay. J Vis Exp.

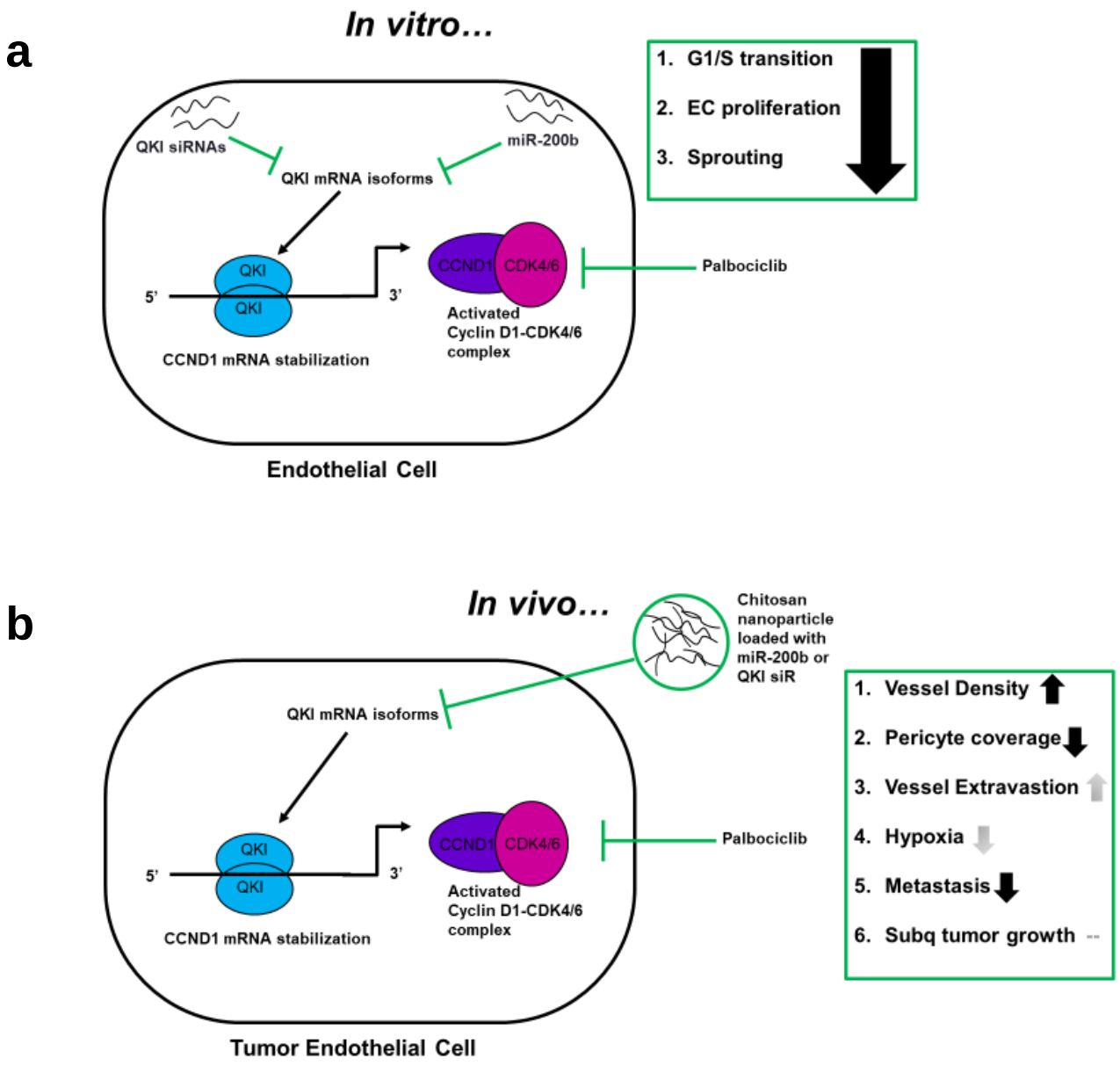

Figure 27 Working models of the miR-200b/QKI/CCND1 axis of regulation of EC function and angiogenesis.

a *in vitro* model of QKI function (i.e., summary of experiments performed in HUVEC).

b *in vivo* model of QKI function (i.e., summary of experiments performed in 344SQ orthotopic LUAD model).

Beyond the miR-200b/QKI Axis

Apart from QKI, miR-200b likely also regulates a complex network of angiogenesis-related genes and pathways. For example, known miR-200b targets associated with EMT, such as ZEB2, have also been implicated in promoting the endothelial to mesenchymal transition (EndoMT). EndoMT has been speculated to contribute to angiogenesis as sprouting ECs (particularly the tip cells leading the vessel) need to undergo many of the same changes as epithelial cells undergoing EMT to be able to promote angiogenesis and expand the vascular network. Such changes include increased migratory phenotype, loss of basal/apical polarity, and increased ability to degrade the surrounding basement membrane and extracellular matrix (Welch-Reardon et al., 2015). Therefore, miR-200b may also inhibit angiogenesis through suppression of ZEB2 and EndoMT. Future studies expanding our understanding of the miR-200b mediated network of endothelial function will lend further insight into such pathways.

Apart from further characterizing additional targets downstream of miR-200b, the contextual cues regulating miR-200b in endothelium upstream are even more poorly understood. What mechanisms are responsible for downregulating miR-200b in tumor ECs, or, conversely, what factors are responsible for sustaining higher miR-200b expression in quiescent endothelium? Hypoxia within tumors has been shown to inhibit miR biogenesis in cancer cells by suppressing expression of miR processing factors dicer and drosha (Rupaimoole et al., 2014; van den Beucken et al., 2014). I observed in the autochthonous mouse model of LUAD that miR-200b was downregulated only in late stage tumors, and not healthy lungs or early stage tumors (Figure 2), suggesting that as the tumor became more aggressive (and, potentially, more hypoxic), miR-200b was downregulated, ultimately de-repressing QKI to allow for increased tumor angiogenesis. One potential mechanism is that hypoxia induces methylation to inhibit expression either of miR-200b and/or miR biogenesis factors. In HUVECs, I observed that treatment with a demethylating agent increased expression of dicer, drosha, and miR-200b; as well as decreased expression of the QKI isoforms, presumably due to activated miR-200b-

mediated inhibition (Figure 28). Therefore, HUVECs may have the capability to be an actively angiogenic EC in part due to suppression of miR-200b (and potentially other anti-angiogenic miRs) via promoter methylation-mediated silencing of dicer and drosha. However, further studies are needed to better understand the mechanisms by which miR-200b expression is regulated within the TME at different stages of tumor progression.

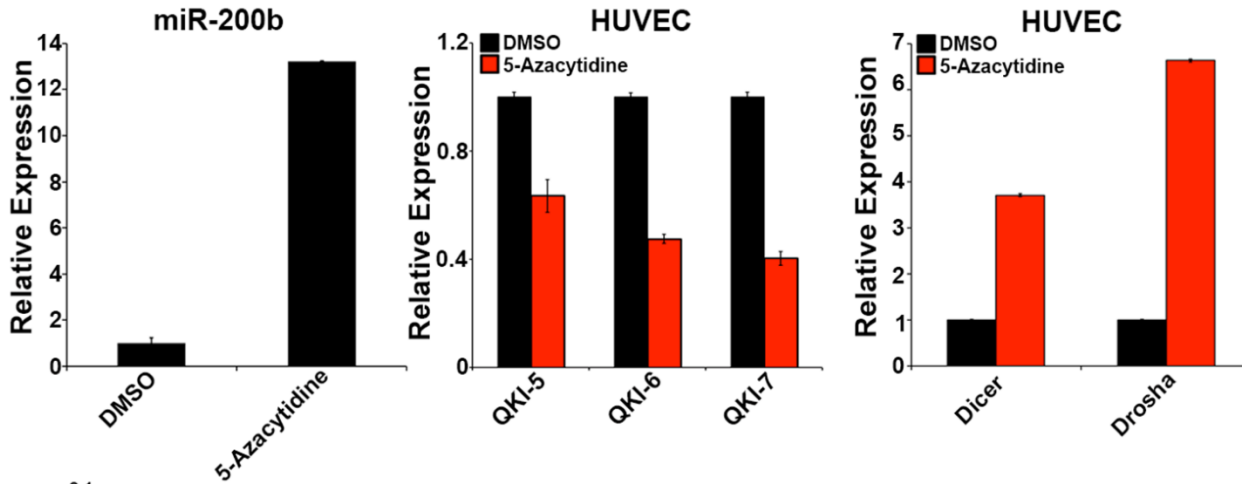

Figure 28 Effects of demethylating agent on miR-200b, QKI, and miR biogenesis enzymes expression.

qPCR for miR-200b, QKI isoforms, dicer, and drosha in HUVEC treated with demethylating agent 5-azacitinde vs. treatment with DMSO vehicle control. All qPCRs were run in triplicate, and error bars represent standard error of the mean.

QKI Isoform-Specific Effects

In my dissertation work, I focused on the role of QKI in promoting angiogenesis downstream of miR-200b. QKI has been demonstrated to play numerous roles in RNA metabolism and has been most thoroughly characterized for its roles in promoting oligodendrocyte differentiation during myelination (Larocque et al., 2005; Li et al., 2000; Wu et al., 2002). I characterized a novel role of QKI in regulating the TME by driving EC cell cycle progression in angiogenesis through the promotion of CCND1 mRNA stability. Notably, all 3 major QKI isoforms immunoprecipitated with CCND1 mRNA, and silencing of each isoform led to loss of CCND1 expression. In addition, overexpression of each isoform rescued the effects of miR-200b-mediated inhibition of EC proliferation. However, isoform-specific silencing demonstrated that only QKI-5 and QKI-7 silencing recapitulated pan-QKI siR inhibitory effects on EC proliferation and sprouting, while QKI-6 silencing did not. Interestingly, however, QKI-5 silencing also resulted in inhibition of QKI-6 and QKI-7 expression, suggesting QKI-5 regulates expression of the other isoforms, which has also been shown in other cell types (Bohnsack et al., 2006; Fagg et al., 2017). Therefore, it may be reasonable to speculate from these results that the predominately cytoplasmic isoform QKI-7 is most important for EC proliferation and angiogenesis. This aligns well with the proposed mechanism of regulating CCND1 through promoting its mRNA stability, which occurs in the cytoplasm. The effects of QKI-5 loss or overexpression on EC function may be explained as primarily through its role as a regulator of QKI-7 expression. Finally, although QKI-6 loss did not affect angiogenesis, QKI-6 overexpression was able to rescue EC proliferation in the presence of miR-200b. One possibility is that in the absence of QKI-7, QKI-6 compensates for QKI-7 function as another QKI cytoplasmic isoform.

More detailed studies discerning the relative contributions of the different QKI isoforms to endothelial function and tumor angiogenesis are needed. For example, a repeat of the RNA-sequencing experiment in HUVEC using isoform-specific QKI siRs instead of the pan-QKI siR

would lend greater insight into isoform-specific targets. Due to the conflicting phenotypes of QKI-6 specific loss relative to QKI-5 and QKI-7 loss, it is possible, for example, that QKI-6 siR will elicit change in expression of an alternate set of genes implicated in another component of EC function independent of proliferation. One caveat to bear in mind, however, when performing experiments with the isoform-specific siRs, is that the QKI-5 siR causes loss in expression of all isoforms. Therefore, to determine QKI-5 specific effects, HUVEC would need to be simultaneously transfected with QKI-5 siR as well as QKI-6 and QKI-7 overexpressing plasmids to compensate for loss of QKI-6 and QKI-7 – which may be technically challenging to perform. Repeating therapeutic experiments assessing the effects CNP-mediated delivery of QKI isoform siRs, as well as staining for the individual QKI isoforms in lung cancer patient TMA and assessing correlations with angiogenesis indices and survival would all add compelling evidence to better characterize the relevance of the QKI isoforms in driving cancer progression and tumor angiogenesis. Finally, performing immunostaining for the different QKI isoforms during sprouting in the bead sprouting assay, or in the endothelium of tumor sections at different stages of tumor growth may lend further insight to the importance of the different isoforms at different stages of vascular development. One sample stain of the QKI isoforms in a late stage sprouting assay is demonstrated in Figure 29. Interestingly, QKI-6 expression appears to be significantly lower than QKI-5 and QKI-7, further supporting QKI-6 may not be as critical to promoting EC function. Although QKI-5 and QKI-7 expression appear to be evenly distributed along the length of the sprouts, it would be interesting to see if the localization of the isoforms changes at earlier stages of sprouting and/or if certain isoforms are more prevalent in tip versus stalk cells, etc.

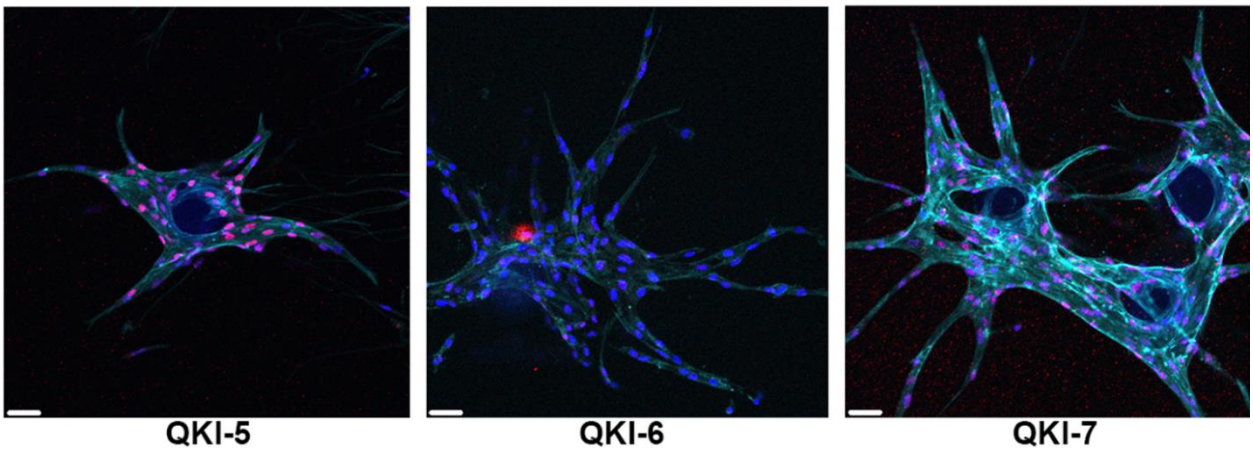

Figure 29 QKI isoform specific staining in bead sprouting assay.

Isoform-specific staining for QKI in late stage bead sprouting assay. Blue, Hoechst nuclear stain; red, QKI; cyan, phalloidin actin stain. Scale bar 50 µm.

Broadening Understanding of QKI Molecular Mechanisms

QKI-mediated promotion of angiogenesis is likely much more complex and extensive than only through regulation of CCND1. Remaining unanswered questions to address include: what other targets are modulated by QKI to promote EC cell cycle progression, and what other mechanisms of QKI are important for regulating ECs and other cell types in the TME? Intriguingly, I observed that QKI expression itself is dependent on EC cell cycle progression (Figure 30) and that the physical interaction between QKI protein and CCND1 mRNA is cell cycle-specific. QKI has been shown to be regulated by Src family protein tyrosine kinases (Src-PTKs) and undergoes tyrosine phosphorylation during central nervous system myelination to modulate its ability to interact with MBP mRNA (Zhang et al., 2003). Thus, I speculate that the phosphorylation status of QKI makes this RBP susceptible to external stimuli that regulate its ability to interact with mRNA targets in specific cellular and molecular contexts. In addition, the different QKI isoforms have unusually long 3'UTRs (approximately 8,000 to 14,000 nucleotides), which carry many predicted miR seed sequences (over 250 according to *TargetScan*), suggesting QKI may be largely susceptible to complex networks of miR regulation. In fact, QKI has been ranked 11th of all the genes in the genome for having the highest number of predicted miR binding sites in its 3'UTR (Artzt and Wu, 2010). As an RBP, QKI may play a pivotal role in varying biological contexts, and these roles may be largely contingent upon extrinsic stimuli acting through phosphorylating kinases and miRs. Indeed, it is intriguing that QKI, which is a distinctly highly conserved RBP (Zorn et al., 1997), has evolved these features that make it so highly susceptible to additional regulation. Such characteristics imply that QKI may represent an important regulatory node within the cell that is critical for integrating multiple cues to subsequently modulate mRNA expression appropriately. In this way, QKI can carry out apparently conflicting roles in different cellular contexts. For example, QKI has been demonstrated to exhibit the opposite effects on cell cycle progression in oligodendrocytes (Biedermann et al., 2010) compared to what I have characterized in endothelium. QKI-5 and 6

promote maturation of a miR involved in cell cycle arrest (Wang et al., 2013) and QKI-6 and 7 promote the stability of cyclin-dependent kinase inhibitor $p27^{Kip1}$ mRNA to shift oligodendrocyte precursors from a pro-proliferative to pro-differentiation state (Larocque et al., 2005). A better understanding of the complexity of QKI regulation, its roles in various cell types, and how cellular context modulates QKI function will lend further insight into the ability of QKI to play such diverse roles in cellular and molecular function.

In a landmark study, Conn et. al assessed a panel of well-known RBPs and found QKI to be the only one critical for circRNA biogenesis, and they further demonstrated that insertion of QREs into linear mRNAs was sufficient to induce their circularization (Conn et al., 2015). However, the functional implications of circRNA generation remain poorly understood. circRNAs are an entire class of non-coding RNAs that are abundant and purposely produced by backsplicing events (Hansen et al., 2013; Jeck et al., 2013; Memczak et al., 2013). Proposed putative functions of circRNAs include acting as miR "sponges" that sequester miRs; sequestering or serving as a scaffold for proteins or mRNAs; or inhibiting the translation of linear mRNAs by sequestering them into an untranslatable form (Jeck and Sharpless, 2014). It is intriguing that QKI is considered a critical component of processing machinery for an entire class of non-coding RNAs and suggests that these circRNAs may comprise a critical component of QKI function important for its roles in angiogenesis regulation. Experiments conducted to identify and then characterize circRNAs expressed in tumor compared to normal ECs (or vice versa) may lend further insight. In addition, QKI's role in regulating other classes of noncoding RNAs, including miRs and long noncoding RNAs should also be more thoroughly characterized, and the contribution of such mechanisms to endothelial function and tumor angiogenesis should be explored.

Finally, a large body of literature has now been published on the various molecular functions of QKI and its mRNA targets. However, the specific molecular mechanisms by which QKI regulates its targets remains poorly understood. For example, how specifically does QKI-5

regulate alternate splicing? Does its binding mask intronic branch points from recognition by the splicing machinery? Similarly, by what mechanism does QKI promote mRNA cytoplasmic stability? Does its binding to mRNA protect it from RNA exonuclease activity? One compelling experiment that could begin answering these questions would be to perform a QKI immunoprecipitation and then perform mass spectrometry to identify QKI protein interaction partners and determine whether QKI directly interacts with any canonical components of RNA processing machinery. Indeed, to my knowledge, no functional protein-protein interactions for QKI have been identified.

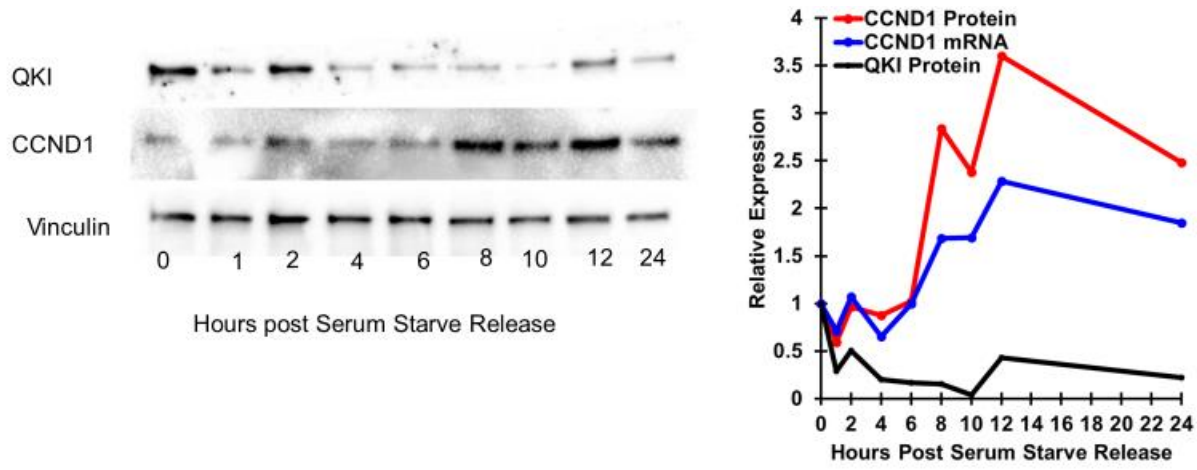

Figure 30 QKI expression is cell cycle regulated.

(Left) Western blot with associated quantification (right) showing QKI and CCND1 protein expression at different time points post serum starve release in HUVEC. The right graph also shows CCND1 mRNA expression from the same cells. HUVEC were serum starved for 24 hours prior to initiating serum starve release.

Deconvoluting the Roles of QKI and miR-200b in Cancer and the TME

QKI has recently been shown to be targeted by miRs specifically in the context of promoting alternative splicing programs during EMT in cancer cells (Pillman et al., 2018). Intriguingly, EMT-induced QKI has also been implicated in generating circRNAs (Conn et al., 2015). In this study, I demonstrate the importance of a novel biological context for miR-200/QKI regulation in ECs. QKI was highly expressed in both cancer cells and TECs in clinical samples of lung cancer, and QKI expression in both TME compartments was independently associated with poor overall survival. These results highlight the clinical relevance of studying QKI-mediated tumor progression and stress the importance of understanding the unique mechanisms of QKI function in different cellular compartments within the TME. My work demonstrates that the role of QKI in promoting cancer progression extends beyond its effects in cancer cells and is also critical in regulating patient survival and metastasis through its functions in the tumor endothelium. To my knowledge, this is the first report of distinguishing QKI's roles within different spatial regions of the TME, which may be key to clarifying the apparent conflicting reports of QKI's roles in cancer progression (Chen et al., 2012; Pillman et al., 2018; Zhou et al., 2017; Zong et al., 2014).

In addition, I also demonstrate the importance of cellular context of miR-200b regulation in cancer. In previous work, it has been demonstrated that miR-200b delivery directly to cancer cells via DOPC liposomal NPs in 344SQ tumors exert paracrine effects on decreasing tumor angiogenesis via inhibition of cancer cell secretion of IL-8 and CXCL1 (Pecot et al., 2013). DOPC liposomes deliver payloads far beyond the tumor vasculature and into cancer cells due to their neutral charge (Landen et al., 2005), whereas the positively-charged CNPs used in this study have been demonstrated to have robust delivery to endothelium (Harrison et al., 2018; Lu et al., 2010). In my dissertation work, I report the effects of delivery of miR-200b directly to ECs within 344SQ lung cancer cell line tumors, as opposed to the cancer cells themselves, further highlighting the importance of cellular context in characterizing the miR-200b/QKI/CCND1 axis

in tumor biology. In addition, in the previous study, the Pecot lab also tested the effects of CNP-mediated delivery of miR-200 directly to ECs within HeyA8 and A2774 ovarian cancer cell line tumors and observed the opposite effects from what I observed in this study (Pecot et al., 2013), also emphasizing the importance of cancer model and cancer type when investigating mechanisms of TME regulation.

Characterizing miR-200b/QKI/CCND1's Effects on Tumor Vasculature

QKI siR delivery to tumor endothelium using CNPs dramatically inhibited distant metastasis. Intriguingly, these therapeutic effects were accompanied by increases in tumor MVD and decreased pericyte coverage. Vessel density within tumors is dynamic and constantly changing in response to the metabolic demands of the tumor (Hlatky et al., 2002; Winkler et al., 2004). MVD has previously been demonstrated to increase in tumors treated with angiogenesis-targeting therapies due to decreases in tumor size (therefore increasing the ratio of pre-existing tumor vessels to tumor area); normalization of tumor vasculature and resultant inhibition of hypoxia; or conversely, conversion to nonfunctional vasculature and a resulting uncoupling of tumor growth from tumor MVD (Goel et al., 2013; Hlatky et al., 2002; Noguera-Troise et al., 2006; Wong et al., 2016; Wong et al., 2015). These results suggest that the reduction in metastases upon CNP-QKI siR delivery to tumor endothelium was due in part to alleviation of tumor hypoxia by increased MVD. Indeed, excessive vessel pruning by anti-VEGF therapies has been shown to promote hypoxia and augment metastasis (Bergers and Hanahan, 2008; Ebos et al., 2009; Paez-Ribes et al., 2009; Vasudev and Reynolds, 2014), while a more balanced alteration of the TME has been suggested to alleviate the activation of aggressive resistance mechanisms (including those stimulated by excessive hypoxia) (Carmeliet and Jain, 2011; Jain, 2014).

Future studies assessing the effects of endothelial QKI silencing on tumor vessel development over time, as well as effects on vessel function, perfusion, and morphology are needed to further characterize the mechanisms by which QKI regulates tumor endothelium *in vivo.* For example, an assessment of vessel perfusion would lend further insight as to whether restored functionality of vasculature upon inhibition of QKI or CCND1 is responsible for the alleviation of hypoxia and subsequent increase in vessel density. Vessel perfusion can be assessed by intravascular injection of fluorescently conjugated lectin, which will result in the labeling of only perfused vessels. Lectin positive staining could be compared to CD31 positive staining to assess what fraction of tumor vasculature is functional after QKI or CCND1 inhibition. Simultaneous injection of mice with hypoxyprobe will allow for a direct comparison between vessel perfusion and tumor hypoxia. I have recently optimized such a multiplex staining scheme (Figure 31) which can be used to begin addressing this question.

An additional possible explanation for the increase in MVD upon QKI/CCND1 targeting is that there was an initial pronounced inhibition of proliferating tumor vasculature, which subsequently stimulated the tumor to activate a compensatory mechanism by co-opting surrounding vasculature from healthy tissue. Because MVD was characterized using CD31 staining, which labels both normal and tumor vasculature, there is no way to distinguish between angiogenic, actively proliferating tumor vasculature and potentially quiescent, co-opted normal vasculature. Re-staining the tumors with markers that have been demonstrated to be more specifically expressed in tumor compared to normal vasculature (Carson-Walter et al., 2001; Ruoslahti, 2004; Seaman et al., 2017; St Croix et al., 2000) and/or, co-staining with CD31 and Ki67 may lend further insight into the nature of the TME after QKI or CCND1 inhibition in endothelium. It is possible that staining with a TEC-specific marker may reveal a pronounced inhibition of angiogenic vessels.

A more thorough assessment of vessel morphology upon QKI/CCND1 suppression may also lend further insight into the mechanism by which this regulatory axis modulates tumor

angiogenesis *in vivo*. For example, vessel tortuosity, vessel thickness, vessel branching, percent of newly formed sprouting vessels (characterized by tip cells extending filopodia), etc. are all parameters that can be more carefully assessed. In addition, due to the inherently dynamic nature of tumor vasculature, utilizing live imaging modalities such as microvasculature ultrasound over the course of tumor progression and response to therapeutic inhibition may lend more insight into the nature of the tumor vasculature. IHC analysis of tumors provides an oversimplified single snapshot in time of an immensely complex and evolving process. It is possible, for example, that imaging of tumor vascular development over time would reveal a pronounced inhibition of MVD at an earlier timepoint in tumor progression.

CNP delivery of QKI siRs also resulted in decreases in pericyte coverage. I observed perivascular QKI expression in the 344SQ orthotopic lung tumors, and QKI expression in pericytes may also have important roles in tumor vasculature. Thus, I cannot exclude the possibility that “off-target” (or non-TEC) CNP delivery of QKI siRs to pericytes resulted in the phenotype of decreased pericyte coverage. Indeed, I observed that QKI silencing in pericytes alone in the bead sprouting assay was sufficient to alter sprouting (Figure 8). However, the *in vivo* decreases in pericyte coverage were not associated with consistent increases in vessel extravasation, suggesting that QKI siR-mediated inhibition of pericyte function may not compromise vessel integrity. It is also interesting to point out that pericytes have been associated with inhibiting EC proliferation to promote vascular stability (Hirschi and D'Amore, 1997). Therefore, inadvertent QKI-silencing mediated inhibition of pericyte function may have led to a derepression of pericyte regulation of EC proliferation and paradoxically contributed to increasing TEC proliferation. All together, these results suggest QKI may directly regulate pericyte function independent of its roles in EC function during angiogenesis and vessel formation. In fact, early papers characterizing the role of QKI in modulating embryologic angiogenesis speculated that it was QKI’s role in promoting smooth muscle cell or pericyte differentiation that was responsible for its effects on angiogenesis, more so than direct effects

on ECs (Li et al., 2003; Noveroske et al., 2002). Therefore, QKI's roles in pericyte function may be even more critical to modulating tumor angiogenesis than its roles in the EC context. The distinct roles of QKI in these 2 vessel-associated cell types remains to be further investigated.

The pleiotropic role(s) of QKI in different cell types may also contribute to cancer progression through other mechanisms. For example, apart from targeting QKI in vascular-associated ECs and pericytes, QKI siR-CNP delivery may have also elicited "off-target" QKI silencing in cancer cells and therefore may have contributed to the inhibition of metastasis through the proposed role of QKI in EMT (Pillman et al., 2018). As supported by the TMA analyses, QKI expression is highly coordinated in at least cancer cells and TECs, and thus targeting QKI may have potent therapeutic effects due to the ability to inhibit multiple components of tumor progression simultaneously. Although QKI has previously been reported to be a tumor suppressor in different cancer types, I observed a lack of an effect on cancer cell proliferation upon QKI silencing in the metastatic model of LUAD, suggesting that the role of QKI in both cancer cells and the TME in metastasis may be more critical for modulating its effects on cancer progression. A better understanding of the complex mechanisms with which QKI regulates EC, pericyte, and cancer cell function and its ability to modulate interactions among these cell types is needed before further therapeutic approaches can be developed.

One approach to begin addressing this question is to develop a mouse model of tissue specific QKI loss. The Pecot lab has begun developing such a mouse: *Cdh5*-Cre^{ERT2}/LSL-ZsGreen/QKI$^{fl/fl}$ that conditionally deletes QKI expression and activates a fluorescent reporter in endothelium under temporal control of tamoxifen. The ability to control QKI loss postnatally is critical for evading potential embryonic lethality as has been previously observed in QKI null and mutant models (Bohnsack et al., 2006; Li et al., 2003; Noveroske et al., 2002). Recently, La Porta et. al demonstrated use of an identical genetic approach to characterize the role of endothelial TIE1 in modulating tumor angiogenesis and its contributions to the different steps of the metastatic cascade (La Porta et al., 2018). The conditional endothelial knockout mouse

model will serve as a powerful tool for more detailed characterization of the role of QKI in tumor angiogenesis and metastasis. Mice can be orthotopically injected in the lung with cancer cells and then treated with tamoxifen to elicit QKI loss in TECs at different timepoints during tumor progression. For example, tamoxifen can be administered before the injection of cancer cells, to determine the effects of endothelial QKI on contributing to the “angiogenic switch” and primary tumor growth. If the kinetics of primary tumor growth and the onset of distant metastasis are well characterized in wild type mice, then tamoxifen can be administered at a known timepoint after the onset of primary tumor growth but before detection of circulating tumor cells within the blood stream to assess the effects of QKI loss on cancer cell intravasation. Finally, tamoxifen could be administered both before and after intravenous injection of cancer cells to assess the effects of QKI endothelial loss on cancer cell extravasation and metastatic outgrowth, respectively.

The benefits of using a conditional knockout mouse model over my prior *in vivo* CNP-mediated RNAi experiments include complete tissue specificity of genetic alterations and higher efficiency of QKI loss. Although CNPs localized to tumor endothelium, the phenotypes observed in my therapeutic experiments likely also resulted from contributing effects of QKI loss in off target cellular compartments such as cancer cells and pericytes. When using the QKI endothelial knockout mouse, the specific contributions of endothelial QKI expression to tumor progression and metastasis can be assessed. In addition, the same experiments could be performed in parallel in wild type mice injected with QKI null cancer cells. In particular, a doxycycline inducible cancer cell line could be used, which would allow for temporal control of cancer cell QKI loss. The same experiments as described above could also be repeated by instead altering the timing of QKI loss in cancer cells instead of the endothelium at different points in tumor progression. These experiments would allow for a direct and defined comparison of the role of QKI expression in endothelium versus cancer cells in tumor growth and metastatic progression and ultimately provide much greater insight into the relative contributions of QKI to cancer progression within different compartments of the TME.

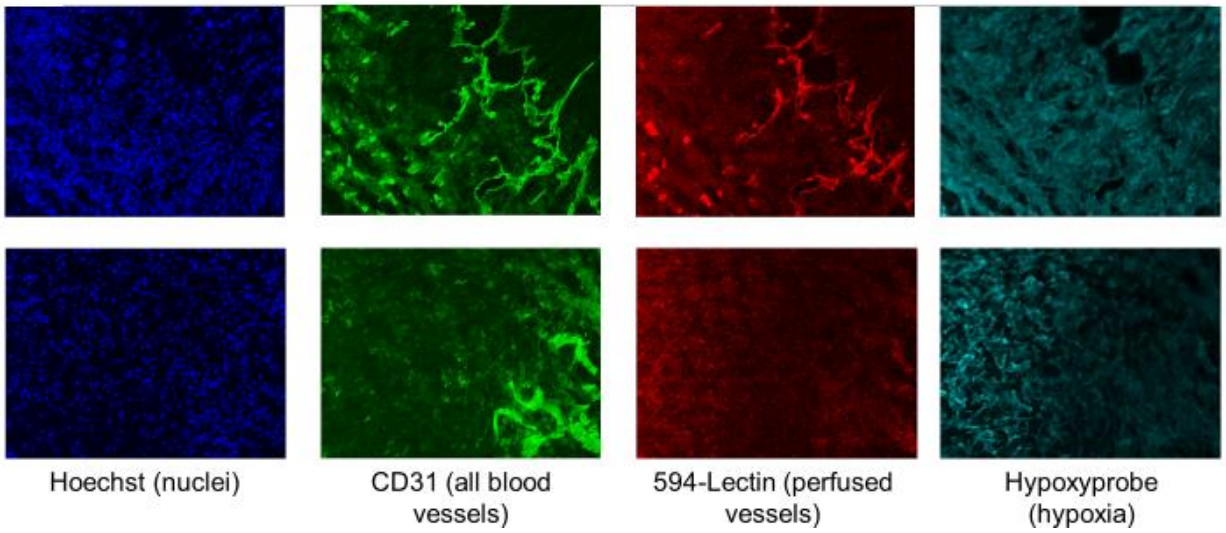

Figure 31 Lectin stains functional vasculature *in vivo.*

Representative staining and imaging of lectin perfused 344SQ LUAD cell line subcutaneous tumor sections. Mice were intravenously injected with DyLight 594 lectin 3 minutes before sacrifice and intraperitoneally with hypoxyprobe 1 hour before sacrifice. Blue, Hoechst nuclear stain; green, CD31 endothelial stain; red, lectin (perfused vasculature), cyan, hypoxyprobe.

New Therapeutic Strategies for Targeting Tumor Angiogenesis

The mechanism I identified by which QKI regulates EC function through CCND1 mRNA stabilization led me to consider the general importance of EC cell cycle in angiogenesis and tumor progression. I observed that direct targeting of the functional CCND1-CDK4/6 complex with palbociclib recapitulated the effects of QKI TEC silencing on angiogenesis and metastasis inhibition. These exciting results suggest that CDK4/6 inhibitors developed for targeting cancer cells (Santo et al., 2015), several of which already have FDA-approval for use in women with hormone-positive breast cancer, can be repurposed for targeting the TME, thus broadening their therapeutic potential and scope. Targeting the cell cycle machinery of ECs provides a more direct pharmacological approach with which to perturb the miR-200b/QKI/CCND1 axis of tumor angiogenesis regulation.

Pharmacological targeting of cell cycle machinery in tumor angiogenesis has been largely unexplored. My work highlights a novel context in which drugs such as palbociclib can be repurposed for tumor angiogenesis targeting. EC proliferation is a hallmark feature of tumor angiogenesis (Hanahan and Folkman, 1996). New blood vessels cannot grow unless ECs proliferate. Therefore, direct targeting of EC proliferation may provide a novel avenue for circumventing the numerous signaling pathways implicated in angiogenesis regulation. Pharmacologic inhibition of VEGF may activate alternate pro-angiogenic signaling pathways, however, if all these pathways feed into the same regulatory node of ultimately promoting EC proliferation, direct inhibition of the EC cell cycle machinery using palbociclib or other cell-cycle targeting drugs may render the activation of other pro-angiogenic signaling pathways ineffective in promoting angiogenesis. Thus, it would be compelling to perform therapeutic experiments in which metastatic mouse models of cancer are dually treated with a VEGF inhibitor and a cyclin D-CDK4/6 inhibitor to determine whether concomitant cell cycle inhibition suppresses the onset of compensatory angiogenesis mechanisms in response to VEGF inhibition. Similarly, it would be intriguing to compare the effects of mono versus dual therapy of delivery of QKI siR CNPs

and a VEGF inhibitor on tumor angiogenesis. In particular, it would be interesting to determine if QKI silencing has an equal or more potent effect on angiogenesis and metastasis compared to VEGF inhibition as well as if dual treatment circumvents the activation of resistance mechanisms or tumor remission often observed with VEGF inhibition.

Developing Novel Angiogenesis Models

Angiogenesis is vital to appropriate embryogenesis and wound healing, and it also plays key roles in numerous diseases including cancer progression (Hanahan and Folkman, 1996) and coronary artery disease.(Semenza, 2003; Zhang and Chopp, 2009). Having a better understanding of how angiogenesis occurs during normal development, and how it is reactivated in pathologic contexts, is critical for the development of novel, effective therapeutics. Faithful *in vitro* models that recapitulate the important stages and cell types involved in angiogenesis *in vivo* are needed to allow researchers to better characterize the molecular mechanisms driving angiogenesis and make novel discoveries in endothelial regulation. Nakatsu and Hughes optimized a sprouting bead assay that they demonstrated undergoes the many known stages of sprouting angiogenesis (Nakatsu et al., 2007; Nakatsu and Hughes, 2008; Nehls and Drenckhahn, 1995). I developed a novel method (presented in Chapter 2: Materials and Methods, subsection Sprouting Assay) which builds upon the assay optimized by Nakatsu and Hughes by incorporating pericytes into the assay, so that the paracrine and juxtracrine roles of mural cells in EC sprouting can be incorporated in novel angiogenesis studies. Pericytes are mural cells that are defined by their role as cells that maintain close physical contact with ECs due to their being embedded in the vascular basement membrane.(Sims, 1986) Pericytes and ECs engage in complex cross-talk via signaling pathways including Notch signaling, ANG-TIE2, PDGFRβ, TGFRβ, and many others.(Armulik et al., 2011; Tattersall et al., 2016) Mouse models deficient in these signaling pathways demonstrate poor pericyte coverage of developing vasculature in embryogenesis, leading to

poor vascular remodeling and dysfunctional vasculature.(Armulik et al., 2011) In addition, the role of pericytes in pathologic angiogenesis is important but oftentimes under-appreciated. For example, a unique feature of tumor vasculature is that the vessels are more immature, leaky, and dysfunctional due to poor pericyte coverage.(Jain, 2005) It has been proposed that the presence or absence of pericytes dramatically impacts the phenotype of tumor blood vessels and is an important mediator of responses to antiangiogenic and antitumor therapies.(Jain, 2005) Thus, including the role of pericytes in *in vitro* assays is key to more completely capture the important mechanisms of endothelial regulation.

Although there are many *in vitro* and *ex vivo* assays currently employed to study angiogenesis, there are shortcomings to consider in each. Some, such as endothelial proliferation and endothelial migration assays, are overly simplified and focus on one endothelial function in an isolated setting on tissue culture plastic (Tahergorabi and Khazaei, 2012). Other assays occur in a more 3 dimensional setting, such as the Matrigel tube formation assay, (Tahergorabi and Khazaei, 2012) but these assays are still oversimplified and focus more on the ability of ECs to migrate and form *de novo* vascular structures, as opposed to sprouting from pre-existing vasculature. Furthermore, none of these assays incorporate mural cell types. There are *ex vivo* models such as the ring aorta assay that do incorporate pericytes present in the host organ, but genetic manipulation of these models is much more challenging due to the necessity of generating knockout or transgenic mouse models of the pathways of interest. The bead sprouting assay is ideal because it models endothelial sprouting, proliferation, migration, and even anastomosis and lumen formation in a 3 dimensional matrix (Nakatsu and Hughes, 2008). The assay faithfully allows for mechanistic assessment of the many different stages of sprouting, while still allowing for direct genetic modification of either the ECs or pericytes in a more controlled setting. The fibrin clots containing the sprouting beads can be easily fixed, stained, and imaged at different stages of sprouting; these sprouts can also be placed in a live imaging chamber to perform real-time imaging of sprouting. My novel sprouting assay protocol

is ideal for studying basic mechanisms of angiogenesis through in depth phenotyping and thorough analysis of the pathways activated during angiogenesis.

The novel sprouting assay protocol presented in Chapter 2: Materials and Methods presents a set of conditions for incorporating pericytes into the standard EC-coated bead sprouting assay which allows for a tight association of ECs and perictyes *in vitro.* In this assay, the presence of the pericytes complements the occurrence of sprouting. The protocol also enables effective silencing (*e.g.* via RNAi) of a gene of interest in a cell type of interest (such as VEGFA specifically in ECs or PDGFRB in pericytes) (Armulik et al., 2011; Coultas et al., 2005) and allows for assessment of relative contributions of gene expression within the distinct cell types to sprouting phenotypes. Researchers employing this protocol are encouraged to perform a standard EC-only sprouting assay in parallel to the pericyte-coated sprouting assay to more thoroughly investigate the unique contributions of pericytes in the vascular functions and phenotypes being studied.

Although this assay begins to address the cellular and phenotypic complexity of angiogenesis at a greater resolution, it still represents an oversimplified system relative to the true, *in vivo* context. In addition, the sprouting angiogenesis occurring in this assay is more analogous to a healthy, physiological context as opposed to a pathologic context such as tumor angiogenesis. Future applications of this method may include the introduction of additional cell types (such as immune cell populations that modulate angiogenic responses) to further recapitulate the heterotypic cellular interactions involved in this complex process. The introduction of external stressors - such as a tumor embedded in proximity to the sprouting vessels in the fibrin gel - to simulate pathologic angiogenesis *in vitro* may also be employed to allow more thorough, mechanistic characterization of the molecular pathways activated in pathological contexts. These advances will be important for improving the ability of researchers to study the complex stages of angiogenesis in a more controlled setting, ultimately enabling discovery and more in-depth characterization of novel therapeutic pathways for targeting

pathologic angiogenesis.

Concluding Remarks

In my dissertation work, I identified QKI as an important target of the miR-200 family with a previously unappreciated role in promoting tumor angiogenesis, metastasis, and poor overall survival. I found that QKI stabilizes CCND1 mRNA during the G1 to S transition, which promotes EC proliferation and sprouting angiogenesis. Using CNP-mediated delivery of QKI siRs to target the tumor endothelium, I observed potent effects on tumor vasculature and inhibition of lung cancer metastasis. Intriguingly, repurposing palbociclib to target the CCND1-CDK4/6 axis in TECs recapitulated these effects.

Altogether, I have discovered a clinically relevant, novel miR/RBP regulatory mechanism of tumor endothelial function that shows promise as a therapeutic target for regulating tumor angiogenesis and inhibiting distant metastasis. Furthermore, I have demonstrated the therapeutic utility of a novel pharmacologic strategy in which tumor angiogenesis and metastasis is suppressed through direct targeting of EC cell cycle progression via palbociclib.

In addition, I have contributed a technical advancement to the angiogenesis field by optimizing the incorporation of pericytes into an improved EC-coated bead sprouting assay. This protocol provides a novel tool for characterizing the complex stages and heterotypic cellular interactions of sprouting angiogenesis and allows users to employ genetic and imaging approaches to conduct thorough mechanistic investigations of vascular function.

REFERENCES

Akerman, M., David-Eden, H., Pinter, R.Y., and Mandel-Gutfreund, Y. (2009). A computational approach for genome-wide mapping of splicing factor binding sites. Genome Biol *10*, R30.

Anand, S., Majeti, B.K., Acevedo, L.M., Murphy, E.A., Mukthavaram, R., Scheppke, L., Huang, M., Shields, D.J., Lindquist, J.N., Lapinski, P.E.*, et al.* (2010). MicroRNA-132-mediated loss of p120RasGAP activates the endothelium to facilitate pathological angiogenesis. Nat Med *16*, 909-914.

Andrae, J., Gallini, R., and Betsholtz, C. (2008). Role of platelet-derived growth factors in physiology and medicine. Genes Dev *22*, 1276-1312.

Armulik, A., Genove, G., and Betsholtz, C. (2011). Pericytes: developmental, physiological, and pathological perspectives, problems, and promises. Dev Cell *21*, 193-215.

Artzt, K., and Wu, J.I. (2010). STAR trek: An introduction to STAR family proteins and review of quaking (QKI). Adv Exp Med Biol *693*, 1-24.

Augustin, H.G., Koh, G.Y., Thurston, G., and Alitalo, K. (2009). Control of vascular morphogenesis and homeostasis through the angiopoietin-Tie system. Nat Rev Mol Cell Biol *10*, 165-177.

Azam, S.H., Porrello, A., Harrison, E.B., Leslie, P.L., Liu, X., Waugh, T.A., Belanger, A., Mangala, L.S., Lopez-Berestein, G., Wilson, H.L., et al. (2019). Quaking orchestrates a post-transcriptional regulatory network of endothelial cell cycle progression critical to angiogenesis and metastasis. Oncogene.

Azam, S.H., Smith, M., Somasundaram, V., and Pecot, C.V. (2018). Incorporating Pericytes into an Endothelial Cell Bead Sprouting Assay. J Vis Exp.

Baluk, P., Hashizume, H., and McDonald, D.M. (2005). Cellular abnormalities of blood vessels as targets in cancer. Curr Opin Genet Dev *15*, 102-111.

Baluk, P., Morikawa, S., Haskell, A., Mancuso, M., and McDonald, D.M. (2003). Abnormalities of basement membrane on blood vessels and endothelial sprouts in tumors. Am J Pathol *163*, 1801-1815.

Bartel, D.P. (2009). MicroRNAs: target recognition and regulatory functions. Cell *136*, 215-233.

Batchelor, T.T., Sorensen, A.G., di Tomaso, E., Zhang, W.T., Duda, D.G., Cohen, K.S., Kozak, K.R., Cahill, D.P., Chen, P.J., Zhu, M.*, et al.* (2007). AZD2171, a pan-VEGF receptor tyrosine kinase inhibitor, normalizes tumor vasculature and alleviates edema in glioblastoma patients. Cancer Cell *11*, 83-95.

Bazzini, A.A., Lee, M.T., and Giraldez, A.J. (2012). Ribosome profiling shows that miR-430 reduces translation before causing mRNA decay in zebrafish. Science *336*, 233-237.

Benedito, R., Roca, C., Sorensen, I., Adams, S., Gossler, A., Fruttiger, M., and Adams, R.H. (2009). The notch ligands Dll4 and Jagged1 have opposing effects on angiogenesis. Cell *137*, 1124-1135.

Benjamin, L.E., Hemo, I., and Keshet, E. (1998). A plasticity window for blood vessel remodelling is defined by pericyte coverage of the preformed endothelial network and is regulated by PDGF-B and VEGF. Development *125*, 1591-1598.

Benjamin, L.E., and Keshet, E. (1997). Conditional switching of vascular endothelial growth factor (VEGF) expression in tumors: induction of endothelial cell shedding and regression of hemangioblastoma-like vessels by VEGF withdrawal. Proc Natl Acad Sci U S A *94*, 8761-8766.

Bergers, G., and Benjamin, L.E. (2003). Tumorigenesis and the angiogenic switch. Nat Rev Cancer *3*, 401-410.

Bergers, G., Brekken, R., McMahon, G., Vu, T.H., Itoh, T., Tamaki, K., Tanzawa, K., Thorpe, P., Itohara, S., Werb, Z.*, et al.* (2000). Matrix metalloproteinase-9 triggers the angiogenic switch during carcinogenesis. Nat Cell Biol *2*, 737-744.

Bergers, G., and Hanahan, D. (2008). Modes of resistance to anti-angiogenic therapy. Nat Rev Cancer *8*, 592-603.

Bergers, G., and Song, S. (2005). The role of pericytes in blood-vessel formation and maintenance. Neuro Oncol *7*, 452-464.

Bergers, G., Song, S., Meyer-Morse, N., Bergsland, E., and Hanahan, D. (2003). Benefits of targeting both pericytes and endothelial cells in the tumor vasculature with kinase inhibitors. J Clin Invest *111*, 1287-1295.

Bethune, J., Artus-Revel, C.G., and Filipowicz, W. (2012). Kinetic analysis reveals successive steps leading to miRNA-mediated silencing in mammalian cells. EMBO Rep *13*, 716-723.

Beuck, C., Qu, S., Fagg, W.S., Ares, M., Jr., and Williamson, J.R. (2012). Structural analysis of the quaking homodimerization interface. J Mol Biol *423*, 766-781.

Biedermann, B., Hotz, H.R., and Ciosk, R. (2010). The Quaking family of RNA-binding proteins: coordinators of the cell cycle and differentiation. Cell Cycle *9*, 1929-1933.

Blanco, R., and Gerhardt, H. (2013). VEGF and Notch in tip and stalk cell selection. Cold Spring Harb Perspect Med *3*, a006569.

Bohnsack, B.L., Lai, L., Northrop, J.L., Justice, M.J., and Hirschi, K.K. (2006). Visceral endoderm function is regulated by quaking and required for vascular development. Genesis *44*, 93-104.

Bohnsack, M.T., Czaplinski, K., and Gorlich, D. (2004). Exportin 5 is a RanGTP-dependent dsRNA-binding protein that mediates nuclear export of pre-miRNAs. Rna *10*, 185-191.

Bottsford-Miller, J.N., Coleman, R.L., and Sood, A.K. (2012). Resistance and escape from antiangiogenesis therapy: clinical implications and future strategies. J Clin Oncol *30*, 4026-4034.

Bray, S.J. (2016). Notch signalling in context. Nat Rev Mol Cell Biol *17*, 722-735.

Bridgeman, V.L., Vermeulen, P.B., Foo, S., Bilecz, A., Daley, F., Kostaras, E., Nathan, M.R., Wan, E., Frentzas, S., Schweiger, T.*, et al.* (2017). Vessel co-option is common in human lung metastases and mediates resistance to anti-angiogenic therapy in preclinical lung metastasis models. J Pathol *241*, 362-374.

Brooks, R.F. (1976). Regulation of fibroblast cell cycle by serum. Nature *260*, 248-250.

Brown, D.M., and Ruoslahti, E. (2004). Metadherin, a cell surface protein in breast tumors that mediates lung metastasis. Cancer Cell *5*, 365-374.

Campisi, J., Morreo, G., and Pardee, A.B. (1984). Kinetics of G1 transit following brief starvation for serum factors. Exp Cell Res *152*, 459-466.

Carmeliet, P. (2000). Mechanisms of angiogenesis and arteriogenesis. Nat Med *6*, 389-395.

Carmeliet, P., and Jain, R.K. (2011). Principles and mechanisms of vessel normalization for cancer and other angiogenic diseases. Nat Rev Drug Discov *10*, 417-427.

Carson-Walter, E.B., Watkins, D.N., Nanda, A., Vogelstein, B., Kinzler, K.W., and St Croix, B. (2001). Cell surface tumor endothelial markers are conserved in mice and humans. Cancer Res *61*, 6649-6655.

Casanovas, O., Hicklin, D.J., Bergers, G., and Hanahan, D. (2005). Drug resistance by evasion of antiangiogenic targeting of VEGF signaling in late-stage pancreatic islet tumors. Cancer Cell *8*, 299-309.

Chambers, A.F., Groom, A.C., and MacDonald, I.C. (2002). Dissemination and growth of cancer cells in metastatic sites. Nat Rev Cancer *2*, 563-572.

Chan, Y.C., Khanna, S., Roy, S., and Sen, C.K. (2011). miR-200b targets Ets-1 and is down-regulated by hypoxia to induce angiogenic response of endothelial cells. J Biol Chem *286*, 2047-2056.

Chan, Y.C., Roy, S., Khanna, S., and Sen, C.K. (2012). Downregulation of endothelial microRNA-200b supports cutaneous wound angiogenesis by desilencing GATA binding protein 2 and vascular endothelial growth factor receptor 2. Arterioscler Thromb Vasc Biol *32*, 1372-1382.

Chang, Y.S., di Tomaso, E., McDonald, D.M., Jones, R., Jain, R.K., and Munn, L.L. (2000). Mosaic blood vessels in tumors: frequency of cancer cells in contact with flowing blood. Proc Natl Acad Sci U S A *97*, 14608-14613.

Chen, A.J., Paik, J.H., Zhang, H., Shukla, S.A., Mortensen, R., Hu, J., Ying, H., Hu, B., Hurt, J., Farny, N.*, et al.* (2012). STAR RNA-binding protein Quaking suppresses cancer via stabilization of specific miRNA. Genes Dev *26*, 1459-1472.

Chen, T., and Richard, S. (1998). Structure-function analysis of Qk1: a lethal point mutation in mouse quaking prevents homodimerization. Mol Cell Biol *18*, 4863-4871.

Cochrane, A., Kelaini, S., Tsifaki, M., Bojdo, J., Vila-Gonzalez, M., Drehmer, D., Caines, R., Magee, C., Eleftheriadou, M., Hu, Y.*, et al.* (2017). Quaking Is a Key Regulator of Endothelial Cell Differentiation, Neovascularization, and Angiogenesis. Stem Cells *35*, 952-966.

Collet, G., Skrzypek, K., Grillon, C., Matejuk, A., El Hafni-Rahbi, B., Lamerant-Fayel, N., and Kieda, C. (2012). Hypoxia control to normalize pathologic angiogenesis: potential role for endothelial precursor cells and miRNAs regulation. Vascul Pharmacol *56*, 252-261.

Colorado, P.C., Torre, A., Kamphaus, G., Maeshima, Y., Hopfer, H., Takahashi, K., Volk, R., Zamborsky, E.D., Herman, S., Sarkar, P.K.*, et al.* (2000). Anti-angiogenic cues from vascular basement membrane collagen. Cancer Res *60*, 2520-2526.

Conn, S.J., Pillman, K.A., Toubia, J., Conn, V.M., Salmanidis, M., Phillips, C.A., Roslan, S., Schreiber, A.W., Gregory, P.A., and Goodall, G.J. (2015). The RNA binding protein quaking regulates formation of circRNAs. Cell *160*, 1125-1134.

Coultas, L., Chawengsaksophak, K., and Rossant, J. (2005). Endothelial cells and VEGF in vascular development. Nature *438*, 937-945.

Dahlman, J.E., Barnes, C., Khan, O., Thiriot, A., Jhunjunwala, S., Shaw, T.E., Xing, Y., Sager, H.B., Sahay, G., Speciner, L.*, et al.* (2014). In vivo endothelial siRNA delivery using polymeric nanoparticles with low molecular weight. Nat Nanotechnol *9*, 648-655.

Darland, D.C., Massingham, L.J., Smith, S.R., Piek, E., Saint-Geniez, M., and D'Amore, P.A. (2003). Pericyte production of cell-associated VEGF is differentiation-dependent and is associated with endothelial survival. Dev Biol *264*, 275-288.

de Bruin, R.G., Shiue, L., Prins, J., de Boer, H.C., Singh, A., Fagg, W.S., van Gils, J.M., Duijs, J.M., Katzman, S., Kraaijeveld, A.O.*, et al.* (2016a). Quaking promotes monocyte differentiation into pro-atherogenic macrophages by controlling pre-mRNA splicing and gene expression. Nat Commun *7*, 10846.

de Bruin, R.G., van der Veer, E.P., Prins, J., Lee, D.H., Dane, M.J., Zhang, H., Roeten, M.K., Bijkerk, R., de Boer, H.C., Rabelink, T.J.*, et al.* (2016b). The RNA-binding protein quaking maintains endothelial barrier function and affects VE-cadherin and beta-catenin protein expression. Sci Rep *6*, 21643.

Dejana, E., Tournier-Lasserve, E., and Weinstein, B.M. (2009). The control of vascular integrity by endothelial cell junctions: molecular basis and pathological implications. Dev Cell *16*, 209-221.

DeNardo, D.G., Barreto, J.B., Andreu, P., Vasquez, L., Tawfik, D., Kolhatkar, N., and Coussens, L.M. (2009). CD4(+) T cells regulate pulmonary metastasis of mammary carcinomas by enhancing protumor properties of macrophages. Cancer Cell *16*, 91-102.

Denli, A.M., Tops, B.B., Plasterk, R.H., Ketting, R.F., and Hannon, G.J. (2004). Processing of primary microRNAs by the Microprocessor complex. Nature *432*, 231-235.

Ding, Y., Hu, Z., Luan, J., Lv, X., Yuan, D., Xie, P., Yuan, S., and Liu, Q. (2017). Protective effect of miR-200b/c by inhibiting vasohibin-2 in human retinal microvascular endothelial cells. Life Sci *191*, 245-252.

Djuranovic, S., Nahvi, A., and Green, R. (2012). miRNA-mediated gene silencing by translational repression followed by mRNA deadenylation and decay. Science *336*, 237-240.

Douma, S., Van Laar, T., Zevenhoven, J., Meuwissen, R., Van Garderen, E., and Peeper, D.S. (2004). Suppression of anoikis and induction of metastasis by the neurotrophic receptor TrkB. Nature *430*, 1034-1039.

Ebersole, T.A., Chen, Q., Justice, M.J., and Artzt, K. (1996). The quaking gene product necessary in embryogenesis and myelination combines features of RNA binding and signal transduction proteins. Nat Genet *12*, 260-265.

Ebos, J.M., and Kerbel, R.S. (2011). Antiangiogenic therapy: impact on invasion, disease progression, and metastasis. Nat Rev Clin Oncol *8*, 210-221.

Ebos, J.M., Lee, C.R., Cruz-Munoz, W., Bjarnason, G.A., Christensen, J.G., and Kerbel, R.S. (2009). Accelerated metastasis after short-term treatment with a potent inhibitor of tumor angiogenesis. Cancer Cell *15*, 232-239.

Egeblad, M., and Werb, Z. (2002). New functions for the matrix metalloproteinases in cancer progression. Nat Rev Cancer *2*, 161-174.

Fagg, W.S., Liu, N., Fair, J.H., Shiue, L., Katzman, S., Donohue, J.P., and Ares, M., Jr. (2017). Autogenous cross-regulation of Quaking mRNA processing and translation balances Quaking functions in splicing and translation. Genes Dev *31*, 1894-1909.

Ferrara, N. (2002). VEGF and the quest for tumour angiogenesis factors. Nat Rev Cancer *2*, 795-803.

Ferrara, N., Gerber, H.P., and LeCouter, J. (2003). The biology of VEGF and its receptors. Nat Med *9*, 669-676.

Folkman, J. (1971). Tumor angiogenesis: therapeutic implications. N Engl J Med *285*, 1182-1186.

Folkman, J., and D'Amore, P.A. (1996). Blood vessel formation: what is its molecular basis? Cell *87*, 1153-1155.

Form, D.M., Pratt, B.M., and Madri, J.A. (1986). Endothelial cell proliferation during angiogenesis. In vitro modulation by basement membrane components. Lab Invest *55*, 521-530.

Fry, D.W., Harvey, P.J., Keller, P.R., Elliott, W.L., Meade, M., Trachet, E., Albassam, M., Zheng, X., Leopold, W.R., Pryer, N.K*., et al.* (2004). Specific inhibition of cyclin-dependent kinase 4/6 by PD 0332991 and associated antitumor activity in human tumor xenografts. Mol Cancer Ther *3*, 1427-1438.

Galarneau, A., and Richard, S. (2005). Target RNA motif and target mRNAs of the Quaking STAR protein. Nat Struct Mol Biol *12*, 691-698.

Giaccia, A.J., Simon, M.C., and Johnson, R. (2004). The biology of hypoxia: the role of oxygen sensing in development, normal function, and disease. Genes Dev *18*, 2183-2194.

Gibbons, D.L., Lin, W., Creighton, C.J., Rizvi, Z.H., Gregory, P.A., Goodall, G.J., Thilaganathan, N., Du, L., Zhang, Y., Pertsemlidis, A*., et al.* (2009). Contextual extracellular cues promote tumor cell EMT and metastasis by regulating miR-200 family expression. Genes Dev *23*, 2140-2151.

Gill, J.G., Langer, E.M., Lindsley, R.C., Cai, M., Murphy, T.L., and Murphy, K.M. (2012). Snail promotes the cell-autonomous generation of Flk1(+) endothelial cells through the repression of the microRNA-200 family. Stem Cells Dev *21*, 167-176.

Goel, S., Gupta, N., Walcott, B.P., Snuderl, M., Kesler, C.T., Kirkpatrick, N.D., Heishi, T., Huang, Y., Martin, J.D., Ager, E.*, et al.* (2013). Effects of vascular-endothelial protein tyrosine phosphatase inhibition on breast cancer vasculature and metastatic progression. J Natl Cancer Inst *105*, 1188-1201.

Greenberg, J.I., Shields, D.J., Barillas, S.G., Acevedo, L.M., Murphy, E., Huang, J., Scheppke, L., Stockmann, C., Johnson, R.S., Angle, N.*, et al.* (2008). A role for VEGF as a negative regulator of pericyte function and vessel maturation. Nature *456*, 809-813.

Gregory, P.A., Bert, A.G., Paterson, E.L., Barry, S.C., Tsykin, A., Farshid, G., Vadas, M.A., Khew-Goodall, Y., and Goodall, G.J. (2008). The miR-200 family and miR-205 regulate epithelial to mesenchymal transition by targeting ZEB1 and SIP1. Nat Cell Biol *10*, 593-601.

Gregory, R.I., Yan, K.P., Amuthan, G., Chendrimada, T., Doratotaj, B., Cooch, N., and Shiekhattar, R. (2004). The Microprocessor complex mediates the genesis of microRNAs. Nature *432*, 235-240.

Griffin, M.J. (1976). Synchronization of some human cell strains by serum and calcium starvation. In Vitro *12*, 393-398.

Grishok, A., Pasquinelli, A.E., Conte, D., Li, N., Parrish, S., Ha, I., Baillie, D.L., Fire, A., Ruvkun, G., and Mello, C.C. (2001). Genes and mechanisms related to RNA interference regulate expression of the small temporal RNAs that control C. elegans developmental timing. Cell *106*, 23-34.

Grivennikov, S.I., Greten, F.R., and Karin, M. (2010). Immunity, inflammation, and cancer. Cell *140*, 883-899.

Guo, M., Breslin, J.W., Wu, M.H., Gottardi, C.J., and Yuan, S.Y. (2008). VE-cadherin and beta-catenin binding dynamics during histamine-induced endothelial hyperpermeability. Am J Physiol Cell Physiol *294*, C977-984.

Guo, W., and Giancotti, F.G. (2004). Integrin signalling during tumour progression. Nat Rev Mol Cell Biol *5*, 816-826.

Gupta, G.P., and Massague, J. (2006). Cancer metastasis: building a framework. Cell *127*, 679-695.

Gupta, G.P., Nguyen, D.X., Chiang, A.C., Bos, P.D., Kim, J.Y., Nadal, C., Gomis, R.R., Manova-Todorova, K., and Massague, J. (2007a). Mediators of vascular remodelling co-opted for sequential steps in lung metastasis. Nature *446*, 765-770.

Gupta, G.P., Perk, J., Acharyya, S., de Candia, P., Mittal, V., Todorova-Manova, K., Gerald, W.L., Brogi, E., Benezra, R., and Massague, J. (2007b). ID genes mediate tumor reinitiation during breast cancer lung metastasis. Proc Natl Acad Sci U S A *104*, 19506-19511.

Ha, M., and Kim, V.N. (2014). Regulation of microRNA biogenesis. Nat Rev Mol Cell Biol *15*, 509-524.

Hall, M.P., Nagel, R.J., Fagg, W.S., Shiue, L., Cline, M.S., Perriman, R.J., Donohue, J.P., and Ares, M., Jr. (2013). Quaking and PTB control overlapping splicing regulatory networks during muscle cell differentiation. Rna *19*, 627-638.

Han, H.D., Mangala, L.S., Lee, J.W., Shahzad, M.M., Kim, H.S., Shen, D., Nam, E.J., Mora, E.M., Stone, R.L., Lu, C.*, et al.* (2010). Targeted gene silencing using RGD-labeled chitosan nanoparticles. Clin Cancer Res *16*, 3910-3922.

Han, J., Lee, Y., Yeom, K.H., Kim, Y.K., Jin, H., and Kim, V.N. (2004a). The Drosha-DGCR8 complex in primary microRNA processing. Genes Dev *18*, 3016-3027.

Han, M.H., Goud, S., Song, L., and Fedoroff, N. (2004b). The Arabidopsis double-stranded RNA-binding protein HYL1 plays a role in microRNA-mediated gene regulation. Proc Natl Acad Sci U S A *101*, 1093-1098.

Hanahan, D., and Folkman, J. (1996). Patterns and emerging mechanisms of the angiogenic switch during tumorigenesis. Cell *86*, 353-364.

Hansen, T.B., Jensen, T.I., Clausen, B.H., Bramsen, J.B., Finsen, B., Damgaard, C.K., and Kjems, J. (2013). Natural RNA circles function as efficient microRNA sponges. Nature *495*, 384-388.

Hardy, R.J. (1998). Molecular defects in the dysmyelinating mutant quaking. J Neurosci Res *51*, 417-422.

Hardy, R.J., Loushin, C.L., Friedrich, V.L., Jr., Chen, Q., Ebersole, T.A., Lazzarini, R.A., and Artzt, K. (1996). Neural cell type-specific expression of QKI proteins is altered in quakingviable mutant mice. J Neurosci *16*, 7941-7949.

Harrison, E.B., Azam, S.H., and Pecot, C.V. (2018). Targeting Accessories to the Crime: Nanoparticle Nucleic Acid Delivery to the Tumor Microenvironment. Front Pharmacol *9*, 307.

Hirschi, K.K., and D'Amore, P.A. (1997). Control of angiogenesis by the pericyte: molecular mechanisms and significance. EXS *79*, 419-428.

Hlatky, L., Hahnfeldt, P., and Folkman, J. (2002). Clinical application of antiangiogenic therapy: microvessel density, what it does and doesn't tell us. J Natl Cancer Inst *94*, 883-893.

Hood, J.D., Bednarski, M., Frausto, R., Guccione, S., Reisfeld, R.A., Xiang, R., and Cheresh, D.A. (2002). Tumor regression by targeted gene delivery to the neovasculature. Science *296*, 2404-2407.

Humphries, B., and Yang, C. (2015). The microRNA-200 family: small molecules with novel roles in cancer development, progression and therapy. Oncotarget *6*, 6472-6498.

Jain, R.K. (2005). Normalization of tumor vasculature: an emerging concept in antiangiogenic therapy. Science *307*, 58-62.

Jain, R.K. (2014). Antiangiogenesis strategies revisited: from starving tumors to alleviating hypoxia. Cancer Cell *26*, 605-622.

Jain, R.K., Martin, J.D., and Stylianopoulos, T. (2014). The role of mechanical forces in tumor growth and therapy. Annu Rev Biomed Eng *16*, 321-346.

Jakobsson, L., Franco, C.A., Bentley, K., Collins, R.T., Ponsioen, B., Aspalter, I.M., Rosewell, I., Busse, M., Thurston, G., Medvinsky, A.*, et al.* (2010). Endothelial cells dynamically compete for the tip cell position during angiogenic sprouting. Nat Cell Biol *12*, 943-953.

Jayson, G.C., Kerbel, R., Ellis, L.M., and Harris, A.L. (2016). Antiangiogenic therapy in oncology: current status and future directions. Lancet *388*, 518-529.

Jeck, W.R., and Sharpless, N.E. (2014). Detecting and characterizing circular RNAs. Nature biotechnology *32*, 453-461.

Jeck, W.R., Sorrentino, J.A., Wang, K., Slevin, M.K., Burd, C.E., Liu, J., Marzluff, W.F., and Sharpless, N.E. (2013). Circular RNAs are abundant, conserved, and associated with ALU repeats. Rna *19*, 141-157.

Ji, H., Ramsey, M.R., Hayes, D.N., Fan, C., McNamara, K., Kozlowski, P., Torrice, C., Wu, M.C., Shimamura, T., Perera, S.A.*, et al.* (2007). LKB1 modulates lung cancer differentiation and metastasis. Nature *448*, 807-810.

Jonas, S., and Izaurralde, E. (2015). Towards a molecular understanding of microRNA-mediated gene silencing. Nat Rev Genet *16*, 421-433.

Joyce, J.A., and Pollard, J.W. (2009). Microenvironmental regulation of metastasis. Nat Rev Cancer *9*, 239-252.

Kalluri, R. (2003). Basement membranes: structure, assembly and role in tumour angiogenesis. Nat Rev Cancer *3*, 422-433.

Kamphaus, G.D., Colorado, P.C., Panka, D.J., Hopfer, H., Ramchandran, R., Torre, A., Maeshima, Y., Mier, J.W., Sukhatme, V.P., and Kalluri, R. (2000). Canstatin, a novel matrix-derived inhibitor of angiogenesis and tumor growth. J Biol Chem *275*, 1209-1215.

Kang, Y., Siegel, P.M., Shu, W., Drobnjak, M., Kakonen, S.M., Cordon-Cardo, C., Guise, T.A., and Massague, J. (2003). A multigenic program mediating breast cancer metastasis to bone. Cancer Cell *3*, 537-549.

Kessenbrock, K., Plaks, V., and Werb, Z. (2010). Matrix metalloproteinases: regulators of the tumor microenvironment. Cell *141*, 52-67.

Ketting, R.F., Fischer, S.E., Bernstein, E., Sijen, T., Hannon, G.J., and Plasterk, R.H. (2001). Dicer functions in RNA interference and in synthesis of small RNA involved in developmental timing in C. elegans. Genes Dev *15*, 2654-2659.

Khan, O.F., Zaia, E.W., Jhunjhunwala, S., Xue, W., Cai, W., Yun, D.S., Barnes, C.M., Dahlman, J.E., Dong, Y., Pelet, J.M.*, et al.* (2015). Dendrimer-Inspired Nanomaterials for the in Vivo Delivery of siRNA to Lung Vasculature. Nano Lett *15*, 3008-3016.

Kim, Y.M., Jang, J.W., Lee, O.H., Yeon, J., Choi, E.Y., Kim, K.W., Lee, S.T., and Kwon, Y.G. (2000). Endostatin inhibits endothelial and tumor cellular invasion by blocking the activation and catalytic activity of matrix metalloproteinase. Cancer Res *60*, 5410-5413.

Kobayashi, H., and Tomari, Y. (2016). RISC assembly: Coordination between small RNAs and Argonaute proteins. Biochim Biophys Acta *1859*, 71-81.

Koch, A.W., Mathivet, T., Larrivee, B., Tong, R.K., Kowalski, J., Pibouin-Fragner, L., Bouvree, K., Stawicki, S., Nicholes, K., Rathore, N.*, et al.* (2011). Robo4 maintains vessel integrity and inhibits angiogenesis by interacting with UNC5B. Dev Cell *20*, 33-46.

Kondo, T., Furuta, T., Mitsunaga, K., Ebersole, T.A., Shichiri, M., Wu, J., Artzt, K., Yamamura, K., and Abe, K. (1999). Genomic organization and expression analysis of the mouse qkI locus. Mamm Genome *10*, 662-669.

Korpal, M., Ell, B.J., Buffa, F.M., Ibrahim, T., Blanco, M.A., Celia-Terrassa, T., Mercatali, L., Khan, Z., Goodarzi, H., Hua, Y.*, et al.* (2011). Direct targeting of Sec23a by miR-200s influences cancer cell secretome and promotes metastatic colonization. Nat Med *17*, 1101-1108.

Kuczynski, E.A., Vermeulen, P.B., Pezzella, F., Kerbel, R.S., and Reynolds, A.R. (2019). Vessel co-option in cancer. Nat Rev Clin Oncol.

Kuczynski, E.A., Yin, M., Bar-Zion, A., Lee, C.R., Butz, H., Man, S., Daley, F., Vermeulen, P.B., Yousef, G.M., Foster, F.S.*, et al.* (2016). Co-option of Liver Vessels and Not Sprouting Angiogenesis Drives Acquired Sorafenib Resistance in Hepatocellular Carcinoma. J Natl Cancer Inst *108*.

La Porta, S., Roth, L., Singhal, M., Mogler, C., Spegg, C., Schieb, B., Qu, X., Adams, R.H., Baldwin, H.S., Savant, S.*, et al.* (2018). Endothelial Tie1-mediated angiogenesis and vascular abnormalization promote tumor progression and metastasis. J Clin Invest *128*, 834-845.

Lamouille, S., Xu, J., and Derynck, R. (2014). Molecular mechanisms of epithelial-mesenchymal transition. Nat Rev Mol Cell Biol *15*, 178-196.

Lamprecht, M.R., Sabatini, D.M., and Carpenter, A.E. (2007). CellProfiler: free, versatile software for automated biological image analysis. Biotechniques *42*, 71-75.

Landen, C.N., Jr., Chavez-Reyes, A., Bucana, C., Schmandt, R., Deavers, M.T., Lopez-Berestein, G., and Sood, A.K. (2005). Therapeutic EphA2 gene targeting in vivo using neutral liposomal small interfering RNA delivery. Cancer Res *65*, 6910-6918.

Larocque, D., Galarneau, A., Liu, H.N., Scott, M., Almazan, G., and Richard, S. (2005). Protection of p27(Kip1) mRNA by quaking RNA binding proteins promotes oligodendrocyte differentiation. Nat Neurosci *8*, 27-33.

Larocque, D., Pilotte, J., Chen, T., Cloutier, F., Massie, B., Pedraza, L., Couture, R., Lasko, P., Almazan, G., and Richard, S. (2002). Nuclear retention of MBP mRNAs in the quaking viable mice. Neuron *36*, 815-829.

Larrivee, B., Freitas, C., Suchting, S., Brunet, I., and Eichmann, A. (2009). Guidance of vascular development: lessons from the nervous system. Circ Res *104*, 428-441.

Larrivee, B., Freitas, C., Trombe, M., Lv, X., Delafarge, B., Yuan, L., Bouvree, K., Breant, C., Del Toro, R., Brechot, N.*, et al.* (2007). Activation of the UNC5B receptor by Netrin-1 inhibits sprouting angiogenesis. Genes Dev *21*, 2433-2447.

Lawler, P.R., and Lawler, J. (2012). Molecular basis for the regulation of angiogenesis by thrombospondin-1 and -2. Cold Spring Harb Perspect Med *2*, a006627.

Lee, Y., Ahn, C., Han, J., Choi, H., Kim, J., Yim, J., Lee, J., Provost, P., Radmark, O., Kim, S.*, et al.* (2003). The nuclear RNase III Drosha initiates microRNA processing. Nature *425*, 415-419.

Li, Z., Takakura, N., Oike, Y., Imanaka, T., Araki, K., Suda, T., Kaname, T., Kondo, T., Abe, K., and Yamamura, K. (2003). Defective smooth muscle development in qkI-deficient mice. Dev Growth Differ *45*, 449-462.

Li, Z., Zhang, Y., Li, D., and Feng, Y. (2000). Destabilization and mislocalization of myelin basic protein mRNAs in quaking dysmyelination lacking the QKI RNA-binding proteins. J Neurosci *20*, 4944-4953.

Lobbardi, R., Lambert, G., Zhao, J., Geisler, R., Kim, H.R., and Rosa, F.M. (2011). Fine-tuning of Hh signaling by the RNA-binding protein Quaking to control muscle development. Development *138*, 1783-1794.

Lu, C., Han, H.D., Mangala, L.S., Ali-Fehmi, R., Newton, C.S., Ozbun, L., Armaiz-Pena, G.N., Hu, W., Stone, R.L., Munkarah, A.*, et al.* (2010). Regulation of tumor angiogenesis by EZH2. Cancer Cell *18*, 185-197.

Lucke, S., and Levkau, B. (2010). Endothelial functions of sphingosine-1-phosphate. Cell Physiol Biochem *26*, 87-96.

Lund, E., Guttinger, S., Calado, A., Dahlberg, J.E., and Kutay, U. (2004). Nuclear export of microRNA precursors. Science *303*, 95-98.

Maeshima, Y., Manfredi, M., Reimer, C., Holthaus, K.A., Hopfer, H., Chandamuri, B.R., Kharbanda, S., and Kalluri, R. (2001). Identification of the anti-angiogenic site within vascular basement membrane-derived tumstatin. J Biol Chem *276*, 15240-15248.

Magenta, A., Cencioni, C., Fasanaro, P., Zaccagnini, G., Greco, S., Sarra-Ferraris, G., Antonini, A., Martelli, F., and Capogrossi, M.C. (2011). miR-200c is upregulated by oxidative stress and induces endothelial cell apoptosis and senescence via ZEB1 inhibition. Cell Death Differ *18*, 1628-1639.

Maniotis, A.J., Folberg, R., Hess, A., Seftor, E.A., Gardner, L.M., Pe'er, J., Trent, J.M., Meltzer, P.S., and Hendrix, M.J. (1999). Vascular channel formation by human melanoma cells in vivo and in vitro: vasculogenic mimicry. Am J Pathol *155*, 739-752.

Mattila, P.K., and Lappalainen, P. (2008). Filopodia: molecular architecture and cellular functions. Nat Rev Mol Cell Biol *9*, 446-454.

Mazzieri, R., Pucci, F., Moi, D., Zonari, E., Ranghetti, A., Berti, A., Politi, L.S., Gentner, B., Brown, J.L., Naldini, L.*, et al.* (2011). Targeting the ANG2/TIE2 axis inhibits tumor growth and metastasis by impairing angiogenesis and disabling rebounds of proangiogenic myeloid cells. Cancer Cell *19*, 512-526.

Mazzone, M., Dettori, D., de Oliveira, R.L., Loges, S., Schmidt, T., Jonckx, B., Tian, Y.M., Lanahan, A.A., Pollard, P., de Almodovar, C.R.*, et al.* (2009). Heterozygous deficiency of PHD2 restores tumor oxygenation and inhibits metastasis via endothelial normalization. Cell *136*, 839-851.

Memczak, S., Jens, M., Elefsinioti, A., Torti, F., Krueger, J., Rybak, A., Maier, L., Mackowiak, S.D., Gregersen, L.H., Munschauer, M.*, et al.* (2013). Circular RNAs are a large class of animal RNAs with regulatory potency. Nature *495*, 333-338.

Morikawa, S., Baluk, P., Kaidoh, T., Haskell, A., Jain, R.K., and McDonald, D.M. (2002). Abnormalities in pericytes on blood vessels and endothelial sprouts in tumors. Am J Pathol *160*, 985-1000.

Murphy, E.A., Majeti, B.K., Barnes, L.A., Makale, M., Weis, S.M., Lutu-Fuga, K., Wrasidlo, W., and Cheresh, D.A. (2008). Nanoparticle-mediated drug delivery to tumor vasculature suppresses metastasis. Proc Natl Acad Sci U S A *105*, 9343-9348.

Nakatsu, M.N., Davis, J., and Hughes, C.C. (2007). Optimized fibrin gel bead assay for the study of angiogenesis. J Vis Exp, 186.

Nakatsu, M.N., and Hughes, C.C. (2008). An optimized three-dimensional in vitro model for the analysis of angiogenesis. Methods Enzymol *443*, 65-82.

Nehls, V., and Drenckhahn, D. (1995). A novel, microcarrier-based in vitro assay for rapid and reliable quantification of three-dimensional cell migration and angiogenesis. Microvasc Res *50*, 311-322.

Newman, A.C., Nakatsu, M.N., Chou, W., Gershon, P.D., and Hughes, C.C. (2011). The requirement for fibroblasts in angiogenesis: fibroblast-derived matrix proteins are essential for endothelial cell lumen formation. Mol Biol Cell *22*, 3791-3800.

Noguera-Troise, I., Daly, C., Papadopoulos, N.J., Coetzee, S., Boland, P., Gale, N.W., Lin, H.C., Yancopoulos, G.D., and Thurston, G. (2006). Blockade of Dll4 inhibits tumour growth by promoting non-productive angiogenesis. Nature *444*, 1032-1037.

Noveroske, J.K., Lai, L., Gaussin, V., Northrop, J.L., Nakamura, H., Hirschi, K.K., and Justice, M.J. (2002). Quaking is essential for blood vessel development. Genesis *32*, 218-230.

Padua, D., Zhang, X.H., Wang, Q., Nadal, C., Gerald, W.L., Gomis, R.R., and Massague, J. (2008). TGFbeta primes breast tumors for lung metastasis seeding through angiopoietin-like 4. Cell *133*, 66-77.

Paez-Ribes, M., Allen, E., Hudock, J., Takeda, T., Okuyama, H., Vinals, F., Inoue, M., Bergers, G., Hanahan, D., and Casanovas, O. (2009). Antiangiogenic therapy elicits malignant progression of tumors to increased local invasion and distant metastasis. Cancer Cell *15*, 220-231.

Paget, S. (1889). The distribution of secondary growths in cancer of the breast. 1889. Cancer Metastasis Rev *8*, 98-101.

Park, S.M., Gaur, A.B., Lengyel, E., and Peter, M.E. (2008). The miR-200 family determines the epithelial phenotype of cancer cells by targeting the E-cadherin repressors ZEB1 and ZEB2. Genes Dev *22*, 894-907.

Paulis, Y.W., Soetekouw, P.M., Verheul, H.M., Tjan-Heijnen, V.C., and Griffioen, A.W. (2010). Signalling pathways in vasculogenic mimicry. Biochim Biophys Acta *1806*, 18-28.

Pecot, C.V., Calin, G.A., Coleman, R.L., Lopez-Berestein, G., and Sood, A.K. (2011). RNA interference in the clinic: challenges and future directions. Nat Rev Cancer *11*, 59-67.

Pecot, C.V., Rupaimoole, R., Yang, D., Akbani, R., Ivan, C., Lu, C., Wu, S., Han, H.D., Shah, M.Y., Rodriguez-Aguayo, C.*, et al.* (2013). Tumour angiogenesis regulation by the miR-200 family. Nat Commun *4*, 2427.

Pettersson, A., Nagy, J.A., Brown, L.F., Sundberg, C., Morgan, E., Jungles, S., Carter, R., Krieger, J.E., Manseau, E.J., Harvey, V.S.*, et al.* (2000). Heterogeneity of the angiogenic response induced in different normal adult tissues by vascular permeability factor/vascular endothelial growth factor. Lab Invest *80*, 99-115.

Pfaff, J., Hennig, J., Herzog, F., Aebersold, R., Sattler, M., Niessing, D., and Meister, G. (2013). Structural features of Argonaute-GW182 protein interactions. Proc Natl Acad Sci U S A *110*, E3770-3779.

Phng, L.K., and Gerhardt, H. (2009). Angiogenesis: a team effort coordinated by notch. Dev Cell *16*, 196-208.

Pichler, M., and Calin, G.A. (2015). MicroRNAs in cancer: from developmental genes in worms to their clinical application in patients. Br J Cancer *113*, 569-573.

Pillman, K.A., Phillips, C.A., Roslan, S., Toubia, J., Dredge, B.K., Bert, A.G., Lumb, R., Neumann, D.P., Li, X., Conn, S.J.*, et al.* (2018). miR-200/375 control epithelial plasticity-associated alternative splicing by repressing the RNA-binding protein Quaking. EMBO J.

Pilotte, J., Larocque, D., and Richard, S. (2001). Nuclear translocation controlled by alternatively spliced isoforms inactivates the QUAKING apoptotic inducer. Genes Dev *15*, 845-858.

Popson, S.A., Ziegler, M.E., Chen, X., Holderfield, M.T., Shaaban, C.I., Fong, A.H., Welch-Reardon, K.M., Papkoff, J., and Hughes, C.C. (2014). Interferon-induced transmembrane protein 1 regulates endothelial lumen formation during angiogenesis. Arterioscler Thromb Vasc Biol *34*, 1011-1019.

Prabhakar, U., Maeda, H., Jain, R.K., Sevick-Muraca, E.M., Zamboni, W., Farokhzad, O.C., Barry, S.T., Gabizon, A., Grodzinski, P., and Blakey, D.C. (2013). Challenges and key considerations of the enhanced permeability and retention effect for nanomedicine drug delivery in oncology. Cancer Res *73*, 2412-2417.

Psaila, B., and Lyden, D. (2009). The metastatic niche: adapting the foreign soil. Nat Rev Cancer *9*, 285-293.

Reymond, N., d'Agua, B.B., and Ridley, A.J. (2013). Crossing the endothelial barrier during metastasis. Nat Rev Cancer *13*, 858-870.

Ridley, A.J. (2015). Rho GTPase signalling in cell migration. Curr Opin Cell Biol *36*, 103-112.

Rodriguez-Manzaneque, J.C., Lane, T.F., Ortega, M.A., Hynes, R.O., Lawler, J., and Iruela-Arispe, M.L. (2001). Thrombospondin-1 suppresses spontaneous tumor growth and inhibits activation of matrix metalloproteinase-9 and mobilization of vascular endothelial growth factor. Proc Natl Acad Sci U S A *98*, 12485-12490.

Ruf, W., Seftor, E.A., Petrovan, R.J., Weiss, R.M., Gruman, L.M., Margaryan, N.V., Seftor, R.E., Miyagi, Y., and Hendrix, M.J. (2003). Differential role of tissue factor pathway inhibitors 1 and 2 in melanoma vasculogenic mimicry. Cancer Res *63*, 5381-5389.

Ruoslahti, E. (2004). Vascular zip codes in angiogenesis and metastasis. Biochem Soc Trans *32*, 397-402.

Rupaimoole, R., Wu, S.Y., Pradeep, S., Ivan, C., Pecot, C.V., Gharpure, K.M., Nagaraja, A.S., Armaiz-Pena, G.N., McGuire, M., Zand, B.*, et al.* (2014). Hypoxia-mediated downregulation of miRNA biogenesis promotes tumour progression. Nat Commun *5*, 5202.

Saccomanno, L., Loushin, C., Jan, E., Punkay, E., Artzt, K., and Goodwin, E.B. (1999). The STAR protein QKI-6 is a translational repressor. Proc Natl Acad Sci U S A *96*, 12605-12610.

Sacharidou, A., Stratman, A.N., and Davis, G.E. (2012). Molecular mechanisms controlling vascular lumen formation in three-dimensional extracellular matrices. Cells Tissues Organs *195*, 122-143.

Santel, A., Aleku, M., Keil, O., Endruschat, J., Esche, V., Durieux, B., Loffler, K., Fechtner, M., Rohl, T., Fisch, G.*, et al.* (2006). RNA interference in the mouse vascular endothelium by systemic administration of siRNA-lipoplexes for cancer therapy. Gene Ther *13*, 1360-1370.

Santo, L., Siu, K.T., and Raje, N. (2015). Targeting Cyclin-Dependent Kinases and Cell Cycle Progression in Human Cancers. Semin Oncol *42*, 788-800.

Schirle, N.T., and MacRae, I.J. (2012). The crystal structure of human Argonaute2. Science *336*, 1037-1040.

Seaman, S., Zhu, Z., Saha, S., Zhang, X.M., Yang, M.Y., Hilton, M.B., Morris, K., Szot, C., Morris, H., Swing, D.A.*, et al.* (2017). Eradication of Tumors through Simultaneous Ablation of CD276/B7-H3-Positive Tumor Cells and Tumor Vasculature. Cancer Cell *31*, 501-515 e508.

Semenza, G.L. (2003). Angiogenesis in ischemic and neoplastic disorders. Annu Rev Med *54*, 17-28.

Sethi, N., Dai, X., Winter, C.G., and Kang, Y. (2011). Tumor-derived JAGGED1 promotes osteolytic bone metastasis of breast cancer by engaging notch signaling in bone cells. Cancer Cell *19*, 192-205.

Shaked, Y., Ciarrocchi, A., Franco, M., Lee, C.R., Man, S., Cheung, A.M., Hicklin, D.J., Chaplin, D., Foster, F.S., Benezra, R.*, et al.* (2006). Therapy-induced acute recruitment of circulating endothelial progenitor cells to tumors. Science *313*, 1785-1787.

Shannon, P., Markiel, A., Ozier, O., Baliga, N.S., Wang, J.T., Ramage, D., Amin, N., Schwikowski, B., and Ideker, T. (2003). Cytoscape: a software environment for integrated models of biomolecular interaction networks. Genome Res *13*, 2498-2504.

Sidman, R.L., Dickie, M.M., and Appel, S.H. (1964). Mutant Mice (Quaking and Jimpy) with Deficient Myelination in the Central Nervous System. Science *144*, 309-311.

Sims, D.E. (1986). The pericyte--a review. Tissue Cell *18*, 153-174.

Sonoshita, M., Aoki, M., Fuwa, H., Aoki, K., Hosogi, H., Sakai, Y., Hashida, H., Takabayashi, A., Sasaki, M., Robine, S.*, et al.* (2011). Suppression of colon cancer metastasis by Aes through inhibition of Notch signaling. Cancer Cell *19*, 125-137.

St Croix, B., Rago, C., Velculescu, V., Traverso, G., Romans, K.E., Montgomery, E., Lal, A., Riggins, G.J., Lengauer, C., Vogelstein, B.*, et al.* (2000). Genes expressed in human tumor endothelium. Science *289*, 1197-1202.

Stewart, P.L., and Nemerow, G.R. (2007). Cell integrins: commonly used receptors for diverse viral pathogens. Trends Microbiol *15*, 500-507.

Strilic, B., Kucera, T., Eglinger, J., Hughes, M.R., McNagny, K.M., Tsukita, S., Dejana, E., Ferrara, N., and Lammert, E. (2009). The molecular basis of vascular lumen formation in the developing mouse aorta. Dev Cell *17*, 505-515.

Tahergorabi, Z., and Khazaei, M. (2012). A review on angiogenesis and its assays. Iran J Basic Med Sci *15*, 1110-1126.

Tattersall, I.W., Du, J., Cong, Z., Cho, B.S., Klein, A.M., Dieck, C.L., Chaudhri, R.A., Cuervo, H., Herts, J.H., and Kitajewski, J. (2016). In vitro modeling of endothelial interaction with macrophages and pericytes demonstrates Notch signaling function in the vascular microenvironment. Angiogenesis *19*, 201-215.

Teplova, M., Hafner, M., Teplov, D., Essig, K., Tuschl, T., and Patel, D.J. (2013). Structure-function studies of STAR family Quaking proteins bound to their in vivo RNA target sites. Genes Dev *27*, 928-940.

Thiery, J.P., Acloque, H., Huang, R.Y., and Nieto, M.A. (2009). Epithelial-mesenchymal transitions in development and disease. Cell *139*, 871-890.

Treiber, T., Treiber, N., and Meister, G. (2019). Regulation of microRNA biogenesis and its crosstalk with other cellular pathways. Nat Rev Mol Cell Biol *20*, 5-20.

Valastyan, S., and Weinberg, R.A. (2011). Tumor metastasis: molecular insights and evolving paradigms. Cell *147*, 275-292.

van den Beucken, T., Koch, E., Chu, K., Rupaimoole, R., Prickaerts, P., Adriaens, M., Voncken, J.W., Harris, A.L., Buffa, F.M., Haider, S.*, et al.* (2014). Hypoxia promotes stem cell phenotypes and poor prognosis through epigenetic regulation of DICER. Nat Commun *5*, 5203.

van Mil, A., Grundmann, S., Goumans, M.J., Lei, Z., Oerlemans, M.I., Jaksani, S., Doevendans, P.A., and Sluijter, J.P. (2012). MicroRNA-214 inhibits angiogenesis by targeting Quaking and reducing angiogenic growth factor release. Cardiovasc Res *93*, 655-665.

Vasudev, N.S., and Reynolds, A.R. (2014). Anti-angiogenic therapy for cancer: current progress, unresolved questions and future directions. Angiogenesis *17*, 471-494.

Vernet, C., and Artzt, K. (1997). STAR, a gene family involved in signal transduction and activation of RNA. Trends Genet *13*, 479-484.

Viallard, C., and Larrivee, B. (2017). Tumor angiogenesis and vascular normalization: alternative therapeutic targets. Angiogenesis *20*, 409-426.

Wallez, Y., and Huber, P. (2008). Endothelial adherens and tight junctions in vascular homeostasis, inflammation and angiogenesis. Biochim Biophys Acta *1778*, 794-809.

Wang, Y., Vogel, G., Yu, Z., and Richard, S. (2013). The QKI-5 and QKI-6 RNA binding proteins regulate the expression of microRNA 7 in glial cells. Mol Cell Biol *33*, 1233-1243.

Welch-Reardon, K.M., Wu, N., and Hughes, C.C. (2015). A role for partial endothelial-mesenchymal transitions in angiogenesis? Arterioscler Thromb Vasc Biol *35*, 303-308.

Welti, J., Loges, S., Dimmeler, S., and Carmeliet, P. (2013). Recent molecular discoveries in angiogenesis and antiangiogenic therapies in cancer. J Clin Invest *123*, 3190-3200.

Williamson, M.P. (1994). The structure and function of proline-rich regions in proteins. Biochem J *297 (Pt 2)*, 249-260.

Winkler, F., Kozin, S.V., Tong, R.T., Chae, S.S., Booth, M.F., Garkavtsev, I., Xu, L., Hicklin, D.J., Fukumura, D., di Tomaso, E.*, et al.* (2004). Kinetics of vascular normalization by VEGFR2 blockade governs brain tumor response to radiation: role of oxygenation, angiopoietin-1, and matrix metalloproteinases. Cancer Cell *6*, 553-563.

Winslow, M.M., Dayton, T.L., Verhaak, R.G., Kim-Kiselak, C., Snyder, E.L., Feldser, D.M., Hubbard, D.D., DuPage, M.J., Whittaker, C.A., Hoersch, S.*, et al.* (2011). Suppression of lung adenocarcinoma progression by Nkx2-1. Nature *473*, 101-104.

Winter, J., Jung, S., Keller, S., Gregory, R.I., and Diederichs, S. (2009). Many roads to maturity: microRNA biogenesis pathways and their regulation. Nature cell biology *11*, 228-234.

Wong, P.P., Bodrug, N., and Hodivala-Dilke, K.M. (2016). Exploring Novel Methods for Modulating Tumor Blood Vessels in Cancer Treatment. Curr Biol *26*, R1161-R1166.

Wong, P.P., Demircioglu, F., Ghazaly, E., Alrawashdeh, W., Stratford, M.R., Scudamore, C.L., Cereser, B., Crnogorac-Jurcevic, T., McDonald, S., Elia, G.*, et al.* (2015). Dual-action combination therapy enhances angiogenesis while reducing tumor growth and spread. Cancer Cell *27*, 123-137.

Wu, J., Zhou, L., Tonissen, K., Tee, R., and Artzt, K. (1999). The quaking I-5 protein (QKI-5) has a novel nuclear localization signal and shuttles between the nucleus and the cytoplasm. J Biol Chem *274*, 29202-29210.

Wu, J.I., Reed, R.B., Grabowski, P.J., and Artzt, K. (2002). Function of quaking in myelination: regulation of alternative splicing. Proc Natl Acad Sci U S A *99*, 4233-4238.

Wu, Y., Li, Z., Yang, M., Dai, B., Hu, F., Yang, F., Zhu, J., Chen, T., and Zhang, L. (2017). MicroRNA-214 regulates smooth muscle cell differentiation from stem cells by targeting RNA-binding protein QKI. Oncotarget *8*, 19866-19878.

Yancopoulos, G.D., Davis, S., Gale, N.W., Rudge, J.S., Wiegand, S.J., and Holash, J. (2000). Vascular-specific growth factors and blood vessel formation. Nature *407*, 242-248.

Yang, J.P., Liao, Y.D., Mai, D.M., Xie, P., Qiang, Y.Y., Zheng, L.S., Wang, M.Y., Mei, Y., Meng, D.F., Xu, L.*, et al.* (2016). Tumor vasculogenic mimicry predicts poor prognosis in cancer patients: a meta-analysis. Angiogenesis *19*, 191-200.

Yi, R., Qin, Y., Macara, I.G., and Cullen, B.R. (2003). Exportin-5 mediates the nuclear export of pre-microRNAs and short hairpin RNAs. Genes Dev *17*, 3011-3016.

Zearfoss, N.R., Clingman, C.C., Farley, B.M., McCoig, L.M., and Ryder, S.P. (2011). Quaking regulates Hnrnpa1 expression through its 3' UTR in oligodendrocyte precursor cells. PLoS Genet *7*, e1001269.

Zhang, X.H., Wang, Q., Gerald, W., Hudis, C.A., Norton, L., Smid, M., Foekens, J.A., and Massague, J. (2009). Latent bone metastasis in breast cancer tied to Src-dependent survival signals. Cancer Cell *16*, 67-78.

Zhang, Y., Lu, Z., Ku, L., Chen, Y., Wang, H., and Feng, Y. (2003). Tyrosine phosphorylation of QKI mediates developmental signals to regulate mRNA metabolism. EMBO J *22*, 1801-1810.

Zhang, Z.G., and Chopp, M. (2009). Neurorestorative therapies for stroke: underlying mechanisms and translation to the clinic. Lancet Neurol *8*, 491-500.

Zhou, X., Li, X., Sun, C., Shi, C., Hua, D., Yu, L., Wen, Y., Hua, F., Wang, Q., Zhou, Q.*, et al.* (2017). Quaking-5 suppresses aggressiveness of lung cancer cells through inhibiting beta-catenin signaling pathway. Oncotarget *8*, 82174-82184.

Zong, F.Y., Fu, X., Wei, W.J., Luo, Y.G., Heiner, M., Cao, L.J., Fang, Z., Fang, R., Lu, D., Ji, H.*, et al.* (2014). The RNA-binding protein QKI suppresses cancer-associated aberrant splicing. PLoS Genet *10*, e1004289.

Zorn, A.M., Grow, M., Patterson, K.D., Ebersole, T.A., Chen, Q., Artzt, K., and Krieg, P.A. (1997). Remarkable sequence conservation of transcripts encoding amphibian and mammalian homologues of quaking, a KH domain RNA-binding protein. Gene *188*, 199-206.